Scuola Normale Superiore

Tesi di Perfezionamento in Fisica

A measurement of the Gluon Splitting Rate into $c\bar{c}$ Pairs in Hadronic Z^0 Decays with the ALEPH detector

Candidate

Andrea Giammanco

Supervisor

Prof. Lorenzo Foà

Ph.D. Thesis

Pisa, April 2003

Contents

Preface

Cerré los ojos, los abrí. Entonces vi el Aleph.
Arribo, ahora, al inefable centro de mi relato,
empieza aquí mi desesperación de escritor.

(I shut my eyes, I opened them. Then I saw the Aleph.
I arrive now at the ineffable core of my story,
and here begins my despair as a writer.)

Jorge Luis Borges, "El Aleph"

This thesis describes the measurement of the rate of $g \to c\bar{c}$ in hadronic Z^0 decays with the ALEPH detector by tagging the leptons originating from the semileptonic decays of the c quarks.

The rate is normalized to all hadronic decays of the Z^0, as follows:

$$g_{c\bar{c}} = \frac{N(Z^0 \to q\bar{q}g, g \to c\bar{c})}{N(Z^0 \to hadrons)} \tag{1}$$

Measuring the gluon splitting rate is important as a test of perturbative QCD at the Z^0 scale. The process $g \to Q\bar{Q}$ is one of the main backgrounds in several analyses involving heavy flavoured quarks, since c and b from gluon splitting can be wrongly identified as primary quarks coming directly from Z^0 decay (*e.g.*, one third of the total experimental error on R_b comes from the uncertainty on $g_{Q\bar{Q}}$). Gluon splitting to heavy quarks is a background also to Higgs searches, since the strongest Higgs couplings are to heavy fermions. The significance of the Higgs excess in ALEPH at $m_H = 116\ GeV/c^2$ has a total systematic uncertainty of $\pm 0.15\sigma$, of which the gluon splitting contribution is $\pm 0.04\sigma$. Furthermore, an accurate knowledge of gluon splitting rates is needed at LHC, where a large fraction of heavy quark events will be produced *via* this process.

This analysis is based on a lepton tag. A selection based on the full LEP I data recorded in ALEPH ($\approx$ 4 millions $e^+e^- \to Z^0 \to q\bar{q}$ events) is designed, from which only events with a lepton in the jet of smallest momentum are retained. The principle is that, due to phase space considerations, the jet which contains most of the final products of the process $g \to c\bar{c}$ is expected to be the one with the smallest momentum.

Another important selection criterion is obtained by cutting on the thrust of the event, since a signal event is expected to be more spherical than a typical $Z^0 \to q\bar{q}$ event. After that, all the events are forced to clusterize in three jets. The last in momentum ordering is considered the "gluon jet" and its properties are used to discriminate the signal from the background, in conjunction with the properties of the lepton, by means of a neural network.

The present dissertation is organized as follows.

The first chapter is devoted to the *Standard Model*, along with the theory of strong interactions and a review of the most important measurements performed at LEP I. In chapter 2 the physical quantity which is the topic of this thesis is described. In chapter 3 the ALEPH apparatus is shown in all its components. In chapter 4 the methods to identify the particles and reconstruct their trajectories are described, as well as the standard algorithms used to cluster the particles in jets and to efficiently discriminate between long and short lived hadrons. Chapter 5 is a general overview on the neural network method, with particular attention to the kind of network used in this measurement. In chapter 6 the analysis and its results are described in detail, while in chapter 7 the main systematic errors are estimated and the results of some consistency checks are shown. The final result and its influence on other measurements are shown in the final chapter.

My original contribution to this dissertation fully covers chapters 6, 7 and 8. Also Sec. 4.7.4 describes original work of the author. My analysis has been already described in an ALEPH article [1].

Chapter 1

Introduction

This chapter is devoted to a brief description of the Standard Model (the theoretical frame of subnuclear physics) and how we arrived to it, together with a short overview of the theory of strong interactions and a description of the main measurements performed at LEP.

1.1 The quest for the fundamental constituents of matter

The goal of particle physics is the knowledge of the fundamental constituents of matter and of their interactions. One of the earliest attempts to describe matter as a combination of a small number of basic constituents is due to Empedocles of Agrigentum (Sicily), who imagined, about twenty-four centuries ago, four basic elements: air, water, fire and earth. Besides these four "roots", Empedocles postulated something called Love (*philia*) to explain the attraction of different forms of matter, and of something called Strife (*neikos*) to account for their separation. So, this early theory already contained some of the main features of the modern understanding of matter: a limited number of distinct constituents which interact via both attractive and repulsive forces. However, Empedocles described matter as continuous and infinitely divisible.

Another surprising anticipation of the modern description of matter was, in the same century, the atomic theory by Democritus of Abdera (who expanded the idea of his master Leucippus). He rejected the infinite divisibility of matter, postulating the existence of "atoms", defined as the indivisible constituents of everything. In Democritus' view there is no limit to the number of varieties of atoms, which can be in any shape and size, and there is no exhaustive explanation (for modern scientific standards) of the forces acting on and among them.

In the last centuries the quest for the fundamental constituents of matter pertained to experimental scientists more than to philosophers. Isaac Newton gave qualitative explanations of Boyle's law by assuming a kinetic theory of gases based on atomism. The foundations of a modern atomic theory of matter came with John Dalton, while Amedeo Avogadro differentiated between atoms and molecules. In 1865 Joseph Loschmidt used the equations of the kinetic theory of gases to make the first determination of Avogadro's number and of molecular diameters. In 1869 Dmitri Ivanovich Mendeleev and Julius Meyer independently introduced the *Periodic Table of the elements*, a concise summary of years of experimental and theoretical chemistry. Other support for the atomic theory came from "Brownian motion", discovered in 1827 by Robert Brown and explained in 1905 by Einstein in an atomic frame. The reality of atoms was no more in doubt.

The large number of them (92 naturally occurring elements) and the regularity in their properties (e.g. their masses) hinted at an underlying structure. The discovery of the electron in 1897 by Joseph John Thomson and of the nucleus by Ernest Rutherford, Hans Geiger and Ernest Marsden between 1911 and 1913 yielded a picture of the atom as a microscopic analogous of the Solar System, with a small central massive core surrounded by orbiting electrons. The model was made coherent, with use of some quantization principles, by Niels Bohr in 1913.

The problem of the structure of the nucleus itself was still open, at that time, but progress was going on in the study of radioactivity: in 1903 Rutherford with Frederic Soddy showed that every radioactive process is a transmutation of elements and in 1909 Rutherford and Thomas Royds showed that alpha particles are doubly ionized helium atoms; Henri Becquerel had shown in 1900 that beta rays are electrons. Rutherford was also the author, in 1919, of the first artificial transmutation of an element, producing hydrogen and oxygen by alpha-particle bombardment of nitrogen.

When Quantum Mechanics reached full development, several problems concerning the structure of matter were solved. In 1926 Erwin Schrödinger proposed the wave-mechanical theory of the hydrogen atom; in 1928 Edward Condon, Ronald Gurney and George Gamow solved the nuclear problem of alpha-particle emission by means of wave mechanics; several atomic and molecular systems were understood with the help of the Schrödinger's equation even in absence of exact solutions, using approximation methods.

But Quantum Mechanics raised a new problem. The simplest and mostly accepted explanation of the nuclear structure made use only of the two known particles, proton and electron, with a number of protons equal to the "atomic number", bound from a still unknown nuclear force, and some electron in the nucleus itself to explain why the charge of the nucleus in electron units differs from the atomic number; but the "uncertainty principle" stated by Werner Heisenberg in 1927 implied that an electron, forced in the small volume of a nucleus, would have an average kinetic energy sufficient to escape very quickly. A new idea was needed, and one of the proposals was the existence of a new particle, the "neutron", having a mass nearly equal to that of the proton but electrically neutral. This new particle was discovered in 1932 by James Chadwick. Two years before, W. Bothe and H. Becker had observed a puzzling penetrating radiation from beryllium bombarded with alpha particles, but missed the right explanation in terms of emitted neutrons.

The neutron was just the first of a long series of particles discovered after their prediction based on theoretical considerations. In 1928 P.A.M. Dirac developed Relativistic Quantum Mechanics, which led him to the prediction of the "positron", an electron with positive charge that was then observed by Carl Anderson in cosmic rays in 1932. In 1931 Pauli predicted the existence of a new very light neutral particle (named "neutrino" by Enrico Fermi) to explain the energy spectrum of electrons produced in beta-decay processes. The neutrino (ν) was discovered in 1956 by Frederic Reines and Clyde Lorrain Cowan. In 1935 Hideki Yukawa announced his theory of nuclear binding forces involving the postulate of a particle having a mass intermediate between the electron and the proton and called "meson" (originally "mesotron") and in 1947 Cecil Powell, G.P.S. Occhialini and Cesare Lattes discovered the pi-meson or pion (π), the first meson, responsible for intra-nuclear interactions.

But a new particle with similar mass, nowadays called "muon" (μ), had already been observed in 1936 by Carl Anderson and Seth Neddermeyer during cosmic ray research, and mistakenly interpreted as the particle predicted by Yukawa. The mistake was recognized only when Marcello Conversi, Ettore Pancini and Oreste Piccioni showed, between 1943 and 1947, that the muon has a much weaker interaction with matter than was expected for the carrier of the strong nuclear force. So the muon was added to the list of the fundamental constituents of matter, despite it was not needed by any of the theories of the time (inspiring the famous quote from Isidor Rabi: "Who ordered it?").

In 1947 a new and unexpected whole family of particles, the "V-particles" (now known as K-mesons) and the hyperons was discovered by George Rochester and Clifford Butler. Those (lately called "strange" particles) are strongly interacting particles, like nucleons (protons, neutrons) and pi-mesons, having a new quantum number, called "strangeness" by Murray Gell-Mann, conserved in strong interactions (so that they can be produced in particle-antiparticle pairs in nuclear reactions) but not in weak interactions (allowing them to decay, in a time scale too long to be due to strong or electromagnetic forces).

This was just the beginning of a plethora of new particles that was discovered, many in cosmic rays experiments, in the 1940s and 1950s. More than one hundred hadrons (generic name for particles sensitive to strong nuclear interaction) were soon known. The list of the "fundamental" particles was quite too long: it was foreseeable (and hoped) that a simplification should arise, like the one that had led to explain the 92 atomic nuclei in terms of protons and neutrons. The first step towards this simplification was the classification of the hadrons based on Group Theory by Murray Gell-Mann and Yuval Ne'eman in 1961 in an analogous way to the Periodic Table of Mendeleev. This scheme was not based on any underlying theory of fundamental structure, nor was derived from any abstract principle. It simply provided a concise representation that exhibited symmetry and order and, additionally, predictive power. In fact, as the Periodic Table had permitted to predict the existence of some elements long before their discovery, this classification predicted the particle Ω^-, which was subsequently discovered in 1964 at Brookhaven. The success of this scheme - described by the group $SU(3)$, the special unitary group of dimension 3 - encouraged physicists to look for underlying reasons for the patterns. In particular, it led Gell-Mann and G. Zweig in 1964, independently of each other, to postulate that all the known hadrons were composed of three elementary particles called the *up*, *down* and *strange* quarks, having electric charge $+2/3$, $-1/3$ and $-1/3$ respectively, in electron charge units. In this model the mesons are bound states of a quark and an antiquark, and the baryons are composed of three quarks or three antiquarks. The proton, for example, is a uud state while the neutron is udd. All "strange" particles contain at least one s or one $\bar{s}$ (i.e. anti-s).

The strongest confirmation for the quark model came from the discovery of the compositeness of nucleons by means of deep inelastic scattering experiments. In 1967 the Stanford Linear Accelerator Center (SLAC) began a study of inelastic scattering of 20 GeV electrons on a proton target, whose results were understandable only in terms of point-like charged objects in the proton.

In the early 1970's Nambu, Fritzsch and Gell-Mann proposed a theory of the strong interaction, the Quantum Chromodynamics (QCD, see Sec. 1.3), in which the strong force between quarks is mediated by the gluon (g), a massless electrically neutral particle. The strong charge is named "color" because of its occurrence in three qualities, called "blue", "red" and "green" in analogy with optics. A color is neutralized by the corresponding anticolor (e.g., "blue" is neutralized by "antiblue") or by the other two colors (that is, "blue", "red" and "green" form a color-neutral object). In QCD neither quarks nor gluons are color-neutral, and they cannot exist as free particles. At the end of the decade, direct evidence for gluons was found at the DESY laboratory in Hamburg. Politzer and, independently, Gross and Wilczek showed that in this theory the strong interactions have unusual properties (including "asymptotic freedom") that are essential to understand data in scattering and other processes.

The process leading from free quarks to the observed hadrons will be better described in Sec. 4.1.

The model with three quark "flavours" (up, down, strange) was recognized as insufficient since it raised the problem of the "Flavour Changing Neutral Currents" ($FCNC$) like $s \to d$. This kind of process had never been observed in any laboratory, but the theory of Glashow, Weinberg and Salaam unifying electromagnetic and weak forces, which worked fine if applied to leptons, when applied to the quarks required the occurrence of $FCNC$'s. In 1970 Glashow, Iliopoulos and Maiani showed that a fourth quark with proper characteristics could provide the cancellations needed to have a cross section for $FCNC$ processes low enough to justify their non observation. This was the "charm" (c) quark, already proposed by Bjorken and Glashow to complete the second quark "family" in analogy with the lepton family composed by the muon and its neutrino (discovered in 1963 by Lederman, Schwartz and Steinberger). The c quark was later discovered in 1974 with the production of the J/ψ meson (a $c\bar{c}$ bound state) at Brookhaven and, independently, at SLAC.

The so called "Standard Model" was established, with matter particles grouped in two "families" (e,ν_e, u and d in the lightest family, μ,ν_μ, c and s in the heaviest). But just a year later, in 1975, the first member of a third family, the τ lepton, was discovered by Martin Perl in SLAC data. The third family, at least for quarks, was already desired, since without it the Standard Model could not explain (unless introducing a new fundamental and yet unknown force) the Charge and Parity (CP) violation in the neutral K's weak decays, a tiny effect known since 1965 and explained by Kobayashi and Maskawa in 1973 with the help of an extension of Cabibbo's idea of mixing between "down-type" (d and s) quarks. Only a mixing between three quarks (described by the so called "CKM matrix") can allow CP violation, so a down-type fifth quark is needed; and of course, to avoid the occurrence of FCNC processes, an up-type sixth quark becomes necessary.

At Fermilab in 1977 Lederman and collaborators found the fifth quark, the "beauty" or "bottom" (b) quark, and the third family was then completed with the "truth" or "top" (t) quark in 1995 and the ν_τ in 2000, at Fermilab again. Little doubt was present, anyway, for the existence of the last two particles after that the existence of the third lepton and quark families had been established.

The current list of what are nowadays considered the fundamental constituents of matter is shown in table 1.1. Table 1.2 lists the carriers of the fundamental forces. The first ones all have spin 1/2 in $\hbar$ units, so that they are fermions (i.e. they obey the Fermi-Dirac statistics, implying the Pauli Exclusion Principle), while the others have integer spin in the same units, so that they are bosons (i.e. they obey the Bose-Einstein statistics). $W^{\pm}$ and Z^0 (predicted by the unified "electroweak" theory of Glashow, Weinberg and Salam) have been discovered at CERN in 1983 by Carlo Rubbia's group.

The only missing particle in the Standard Model is, at present, the Higgs boson, needed to explain the occurrence of non zero particle masses via the *spontaneous symmetry breaking* mechanism.

After so many years no answer has been found to Rabi's question, originally concerning the muon: "Who ordered it?", that is, why are there three copies of every fundamental matter particles[1]? One of the goals of an eventual Theory Of Everything would be the explanation of this scheme.

1.2 Standard Model

In the current understanding, the interactions of elementary particles (except for what concerns gravity) are described by the Standard Model [3, 4, 5], a gauge field theory based on the group $G = SU(3)_c \times SU(2)_L \times U(1)_Y$ with a spontaneous breakdown of symmetry

[1] The occurrence of further families is now disfavored, after that the LEP data, between 1989 and 1995, showed that only three neutrinos exist lighter than one half of the Z^0 mass (see Sec. 1.4.1); since the known neutrinos are the lightest members of their families and are almost massless, this is usually considered an indication that no other family exists at all.

Leptons			Quarks		
Particle	Charge/e	Mass	Particle	Charge/e	Mass
e	-1	511 KeV	up (u)	$+2/3$	$1.4 - 4.5$ MeV
ν_e	0	< 3 eV	down (d)	$-1/3$	$5 - 8.5$ MeV
μ	-1	105.6 MeV	charm (c)	$+2/3$	$1.0 - 1.4$ GeV
ν_μ	0	< 0.19 MeV	strange (s)	$-1/3$	$80 - 155$ MeV
τ	-1	1.77 GeV	top (t)	$+2/3$	174.3 GeV
ν_τ	0	< 18.2 MeV	bottom (b)	$-1/3$	$4.0 - 4.5$ GeV

Table 1.1: Standard Model matter particles (fermions) [2].

Particle	Charge/e	Mass	Spin
photon (γ)	0	0	1
W^+	$+1$	80.4 GeV	1
W^-	-1	80.4 GeV	1
Z^0	0	91.2 GeV	1
gluon (g)	0	0	1
graviton (?)	0	0	2

Table 1.2: Standard Model force carriers (bosons) [2].

(via the *Higgs mechanism*) which leaves $SU(3)_c \times U(1)_{em}$ as "visible" symmetry. The term $SU(2)_L \times U(1)_Y$ describes the electroweak interactions, the term $SU(3)_c$ the strong interactions, whose corresponding theory, Quantum Chromodynamics (QCD), has the quarks as matter fields (fermions) and the gluons as exchange particles (gauge bosons). The exchange particles of the $SU(2)_L \times U(1)_Y$ gauge theory are four bosons (three, $W^{1,2,3}$, in correspondence to the $SU(2)$ group generators and one, B, for the $U(1)$) which mix to give γ, W^+, W^-, Z^0 as physical (observable) fields:

$$W^+ = (W^1 - iW^2)/\sqrt{2} \tag{1.1}$$

$$W^- = (W^1 + iW^2)/\sqrt{2} \tag{1.2}$$

$$Z = W^3 cos\theta_w - Bsin\theta_w \tag{1.3}$$

$$A = W^3 sin\theta_w + Bcos\theta_w \tag{1.4}$$

where θ_w is named "mixing parameter" or "Weinberg angle". Due to the Higgs mechanism the W^+, W^- and Z^0 quanta have non-zero mass while the photon is massless.

Fermions, as said, can be grouped in three families (see Tab. 1.1), each containing two quark "flavours", sensitive to the strong interactions, and two leptons (a neutrino and a charged lepton) which are not. Leptons have a conserved quantum number, the *leptonic* *number*, defined as follows:

$$L = N(l^-) + N(\nu_l) - N(l^+) - N(\bar{\nu}_l)$$

where l is a generic lepton.

Moreover, every lepton family has a corresponding conserved quantum number. For the first generation it is the electronic number ($L_e = N(e^-) + N(\nu_e) - N(e^+) - N(\bar{\nu}_e)$), for the second it is the muonic number, for the third the tauonic number. This is not the case for the quarks, since the weak interactions allow transitions between different generations (e.g. $b \rightarrow c$), but there is a conserved quantum number also in the quark sector: the baryonic number, defined as the number of quarks (of any flavour) minus the number of antiquarks.

Quarks have also another degree of freedom called "color", as said in the previous section, which has the role of the source of the strong force in QCD, similarly to the electric charge for the electromagnetic force in Quantum Electro-Dynamics. $SU(3)$ requires eight gluons, each with a color and an anticolor (e.g. red-antiblue). Self-interaction of gluons is allowed due to the non-Abelian character of the theory (in contrast with QED).

Quarks and gluons are "confined" into hadrons, i.e. color singlets, which are actually observed; there is no way, according to QCD, to detect free quarks or gluons, as well as any composite state which is not a color singlet, and this has been confirmed by decades of searches at the accelerators. The transition from quarks and gluons to hadrons is not completely understood starting from the basic principles of QCD. In spite of this, QCD is well tested in the domain of high energies and high momentum transfers, where the perturbation theory is reliable due to the weakening of the QCD coupling (α_s) as the transferred 4-momentum, Q, increases.

1.3 Strong Interactions

1.3.1 The Lagrangian of Strong Interactions

The QCD Lagrangian density is given by

$$\mathcal{L}_{QCD} = \sum_{flavours} \bar{q}_a (i\gamma^\mu D_\mu - m_q)_{ab} q_b - \frac{1}{4} F^A_{\mu\nu} F^{A\mu\nu} \tag{1.5}$$

where the sum runs over the N_f different flavours of the quarks. $F^A_{\mu\nu}$ is the field strength tensor derived from the gluon field $\mathcal{A}^A_\mu$ as

$$F^A_{\mu\nu} = [\partial_\mu \mathcal{A}^A_\nu - \partial_\nu \mathcal{A}^A_\mu - g_s f^{ABC} \mathcal{A}^B_\mu \mathcal{A}^C_\nu] \tag{1.6}$$

where the capital indices run over the eight color degrees of freedom of the gluon field, g_s is the coupling constant which determines the strength of the interaction between colored quanta, and f^{ABC} are the structure constants of the color group $SU(3)$. The third term in Eq. 1.6 shows the non-Abelian nature of QCD, which gives rise to gluon self-interactions and, ultimately, to asymptotic freedom.

The quark fields q_a in Eq. 1.5 are in the triplet representation of the color group and D is the covariant derivative, which acting on triplet fields takes the form:

$$(D_\mu)_{ab} = \delta_{ab}\partial_\mu + ig_s(t^C \mathcal{A}^C_\mu)_{ab} \tag{1.7}$$

where the generators t are matrices in the fundamental representation of $SU(3)$ and fulfill the relation

$$[t^A, t^B] = if^{ABC}t^C \ . \tag{1.8}$$

By convention the normalization of the $SU(N)$ matrices is chosen to be

$$Tr(t^A t^B) = T_R \delta^{AB}, \ \ T_R = \frac{1}{2} \ . \tag{1.9}$$

With this choice, the color matrices for $SU(N)$ obey the following relations:

$$\sum_A t^A_{ab} t^A_{bc} = C_F \delta_{ac}, \ \ C_F = \frac{N^2-1}{2N} \tag{1.10}$$

$$\sum_{A,B} f^{ABC} f^{ABD} = C_A \delta^{CD}, \ \ C_A = N \ . \tag{1.11}$$

Thus for the specific case of $SU(3)$ we have

$$C_F = \frac{4}{3}, \ \ C_A = 3 \tag{1.12}$$

which are called the *color factors*. They are related to the emission of a gluon by a quark (Fig. 1.1a) and the splitting of a gluon into two other gluons (Fig. 1.1b), respectively.

The QCD Lagrangian in Eq. 1.5 leads to three elementary vertices shown in Fig. 1.1. Amplitudes for the various processes involving quarks and gluons can be obtained using

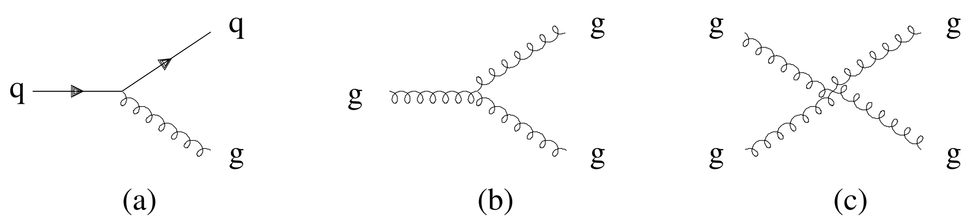

Figure 1.1: Elementary vertices of QCD: (a) quark-gluon vertex, (b) triple gluon vertex, (c) four-gluon vertex.

the Feynman rules derivable from the Lagrangian. The amplitudes for $q\bar{q}g$ and ggg in Fig. 1.1a and Fig. 1.1b are proportional to the coupling g_s, whereas the four-gluon vertex (Fig. 1.1c) is proportional to g_s^2.

The Lagrangian density in Eq. 1.5 has the property of *gauge invariance*, since it remains invariant under a local $SU(3)$ *gauge transformation*:

$$q_a \rightarrow U_{ab} q_b \tag{1.13}$$

$$\bar{q}_a \rightarrow U^*_{ab} \bar{q}_b \tag{1.14}$$

$$\mathcal{A}^A_\mu \rightarrow \mathcal{A}^A_\mu + \partial_\mu \omega(x) + g_s f^{ABC} \omega^B(x) \mathcal{A}^C_\mu \tag{1.15}$$

where $\omega^A(x)$ $(A = 1, ..., 8)$ are arbitrary real quantities which depend in general on the space time coordinates $x = (t, \vec{x})$. A gluon mass term of the form $m_g^2 \mathcal{A}^A_\mu \mathcal{A}^{\nu A}$ would violate gauge invariance and hence is not allowed.

1.3.2 The running coupling

In a quantum field theory the calculation of a dimensionless observable R as a perturbation series in $\alpha_s = g_s^2/4\pi$, where R depends on a large energy scale Q, requires renormalization to remove ultraviolet divergences. Such divergences come from loop corrections, such as those represented by the Feynman diagrams in Fig. 1.2.

Through renormalization the divergent terms are absorbed into a redefinition of the couplings, the masses or the field normalizations. The "bare" values of these quantities are not physically observable, while the renormalized values are measurable. This process introduces a mass scale μ, at which the subtractions which remove the divergences are performed. R depends on the non-constant ratio Q/μ. The renormalized coupling also

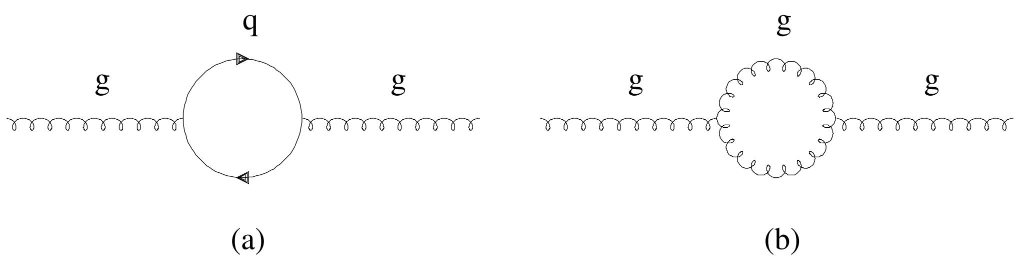

Figure 1.2: Loop corrections to the gluon propagator: (a) quark loop, (b) gluon loop.

depends on μ.

Since μ is an arbitrary parameter, R cannot depend on μ when the coupling is fixed. Moreover, since R is dimensionless, it can only depend on Q/μ or equivalently Q^2/μ^2 and on the renormalized coupling α_s. Hence

$$\mu^2 \frac{d}{d\mu^2} R\left(\frac{Q^2}{\mu^2}, \alpha_s\right) \equiv \left[\mu^2 \frac{\partial}{\partial \mu^2} + \mu^2 \frac{\partial \alpha_s}{\partial \mu^2} \frac{\partial}{\partial \alpha_s}\right] R = 0 \tag{1.16}$$

which is called the renormalization group equation. Introducing $\tau \equiv \ln\left(\frac{Q^2}{\mu^2}\right)$ and $\beta(\alpha_s) \equiv \mu^2 \frac{\partial \alpha_s}{\partial \mu^2}$, the renormalization group equation can be written as

$$\left[-\frac{\partial}{\partial \tau} + \beta(\alpha_s) \frac{\partial}{\partial \alpha_s}\right] R = 0 \tag{1.17}$$

which is solved by defining the running coupling $\alpha_s(Q)$,

$$\tau = \int_{\alpha_s}^{\alpha_s(Q)} \frac{dx}{\beta(x)} \tag{1.18}$$

where $\alpha_s(\mu) \equiv \alpha_s$. Thus all scale dependence in R comes from the running of $\alpha_s(Q)$. A change in the renormalization scale is compensated by a change of the coupling, and the physical observable R remains independent of the unphysical scale μ^2. However, this only holds if R is calculated at all orders of α_s, otherwise an explicit scale dependence appears.

The running of the QCD coupling, α_s, is determined by the β function, which has the expansion:

$$\beta(\alpha_s) = -b\alpha_s^2(1 + b'\alpha_s + \mathcal{O}(\alpha_s^2)) \tag{1.19}$$

where

$$b = \frac{11C_A - 2N_f}{12\pi} \; ; \quad b' = \frac{17C_A^2 - 5C_A N_f - 3C_F N_f}{2\pi(11C_A - 2N_f)} \tag{1.20}$$

with N_f the number of active flavours, where active means having $m_q \lesssim Q$. Thus for $5 \lesssim Q \lesssim 175$ GeV, $N_f = 5$.

The β function in general depends on the renormalization scheme used, hence the running coupling. Nevertheless the first two terms of the expansion 1.19 are scheme independent. Neglecting b' and higher order coefficients in Eq. 1.19 the following solution can be extracted:

$$\alpha_s(Q^2) = \frac{\alpha_s(\mu^2)}{1 + \alpha_s(\mu^2) b \ln \frac{Q^2}{\mu^2}} \ . \tag{1.21}$$

Quark loop diagrams contribute to the negative N_f term in b (Eq. 1.20) while gluon loop diagrams give a positive C_A contribution which makes an overall negative β function. This is in contrast to QED, where the b coefficients have opposite signs. Then, as Q becomes large, $\alpha_s(Q)$ decreases to zero. This property of QCD, which depends on the sign of b, is called asymptotic freedom. It is this property that allows reliable predictions from perturbation theory for processes involving high momentum transfers. In QED, where b is negative, the coupling increases at large Q.

1.3.3 The Lambda parameter

Perturbative QCD permits to calculate α_s as a function of Q, given its value (to be determined experimentally) at some reference scale. It is customary to use its value at $Q = M_Z$ as the fundamental parameter, since this is a convenient reference scale large enough to be in the perturbative regime.

However, it is also useful to express $\alpha_s(Q)$ in terms of a dimensionfull parameter, Λ, coming out as a constant of integration:

$$\ln\frac{Q^2}{\Lambda^2} = -\int_{\alpha_s(Q)}^{\infty} \frac{dx}{\beta(x)} = \int_{\alpha_s(Q)}^{\infty} \frac{dx}{bx^2(1 + b'x + ...)} \ . \tag{1.22}$$

Then, in perturbative theory, $\alpha_s(Q) \to \infty$ as $Q \to \Lambda$. Thus Λ has the physical meaning of the scale of the breakdown of the perturbative approach.

At next-to-leading order (NLO) the coupling constant can be written in terms of this parameter as follows:

$$\alpha_s(Q) = \frac{1}{b\ln(Q^2/\Lambda^2)} \left[1 - \frac{b'}{b} \frac{\ln\ln(Q^2/\Lambda^2)}{\ln(Q^2/\Lambda^2)} \right] \tag{1.23}$$

The Λ parameter depends on the number of active flavours, N_f. For $\alpha_s(M_Z) = 0.120$, Eq. 1.23 gives a $\Lambda^{(5)}$ value of about 100 MeV.

1.3.4 From partons to hadrons

The process $e^+e^- \rightarrow$ *hadrons* can be viewed as proceeding through the four phases shown in Fig. 1.3. How all these phases of the process are simulated using Monte Carlo techniques is described in Sec 4.1.1.

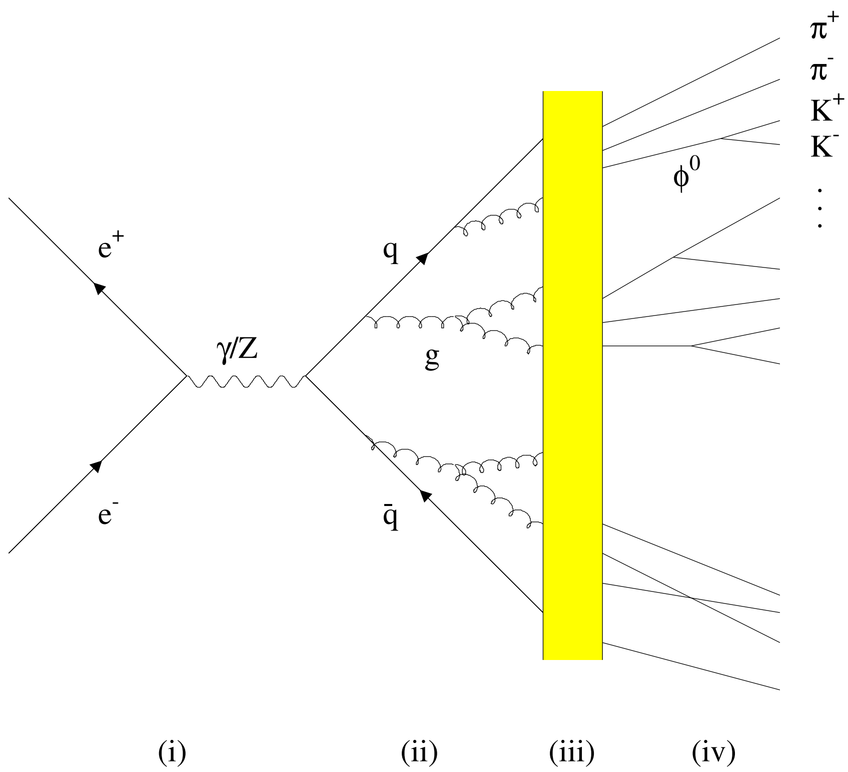

Figure 1.3: The reaction $e^+e^- \rightarrow$ *hadrons* viewed in four phases: (i) e^+e^- annihilation into a Z^0 boson, which decays into a primary quark-antiquark pair; (ii) radiation of gluons from quark and antiquark according to perturbative QCD; (iii) non-perturbative transformation of partons into color-neutral hadrons; (iv) decay of short-lived hadrons.

The first phase is the reaction $e^+e^- \rightarrow q\bar{q}$, computable with very high precision in the theory of electroweak interactions.

This is followed by the radiation of hard gluons, which can be described reliably by perturbative QCD. For predictions of final states with larger number of partons, one can use the *parton shower* approach, based on the *leading logarithm approximation*. The main idea is to reorganize the perturbative expansion so that the terms with leading collinear singularities are summed to all orders [6]. The result can be reinterpreted as a sequence of parton branchings $q \to qg$, $g \to gg$ and $g \to q\bar{q}$. The virtual mass Q of the partons decreases after each decay, and this leads to a corresponding increase in $\alpha_s(Q^2)$.

The shower is terminated at some virtuality cut-off Q_0, below which $\alpha_s(Q^2)$ becomes so large that perturbation theory is no longer valid. At this point, other calculation techniques (e.g. phenomenological models) must be invoked to describe the production of final state hadrons (*hadronization* or *fragmentation*). If both the perturbative description and the models were perfect, the value of Q_0 would be arbitrary. In practice, Q_0 is adjusted to achieve the best overall description of the data; typical values are in the range $0.6 - 1.6$ GeV, corresponding to $\alpha_s(Q^2) \approx 0.3 - 0.5$.

An important aspect of the hadronic events is that, at the large $\sqrt{s}$ values considered, the final state hadrons generally form *jets*, i.e. they are not arbitrarily spread out in phase space, but stay rather close together. The directions and energies of these jets are in close correspondence with those of the primary partons. More precisely, hadrons are formed out of the color field with limited transverse momentum. Therefore, the higher the energy of the primary parton, the stronger is the collimation of hadrons around its direction. An event where the primary quarks from Z^0 decay do not radiate any energetic gluons will typically appear as two back-to-back well defined jets (see Fig. 1.4), whereas events with one or more high energy gluons (like the $g \to c\bar{c}$ events studied in this thesis) will give rise to additional hadronic jets (see Fig. 1.5).

1.3.5 Semileptonic decays of heavy hadrons

The last step of the process is the decay of short-lived hadrons. While this process, at quark level, is easily and reliably described by means of the electroweak theory, some difficulties arise when considering the decay of a hadronic bound state. For hadrons composed of a heavy quark (c, b) and one or two light quarks (u, d, s) it is convenient to consider the light quark(s) as "spectator(s)" of the decay process, influencing only slightly the dynamics of the heavier quark. The pure "spectator model" considers the decaying heavy quark in the hadron as a free particle; it is usually used with the inclusion of perturbative QCD radiative corrections, and yields the following decay width for the process $H_Q \to X_q l\nu$, where H_Q is a hadron containing a Q quark (c or b) and X_q a generic

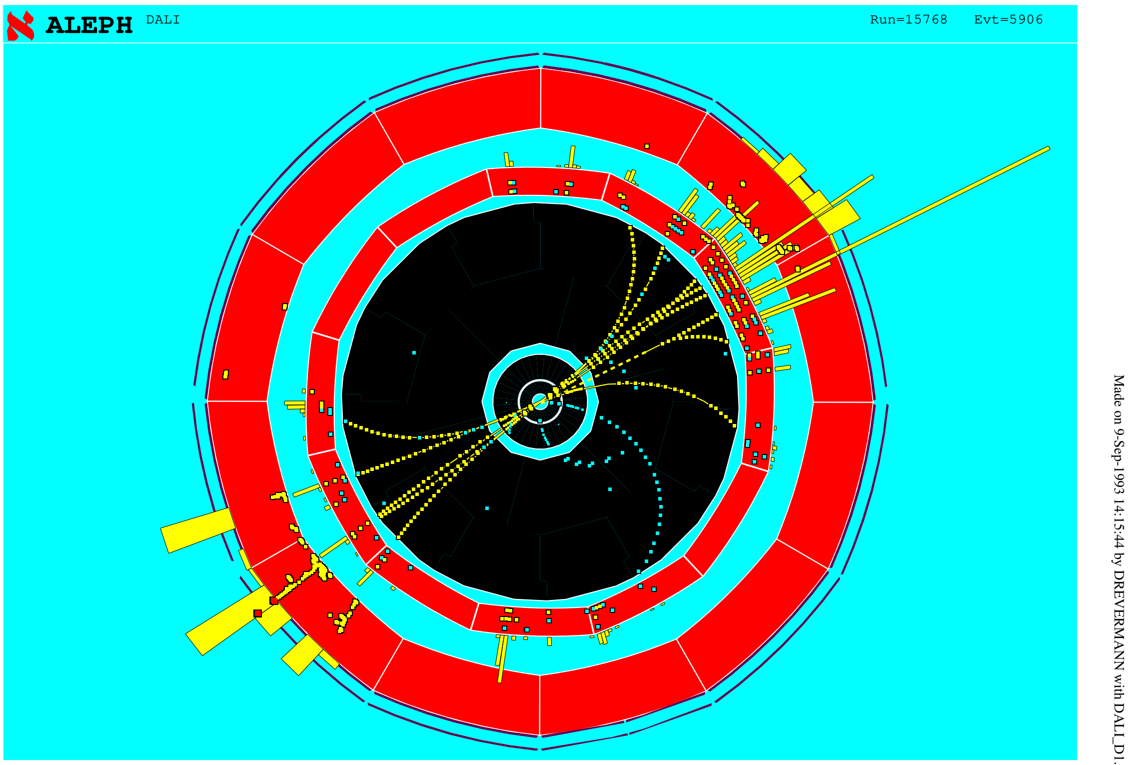

Figure 1.4: A two-jet hadronic event recorded in ALEPH.

final state containing a q quark from the Q decay:

$$\Gamma_{H_Q}(H_Q \to X_q l\nu) \approx \Gamma(Q \to q l\nu) = |V_{qQ}|^2 \left(\frac{G_F^2 m_Q^5}{192\pi^3}\right) f\left(\frac{m_q}{m_Q}\right)\left[1 - \frac{2}{3}\frac{\alpha_s}{\pi} g\left(\frac{m_q}{m_Q}\right)\right] . \tag{1.24}$$

Here V_{qQ} is an element of the CKM matrix, G_F is the Fermi constant, f is the phase space factor and g is a QCD correction related to real and virtual gluon emission ($g(z) = (\pi^2 - 31/4)(1-z)^2 + 1.5$ for single gluon correction [7]). As can be seen, the most important dependence is on the heavy quark mass m_Q.

The ACCMM model [8, 9] is an improvement on the naive free-quark decay spectator model, in which non perturbative QCD effects are taken into account kinematically. Binding effects are considered between the heavy quark and the spectator (introducing the need for m_{sp}, the spectator mass, as additional free parameter), as well as QCD corrections due to the emission of hard gluons by the quarks and to the possible exchange of gluons between the quarks in the hadron; the Fermi motion of the spectator quark inside a meson is considered introducing a gaussian distribution for the momentum $\vec{p}$ of

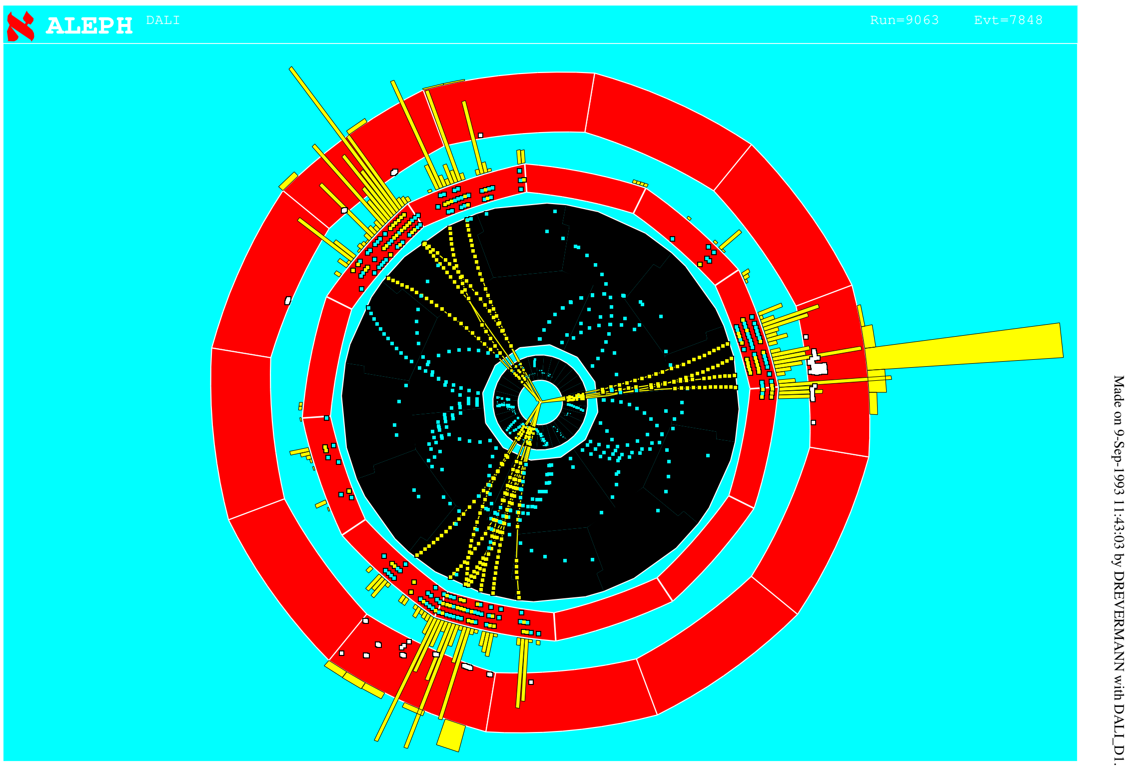

Figure 1.5: A three-jet hadronic event recorded in ALEPH.

the spectator quark, in the meson rest frame:

$$\phi(\vec{p}; p_F) = \frac{4}{\sqrt{\pi} p_F^3} \exp\left(\frac{-p^2}{p_F^2}\right) \quad , \tag{1.25}$$

where $p_F \approx 0.3$ GeV/c is the Fermi momentum, that has different values for the different meson species. The relation between p and the mass, W, of the heavy quark, considered as a virtual particle, is given by

$$W^2 = M_{H_Q}^2 + m_{sp}^2 - 2M_{H_Q}\sqrt{p^2 + m_{sp}^2} \; . \tag{1.26}$$

So, the heavy quark mass, which is a critical parameter in the free-quark model, is replaced by $W(p)$. The main parameter of the model is p_F, determined by a fit on data as explained in Sec. 7.1.4, whose value is less critical.

In this thesis the uncertainty on the modeling of the heavy quark decay is taken in account as a source of systematic uncertainty in Sec. 7.1.4, where also the uncertainty on the semileptonic "branching ratios" is separately considered for the processes $b \to l$, $b \to c \to l$ and $c \to l$, defined as $BR(b \to X) \equiv \frac{\Gamma(b \to X)}{\Gamma(b \to \mathrm{any})}$.

1.4 LEP Physics

LEP operation was divided in two phases: LEP I (1989-1995), with a centre-of-mass energy of 91.2 GeV in order to exploit the large total cross section due to the Z^0 mass peak, and LEP II (1995-2000), which scanned the energy range between the Z^0 peak and 209 GeV in order to perform precision studies on $W^{\pm}$ properties and to look for new physics phenomena (including the presence of a Higgs boson).

At LEP I energies, i.e. at the Z^0 mass peak (91.2 GeV), fermion production is dominated by the process $e^+e^- \to Z^0 \to f\bar{f}$, where f can be any fermion except the t ("top") quark, the only Standard Model fermion whose production threshold is above the Z^0 mass. In an exact treatment, one should consider the sum of the amplitudes between this process and $e^+e^- \to \gamma \to f\bar{f}$, but in the proximity of the resonance the photonic contribution to the cross section and the interference terms can be neglected for the purpose of this work.

The Z^0 boson, which, as the W's, mediates the weak interactions, is unstable and decays in $\approx 3 \times 10^{-25}$ seconds in charged leptons, neutrinos and quarks; in the first case the decay is said "leptonic", in the last "hadronic" (see Fig. 1.6).

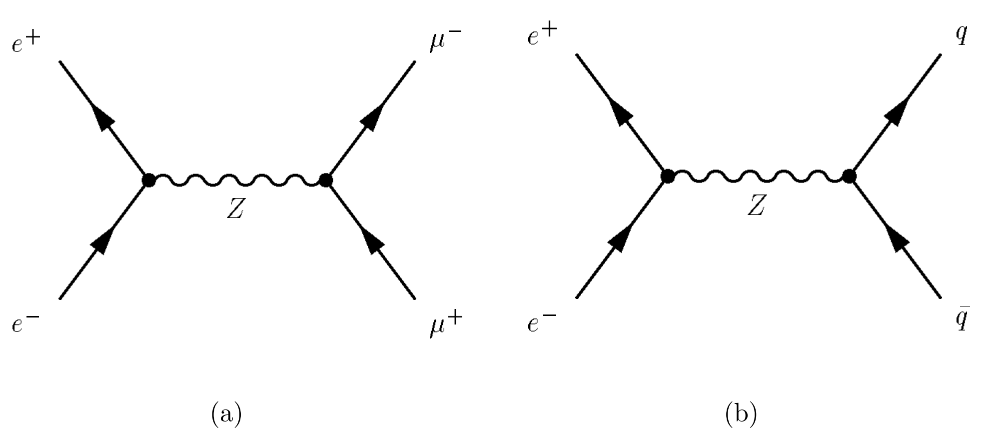

Figure 1.6: Examples of Z^0 decays: (a) leptonic, (b) hadronic.

About 70% of the Z^0 decays are hadronic, 10% leptonic, and the remaining 20% are $Z^0 \to \nu\bar{\nu}$ processes[2].

At $\sqrt{s} > 2M_W \approx 161$ GeV, W^+W^- pairs can be created, and thus much analysis work on LEP II data is devoted to the study of the $W^{\pm}$ properties. Besides that, LEP II has given an unprecedented opportunity to explore energies above the Z^0 peak looking for new physics (Higgs boson, supersymmetric particles, heavier replicas of the Z^0, proofs of compositeness, ...) in the very clean e^+e^- environment.

The following pages describe some of the most important measurements performed at LEP.

1.4.1 Number of light neutrino species

At the very beginning of its operation, in 1989, LEP was able to give the definitive answer about the number of light neutrino species (i.e. $M_\nu \leq \frac{1}{2}M_Z$). In the Standard Model, neutrinos are in correspondence with charged leptons in isospin doublets, so that this result is seen as an indication of the absence of a fourth *replica* of the electron.

This result was possible thanks to the unprecedented number of Z^0's produced at LEP already in the first months of operation, allowing precise measurements of the decay width, both total and into single fermion pairs. A strong evidence of the existence of only three neutrinos already came from cosmology, since the number of lepton families is related to the abundance of primordial chemical elements such as He^4 [10], influenced by the cooling speed of the Universe which in turn depends on the number of relativistic particles (the photon, the electron and the light neutrinos). The LEP determination, much more precise, has been the first obtained in a terrestrial laboratory.

The number of light neutrino species, N_ν, can been extracted in several ways. The main method makes use of the "invisible width" $\Gamma_{inv} \equiv N_\nu \Gamma_\nu$. The total decay width of the Z^0 is the sum of the partial widths in hadrons, charged leptons and neutrinos:

$$\Gamma_{tot} = \Gamma_h + \Gamma_l + N_\nu \Gamma_\nu \tag{1.27}$$

Moreover, the hadronic cross section σ_h^0 is given by

$$\sigma_h^0 = \frac{12\pi}{M_Z^2} \frac{\Gamma_l \Gamma_h}{\Gamma_{tot}^2} \tag{1.28}$$

yielding

$$\Gamma_{tot} = \sqrt{\frac{12\pi}{M_Z^2 \sigma_h^0} \Gamma_l \Gamma_h} \,. \tag{1.29}$$

Writing $\frac{\Gamma_l}{\Gamma_h} = B_l$ and $\frac{\Gamma_\nu}{\Gamma_l} = R$,

$$\Gamma_h(1 + B_l + N_\nu R) = \Gamma_h \sqrt{\frac{12\pi}{M_Z^2 \sigma_h^0} B_l} \tag{1.30}$$

from which

$$N_\nu = \frac{1}{R}\left[\sqrt{\frac{12\pi}{M_Z^2\sigma_h^0}B_l} - B_l - 1\right] \quad (1.31)$$

so that N_ν can be determined from the precise measurements of σ_h^0, M_Z and B_l, while $R \approx 6$ is the only theoretical input. From the whole LEP I data set, $N_\nu = 2.9841 \pm 0.0083$ [2]. This excludes the occurrence of a fourth fermion family, unless the corresponding neutrino has mass greater than half of the Z^0 mass. The uncertainty is dominated by the theoretical uncertainty on σ_h^0. Fig. 1.7 shows the remarkable agreement of the Z^0 lineshape in hadronic decays with the theoretical expectation for $N_\nu = 3$ in ALEPH data.

1.4.2 Decay fractions of the Z^0 in c and b

The measurement of the partial decay fraction $R_b = \Gamma_{b\bar{b}}/\Gamma^h_{tot}$ is very important, since the $Z \to b\bar{b}$ vertex receives a non negligible contribution from diagrams involving virtual t's (see Fig. 1.8) since b and t belong to the same isospin doublet. This makes R_b dependent on m_t (see Fig. 1.9) and a comparison is possible with the direct measurement of the top mass at the hadronic accelerators. A global electroweak fit including R_b yields $m_t = 178.1^{+10.4}_{-8.3}$ GeV [2], to be compared with the direct observation at FERMILAB yielding $m_t = 174.3 \pm 5.1$ GeV [11, 12].

The other partial decay fractions, including $R_c = \Gamma_{c\bar{c}}/\Gamma^h_{tot}$, show a much weaker dependence on m_t, given only by the contribution of $\Gamma_{b\bar{b}}$ at the denominator, and their importance lies in the fact that a deviation from the Standard Model prediction would signal "new physics", e.g. in the form of loops of new particles as corrections to the decay vertex.

The normalization to Γ_{had} instead of Γ_{tot}, which can seem more natural, is convenient since this cancels almost entirely the effects due to QCD vacuum polarization.

The world average for R_b and R_c, given by LEP I and SLC, is [13]:

$$R_b = 0.21644 \pm 0.00065\ , \quad (1.32)$$

$$R_c = 0.1718 \pm 0.0031\ . \quad (1.33)$$

As explained in Sec. 2.1, R_b and R_c measurements have to take in account a systematic contribution from the occurrence of gluon splitting into heavy quarks. In Sec. 8.3.1 these R_b and R_c results and their uncertainties will be updated with the new $g_{c\bar{c}}$ value.

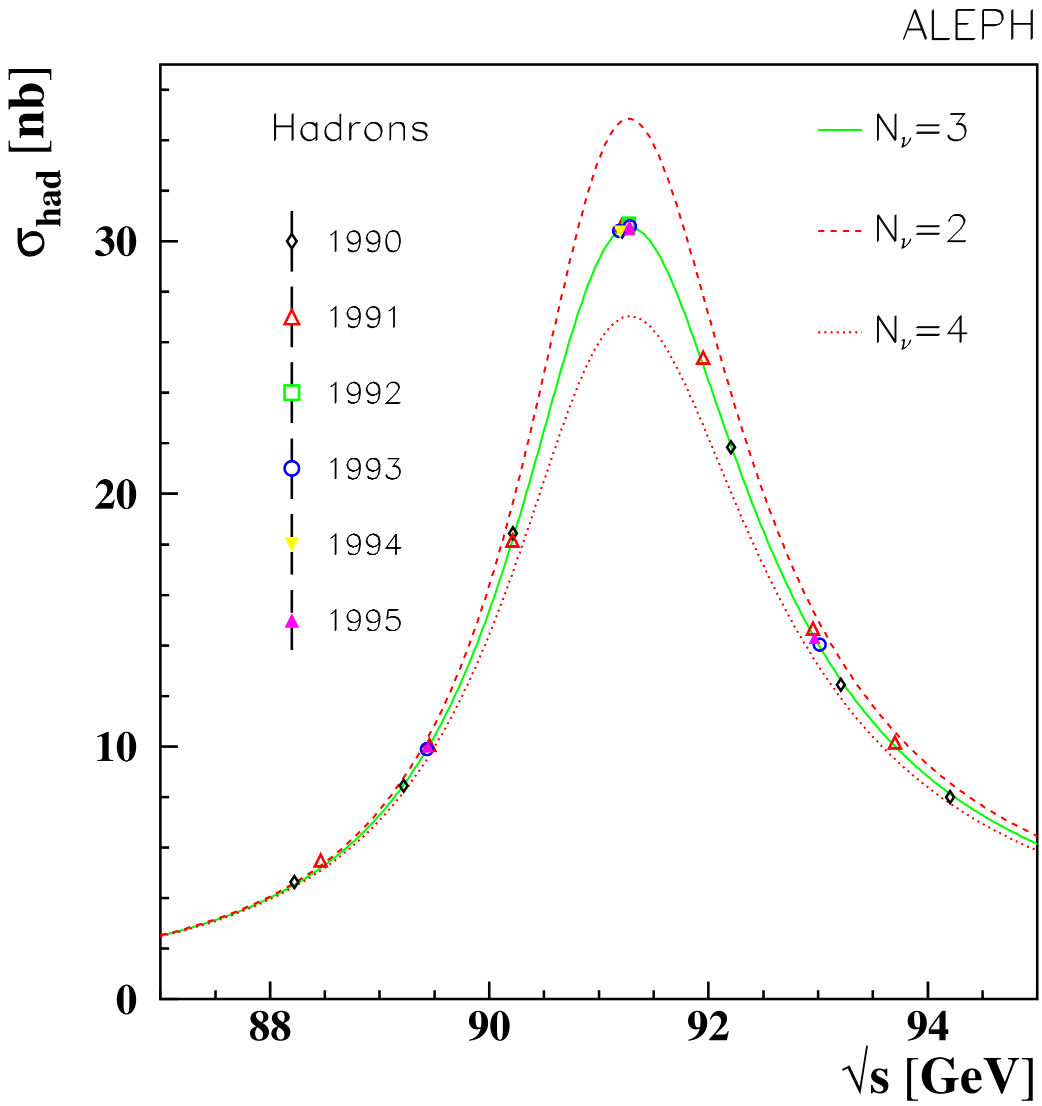

Figure 1.7: The hadronic Z^0 lineshape measured at ALEPH versus the expectation for N_ν =2,3 and 4.

1.5 α_s measurements

At LEP the strong coupling constant is measured in $e^+e^- \rightarrow hadrons$ events or in $e^+e^- \rightarrow \tau^+\tau^-$, with one or both τ's decaying hadronically.

1.5.1 Inclusive variables

One of the most important analysis strategies makes use of inclusive observables, such as the hadronic cross section, for which there is no need to analyze the particle content or the topology of the final state. Several measurements have been performed of the quantities

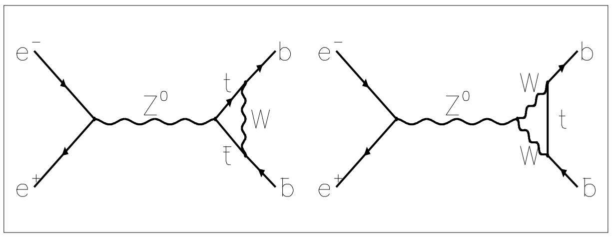

Figure 1.8: Corrections to the $Z \to b\bar{b}$ vertex involving the t quark.

R_l and R_τ, defined as

$$R_l \equiv \frac{\Gamma(Z, \to hadrons)}{\Gamma(Z \to \mu^+\mu^-)} \quad , \quad R_\tau \equiv \frac{\Gamma(\tau \to \ hadrons)}{\Gamma(Z \to \mu^+\mu^-)} \tag{1.34}$$

where the normalization to the decay width to muons is chosen to cancel the common systematic uncertainties between the hadronic channel and the very clean muonic channel. From $R_{l,\tau}$ analyses α_s is extracted by means of the QCD correction to the very precise electroweak determination of these quantities.

The QCD correction is known up to Next-to-Next-to-Leading Order (NNLO). Additional corrections are due to quark mass uncertainties and non-perturbative effects, which are very small for R_l, being suppressed as m_q^2/M_Z^2 and $1/M_Z^4$. The LEP average for R_l is 20.768 ± 0.024 [13], which translates into $\alpha_s(M_Z) = 0.124 \pm 0.004$ [14]. The main uncertainty comes from the statistical error in the muon cross section.

For τ decays ALEPH [15] and OPAL [16] measured not only R_τ but also several moments of the hadronic mass distribution, for which α_s and some non-perturbative parameters were simultaneously fitted. By translating the results in terms of the coupling at the Z^0 peak, the combination yields $\alpha_s(M_Z) = 0.1181 \pm 0.0007(exp) \pm 0.0030(theo)$ [14].

1.5.2 Event shape variables

The most accurate determinations of $\alpha_s(Q^2)$ come from "event shape" analyses.

Event shapes [17, 18] are defined as infrared and collinear safe observables characterising the structure of the final state. Infrared safe means that the quantity in question should not change if one adds one soft particle to the final state, while collinear safe means that the quantity does not change if one splits one massless particle in the final

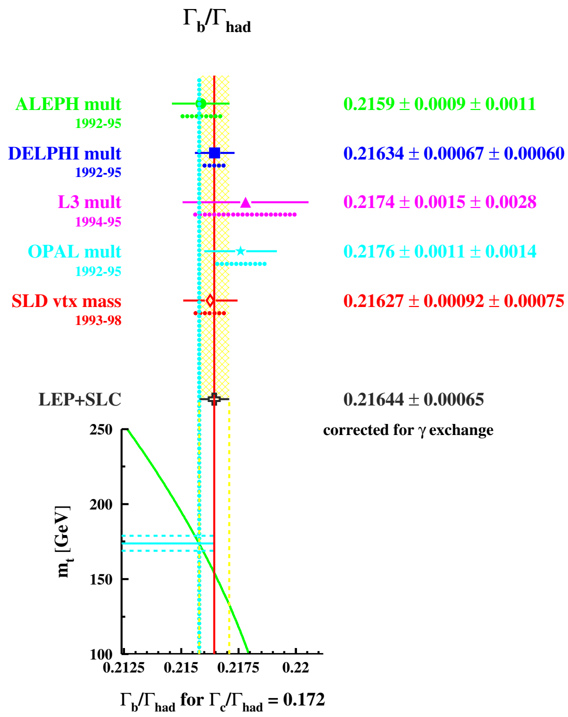

Figure 1.9: R_b dependence on m_t.

state in two massless collinear particles sharing its momentum. Thus, for example, the multiplicity (i.e. number of tracks) of the final state is neither collinear nor infrared safe, since it changes by one unit if one adds a soft particle or performs a collinear splitting of a final state particle.

Being related to the topology of the hadronic event, these observables give direct sensitivity to α_s since gluon radiation influences the topology. The most used events shape variables are:

- the "thrust"(T), defined as the maximum, for all the possible directions $\vec{n}$, of the quantity

$$T = \Sigma_a \frac{\vec{p_a} \cdot \vec{n}}{|\vec{p_a}|} , \tag{1.35}$$

  where the sum is over all the reconstructed particles;

- the C parameter, defined as a combination of the eigenvalues of the infrared safe momentum tensor

$$\theta^{ij} = \Sigma_a \frac{p_a^i p_a^j}{|\vec{p_a}|} / \Sigma_a |\vec{p_a}| ; \tag{1.36}$$

- the heavy jet mass [19], having divided the event in only two jets (e.g. requiring that jets H and L minimize the quantity $M_H^2 + M_L^2$, or simply reconstructing one jet per hemisphere, using the plane orthogonal to the thrust axis to separate the hemispheres);

Non-perturbative effects can be taken in account by simulating the hadronization by means of Monte Carlo "parton shower" algorithms [20, 21, 22], described in Sec. 4.1.1. Several measurements have been performed by LEP experiments studying event shape variables both at the Z^0 and at the higher energies reached by the accelerator, fitting the distributions predicted by perturbative QCD with non-perturbative corrections described via Monte Carlo programs. The LEP average for these analyses yields [23]

$$\alpha_s(M_Z) = 0.1198 \pm 0.0003(stat) \pm 0.0009(syst) \pm 0.0008(had) \pm 0.0046(theo) \ . \quad (1.37)$$

Another approach makes use, for the modeling of non-perturbative effects, of simple analytical expressions dependent on a small number of parameters [24], which can be interpreted [25] as moments of $\alpha_s(Q)$, averaged over small Q^2 values. For most cases, the first moment is sufficient:

$$\alpha_0(\mu_0) \equiv \frac{1}{\mu_0} \int_0^{\mu_0} dq \ \alpha_s(q) \ , \quad (1.38)$$

where μ_0 is usually taken as 2 GeV.

It is common to use either moments of the event shape variables, or their distributions. In the case of the first moments, the generic shape variable $\mathcal{F}$ can be written

$$\langle \mathcal{F} \rangle = \langle \mathcal{F} \rangle_{PT} + c_{\mathcal{F}} \mathcal{P} \ , \quad (1.39)$$

where the subscript PT labels the perturbative contribution, $c_{\mathcal{F}}$ is an observable-dependent constant, and the factor $\mathcal{P}$ is the same for all the shape variables:

$$\mathcal{P} = \frac{4C_F}{\pi^2} \mathcal{M} \frac{\mu_0}{\sqrt{s}} \left[\alpha_0(\mu_0) - \alpha_s(\sqrt{s}) + \mathcal{O}(\alpha_s^2) \right] \ ; \quad (1.40)$$

$\mathcal{M} = 1.795$, the "Milan factor", incorporates the effects of 2-loop corrections [26]. Fig. 1.10 shows the evolution with $\sqrt{s}$ of the first moments of various shape variables.

When considering distributions of the shape variables instead of their moments, the effect of non-perturbative corrections is to shift the value of the observable in the perturbative prediction[27]:

$$\frac{d\sigma}{d\mathcal{F}}(\mathcal{F}) = \frac{d\sigma^{PT}}{d\mathcal{F}}(\mathcal{F} - \mathcal{P} D_{\mathcal{F}}) \ , \quad (1.41)$$

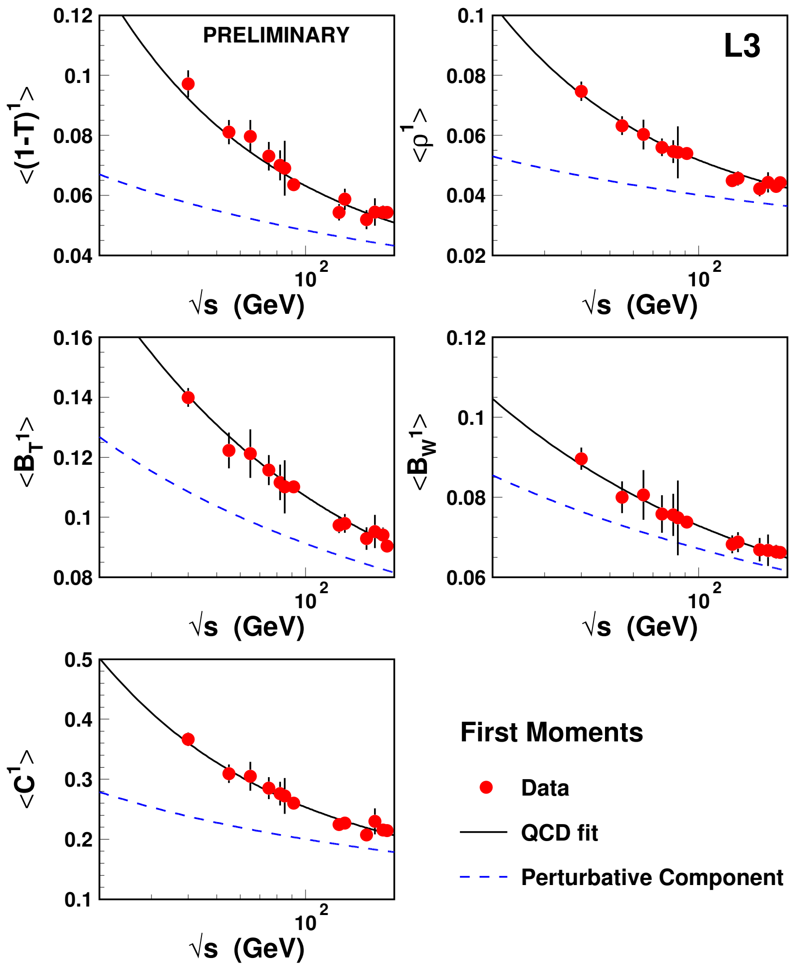

Figure 1.10: Evolution with $\sqrt{s}$ of the first moments of various shape variables, from L3.The dashed lines include only the perturbative calculation, while the solid lines come from fits including non-perturbative effects.

where $\mathcal{P}$ is the same as for the first moments, and $D_{\mathcal{F}}$ has to be calculated for each observable.

From first moments and distributions of event shape variables at LEP and JADE, the following combined result is obtained [28]:

$$\alpha_s(M_Z) \quad = \quad 0.1141 \pm 0.0012(stat)^{+0.0034}_{-0.0024}(syst)^{+0.0055}_{-0.0041}(theo) \ . \tag{1.42}$$

$$\tag{1.43}$$

1.5.3 Combination

The current world average for α_s at the Z^0 peak is [2]

$$\alpha_s(M_Z) = 0.118 \pm 0.002 \; . \tag{1.44}$$

This combination also includes results from $ep, \mu p, \nu p$ collisions (Deep Inelastic Scattering), from "quarkonia" bound states (i.e. $(c\bar{c}) = J/\psi, \psi', \psi'', \ldots$, and $(b\bar{b}) = Y, Y', Y'', \ldots$) and from $p\bar{p}$ collisions, e.g. hard jet studies, heavy quark production, and $\gamma, W^{\pm}, Z^0$ emission.

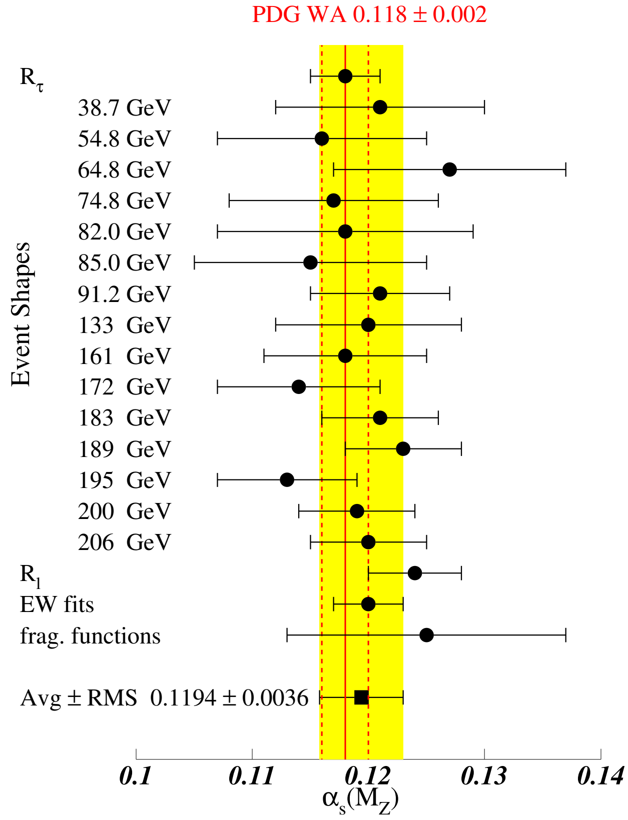

Figure 1.11: Summary of the $\alpha_s(M_Z)$ measurements performed at LEP [29].

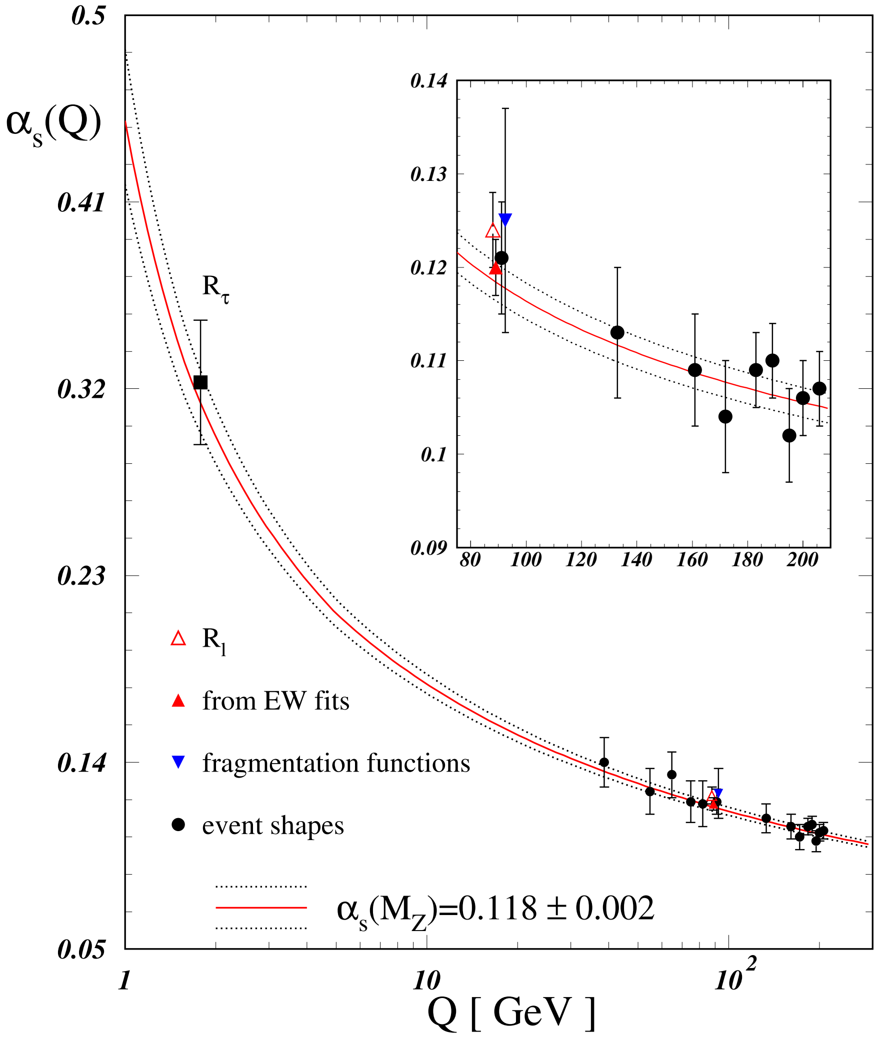

Figure 1.12: Running of α_s with $\sqrt{s}$ at LEP [29].

Chapter 2

Gluon splitting into $c\bar{c}$ pairs

2.1 Definition of the decay rate of gluons in $c\bar{c}$ pairs and importance of the measurement

This dissertation describes a measurement of the rate of $g \to c\bar{c}$ events in hadronic events at the Z^0 peak using a tag based on leptons from the decay of the c quarks from gluons.

This rate is defined as

$$g_{c\bar{c}} = \frac{N(Z^0 \to q\bar{q}g, g \to c\bar{c})}{N(Z^0 \to hadrons)} \tag{2.1}$$

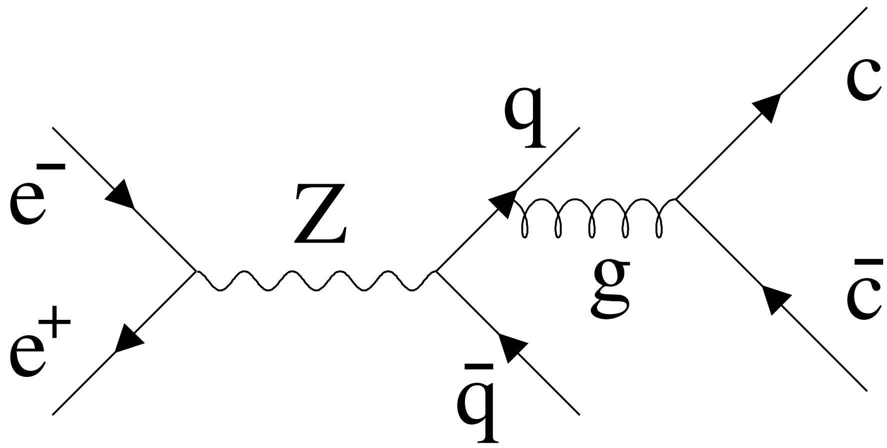

Figure 2.1: Feynman diagram for *gluon splitting* in $c\bar{c}$, at lowest order in α_s.

Measuring the gluon splitting rate is important as a test of perturbative QCD at the Z^0 scale. The process $g \to Q\bar{Q}$ ($Q = c, b$) is one of the main backgrounds in several analyses involving heavy flavoured quarks, since c and b from gluon splitting can be misidentified as primary quarks coming directly from Z^0 decay.

For example, one third of the total experimental error on $R_b \equiv \Gamma_{b\bar{b}}/\Gamma_{hadrons}$ [30] comes from the uncertainty on $g_{Q\bar{Q}}$ (it is the largest single source of error on this observable). The main $Z^0 \to b\bar{b}$ and $Z^0 \to c\bar{c}$ measurements, in fact, are based on a "double tag" method, consisting in dividing the event in two hemispheres and applying a selection to both. The number of events with one or both hemispheres selected is then used to extract R_b and R_c, knowing from Monte Carlo the selection efficiency for b and c quarks, the amount of *uds* contamination and the correlations between hemispheres. The presence of gluon splitting to heavy quarks can lead a *uds* hemisphere to be tagged as c or b, and influences the inter-hemisphere correlations also in c and b events.

Table 2.1 shows the contribution of the gluon splitting uncertainties to the total error on R_b and R_c.

	Error on R_b	**Error on R_c**
$g_{b\bar{b}} = (2.54 \pm 0.51) \times 10^{-3}$	0.000202 (anticorr.)	0.000106 (corr.)
$g_{c\bar{c}} = (2.96 \pm 0.38) \times 10^{-2}$	0.000074 (anticorr.)	0.000774 (anticorr.)
total	0.000654	0.003069

Table 2.1: Contribution of the gluon splitting uncertainties to the total error on R_b and R_c. The label "corr." or "anticorr." indicates if the R_Q measurement is positively or negatively correlated with $g_{Q\bar{Q}}$.

Gluon splitting to heavy quarks is a background also for Higgs searches, since the strongest Higgs couplings are to heavy fermions and the process $g \to Q\bar{Q}$ in $e^+e^- \to q\bar{q}$ events can fake $H \to Q\bar{Q}$. The significance of the Higgs excess in ALEPH at $m_H = 116\ GeV/c^2$ [31, 32] has a total systematic uncertainty of $\pm 0.15\sigma$, of which the gluon splitting contribution is $\pm 0.04\sigma$.

Furthermore, an accurate knowledge of gluon splitting rates is needed at LHC, where a large fraction of heavy quark events will be produced *via* this process.

2.2 Theoretical prediction for $g_{c\bar{c}}$

The theoretical treatment of the production of heavy quarks from a gluon is described in a series of articles [33, 34, 35, 36, 37, 38].

The description of the *gluon splitting* process is explained in the framework of perturbative QCD.

The amount of radiative emission of gluons is usually a divergent quantity in the $m_g \to 0$ limit, but in the present case the c mass (≈ 1.2 GeV) provides a natural infrared "cut-off" to the gluon energy. However, when calculating $g_{c\bar{c}}$ for jet mass scales well above the quark mass, large logarithmic terms arise at all orders in the perturbative expansion, potentially spoiling its convergence. To make reliable predictions, these terms must be organised into an improved perturbation series that "resums" all large terms in the original series. The "resummation" procedure is described in general in Ref. [39].

2.2.1 Leading order

The calculation of the leading-order (LO) differential cross section for the process $Z^0 \to q\bar{q}g\ , g \to Q\bar{Q}$ is made easier by first considering the process

$$\gamma^* \to q\bar{q}g \quad , \quad g \to Q\bar{Q} \tag{2.2}$$

with $q = u, d, s$ and $Q = c, b$, neglecting interference with diagrams where the heavy quarks pair comes from the photon and the light quark pair is produced by gluon splitting (see Sec. 2.2.2). Integrating over the heavy quark momenta, a simple expression is obtained with two factorized parts that correspond to massive gluon emission followed by its decay into a heavy quark pair [34]:

$$\frac{1}{\sigma_0} d\sigma = \frac{\alpha_s^2}{12\pi^2} C_F dx_1 dx_2 \frac{dx_g^2}{x_g^2} \sqrt{1 - x^2/x_g^2} \left(1 + \frac{x^2}{2x_g^2}\right) \mathcal{M}_{prod} \tag{2.3}$$

$$\begin{aligned} \mathcal{M}_{prod} &= \frac{x_1^2 + x_2^2}{(1-x_1)(1-x_2)} + \\ &+ x_g^2 \frac{2(1+x_1+x_2)(1-x_1)(1-x_2) - (2-x_1-x_2)^2}{(1-x_1)^2(1-x_2)^2} + \\ &+ x_g^4 \frac{2}{(1-x_1)(1-x_2)} \end{aligned} \tag{2.4}$$

where $x_g^2 = m_g^2/s$, $x^2 = 4m_Q^2/s$, $x_{1,2}$ are the energy fractions of the light quark and antiquark respectively, and σ_0 is the total cross section for $\gamma^* \to hadrons$. The term $\mathcal{M}_{prod}$ corresponds to the production part, which reduces to the well known emission formula for $m_g \to 0$.

The normalization of the cross section to σ_0 gives independence of the result from the identity of the vector boson, and so it is equally valid for the process $Z^0 \to q\bar{q}g \to q\bar{q}Q\bar{Q}$.

The integration of Eq. 2.3 yields the LO result [34] which, in the limit $x \approx 0$ (i.e. center-of-mass energy much greater than the secondary quark mass, as is the case for c

quarks at the Z^0 peak), becomes [34, 40]

$$g_{Q\bar{Q}} \equiv \frac{\sigma}{\sigma_0} \approx \left(\frac{\alpha_s}{4\pi}\right)^2 C_F \frac{4}{3} \left\{ -\frac{1}{3}\log^3 x^{*2} - \frac{3}{2}\log^2 x^{*2} - \left(\frac{76}{9} - \frac{2}{3}\pi^2\right) \log x^{*2} + 2.359... \right\} \quad (2.5)$$

where $x^* \equiv \frac{1}{2}e^{5/6}x \approx 1.15\ x$.

2.2.2 Interference term

The previous results rely on the assumption that it is possible to separate the processes $Z^0 \to q\bar{q}g \to q\bar{q}Q\bar{Q}$ and $Z^0 \to Q\bar{Q}g \to Q\bar{Q}q\bar{q}$. For this to happen, the interference term between them has to be zero or negligible. Fortunately this is the case.

In the case $q \neq Q$, and assuming that we do not distinguish quarks from antiquarks (and this is the case, since the $g_{c\bar{c}}$ measurements do not determine the charge of the quarks involved), the interference term vanishes by a consequence of Furry's theorem [41], which, when applied to quarks, states that, due to their opposite axial couplings, cancellations occur between "up" and "down" type quarks (i.e. u and d, c and s) coupled to a vector current[1], leaving only the case $q = b$. The result is [42]

$$\frac{\sigma_I}{\sigma_0} = \frac{1}{3}\left(\frac{\alpha_s}{\pi}\right)^2 I_4 \frac{a_b^2}{\Sigma_i(v_i^2 + a_i^2)} \ , \quad (2.6)$$

where $I_4 \approx 0.460$ and v_i, a_i are the vector and axial couplings of quark i, which give $a_b^2/\Sigma_i(v_i^2 + a_i^2) \approx 0.148$. This only provides an effect of order 0.2% of the $g_{Q\bar{Q}}$ rate. In the case $q = Q$ Furry's theorem no longer applies but since the quark is heavy, the contribution is small (only slightly larger than Eq. 2.6) [37].

2.2.3 Resummed calculation

Every time two widely different mass scales m_1, m_2 are present, large logarithmic terms like $[\alpha_s \log^2(m_2/m_1)]^n$ appear to all orders in perturbative expansion, spoiling the reliability of the LO results (intuitively, for every gluon radiated one has to consider, in general, the collinear and the soft gluon limits, each contributing with a logarithm). In the present case, the relevant mass scales of the problem are m_Q, which has the role of an infrared cut-off, and M_Z. The relevant logarithms to be resummed are of the form $\alpha_s^n \log^k(M_Z/m_Q)$, with $k = 2n - 1$, since the $k = 2n$ terms are absent in the heavy quark case [34] [2].

[1] The cancellation would be exact in case of degenerate masses, i.e. $m_u = m_d$ and $m_c = m_s$.

[2] This is a special feature of the heavy quark case, for which there is no logarithm coming from the collinear limit due to the mass of the final state; a demonstration can be found in Ref. [43]

The computation of the sum of this infinite set of logarithms is called "resummation". This is usually done in terms of evolution equations that describe how the quantity of interest changes with the mass scale[3]. Another approach to the resummation problem is to formulate the evolution as a probabilistic chain, which can be simulated numerically using Monte Carlo methods [20, 21, 22], with an appropriate choice of the evolution variable. Monte Carlo algorithms generally take into account only the leading logarithms, but include many important additional effects, such as the energy-momentum conservation, which enters analytical calculations only at Next-to-Next-to-Leading Order (NNLO) in perturbative expansion [44], and the suppression due to competition for phase-space between different types of emission (e.g. between $g \to gg$ and $g \to Q\bar{Q}$)[4].

In Ref. [33] the resummation is done both analytically (following the methods of Ref. [45]) and with the help of the Monte Carlo algorithm HERWIG [21, 22], which simulates every hadronic process as a factorized series of branchings ($q \to qg$, $g \to q\bar{q}$, $g \to gg$), each with an opening angle smaller than the previous. This approach is described shortly in the following.

In HERWIG the evolution variable is

$$Q^2 \approx E^2(1 - \cos\theta_{ij}) \; , \tag{2.7}$$

where $E = E_i + E_j$, and i, j are the produced partons. This approximation becomes exact in the limit of massless partons. It can be immediately seen that ordering in Q^2 corresponds to ordering in opening angle.

The "form factor" $\Delta(Q)$ is defined as the probability that a parton capable of branching at scales up to Q^2 does not produce any resolvable radiation. This can be written, for massless partons, as

$$\Delta(Q) = \exp\left\{ -\int_{Q_c}^{Q} \frac{dk}{k} \int_{z_i(k)}^{1-z_j(k)} dz \; P(z) \frac{\alpha_s}{\pi} \right\} \; , \tag{2.8}$$

where k is the parton energy, z is the energy fraction of the splitting, $P(z)$ is the *splitting function*, corresponding to the partonic probability to radiate, and Q_c and $z_{i,j}$ are infrared cut-offs. Q_c is given by $Q_i + Q_j$.

[3] A review of these methods can be found in Ref. [39].

[4] The physical origin of this suppression is clear, in a time-ordered picture: soft gluons radiated from the primary quark or from the hard gluon prior to the gluon splitting carry away energy, and thus reduce the phase-space available for the $Q\bar{Q}$ pair. An analytical calculation at Next-to-Leading Order would neglect this important effect.

The *two-scales form factor* is defined as

$$\Delta(Q,q) \equiv \frac{\Delta(Q)}{\Delta(q)} = \exp\left\{-\int_q^Q \frac{dk}{k}\int_{z_i(k)}^{1-z_j(k)} dz\ P(z)\frac{\alpha_s}{\pi}\right\} . \tag{2.9}$$

To generate q values with this distribution, a random number r is chosen with uniform distribution in the range $[0,1]$, and solving

$$r = \Delta(Q,q) \tag{2.10}$$

for q. If the Q value obtained from this equation is above Q_c, then a parton is emitted at scale q, otherwise there is no resolvable emission and the algorithm terminates. This can be easily generalized to the case of more than one type of competing branchings, by choosing q values corresponding to each type of branching according to the above procedure, and then using the largest.

The (massless) splitting function for the elementary process $g \to q\bar{q}$ is [33]

$$P_{g\to q\bar{q}}(z) = \frac{1}{2}(z^2+(1-z)^2) , \tag{2.11}$$

giving the form factor

$$\begin{aligned}\Delta(Q) &= \exp\left\{-\int_{2Q_q}^{Q}\frac{dk}{k}\int_0^1 dz\ (z^2+(1-z)^2)\frac{\alpha_s(k)}{2\pi}\right\} \\ &= \exp\left\{-\frac{1}{3\pi}\int_{2Q_q}^{Q}\frac{dk}{k}\alpha_s(k)\right\}\end{aligned} \tag{2.12}$$

which, using Eq. 1.19, becomes

$$\Delta(Q) = \left(\frac{b'+1/\alpha_s(2Q_q)}{b'+1/\alpha_s(Q)}\right)^{\frac{1}{6\pi b}} . \tag{2.13}$$

In the case $g \to Q\bar{Q}$ the heavy quark mass cannot be neglected, and a complete treatment would lead to integrals of the form

$$\int_{x^2}^{a}\frac{dz}{z}\sqrt{1-\frac{x^2}{z}}\left(1+\frac{x^2}{2z}\right)\log^{n-1}z = -\frac{1}{n}\log^n x^{*2} + \mathcal{O}\left(\log^{n-2}x^{*2}\right) \tag{2.14}$$

(for small x); however, exactly the same result is obtained (to Next-to-Leading Logarithmic accuracy) using the massless splitting function (Eq. 2.11) and the effective reduced mass x^*:

$$\int_{x^{*2}}^{a}\frac{dz}{z}\ \log^{n-1}z = -\frac{1}{n}\log^n x^{*2} . \tag{2.15}$$

Therefore by using the effective mass $m_Q^* \equiv \frac{1}{2}e^{5/6}m_Q \approx 1.15\ x$ (which has the physical interpretation of the resolution scale at which the heavy quarks are resolved, see Ref. [37]) it is possible to neglect the heavy quark mass in the decay of the gluon while maintaining the correct Leading and Next-to-Leading logarithms.

Since b and b' in Eq. 2.13 are functions of N_f, the integral in the form factor has to be written as a sum over flavours, yielding

$$\Delta(Q, 2Q_q) = \Delta(Q, m_f)\Delta(m_f, m_{f-1})\ldots\Delta(m_{q+1}, 2Q_q)\ , \tag{2.16}$$

where m_f is the mass of the f-th flavour. The physical interpretation is straightforward: between the first $q \to qg$ emission and the gluon splitting into a $Q\bar{Q}$ pair, several branchings can happen (including the possibility $g(Q_1) \to q\bar{q}$, $q = u, d, s$, followed by $q \to qg(Q_2)$, with $Q_2 < Q_1$ as obvious).

2.2.4 Matching of LO and NLL results

A simple addition of the Leading Order result, which is exact at this order, with the approximate result obtained with an all-order resummation technique like the one described would count twice the Leading Logarithmic term. To avoid this, we have to subtract the sum of the terms they have in common. The terms to subtract are evaluated at the *threshold region*, defined as the regime in which $\log x$ is large but $\alpha_s \log x$ is still small [45].

The comparison with the exact Leading Order result at the threshold also allows a test of the resummation procedure. In Ref. [34], the threshold expansion of the analytical result is

$$g_{Q\bar{Q}} \approx \left(\frac{\alpha_s}{4\pi}\right)^2 C_F \frac{4}{3}\left\{-\frac{1}{3}\log^3 x^{*2} - \frac{3}{2}\log^2 x^{*2} - Y\log x^{*2}\right\} + \mathcal{O}(\alpha_s^3)\ , \tag{2.17}$$

with

$$Y \equiv \frac{1}{27C_A^4}(99C_A^4 + 54C_A^3N_f - 28C_A^2C_FN_f - 32C_A^2N_f^2 + 88C_AC_FN_f^2 - 64C_F^2N_f^2)\ .$$

The comparison between Eq. 2.5 and Eq. 2.17 confirms the correctness of the resummed result at Leading and Next-to-Leading logarithmic order, since the coefficients of the $\alpha_s^2\log^3 x^{*2}$ and $\alpha_s^2\log^2 x^{*2}$ terms are exactly reproduced, while the Next-to-Next-to-Leading term, $\alpha_s^2\log x^{*2}$, has the wrong coefficient Y.

2.2.5 Leading non-perturbative contributions

Ref. [46] considers the non-perturbative contribution coming from the gluon condensate, i.e. the vacuum expectation value of F^2 (short notation for $F^A_{\mu\nu}F^{\mu\nu}_A$, where $F^A_{\mu\nu}$ is defined in Eq. 1.6) [47].

The result is

$$\frac{\langle \alpha_s F^2 \rangle}{N_f^2 - 1} \frac{\alpha_s(m_Q)}{m_Q^4} \left(-\frac{1}{30} C_F + \frac{53}{3780} C_A \right) , \tag{2.18}$$

where $\langle F^2 \rangle$ is the gluon condensate. Adopting the determination $\langle (\alpha_s/\pi) F^2 \rangle \approx 0.012\ \mathrm{GeV}^4$, this non-perturbative contribution is found for c quarks to be about five orders of magnitude smaller than the perturbative result. The scale of the non-perturbative contribution is set by the ratio $\langle \alpha_s F^2 \rangle \frac{\alpha_s(m_c)}{m_c^4} \approx \mathcal{O}\left(10^{-2}\alpha_s(m_c)\right)$, a value which is already small compared with the perturbative contribution. Its coefficient turns out to be very small too, due to an accidental cancellation between the C_F and C_A terms in Eq. 2.18.

2.2.6 Numerical results

The most recent determination [38], at NLL (Next-to-Leading-Logarithmic) order, yields:

$$g_{c\bar{c}} = 2.3 \times 10^{-2} \quad (m_c = 1.2\ \mathrm{GeV}/c^2, \alpha_s = 0.120) \tag{2.19}$$

$$g_{c\bar{c}} = 1.7 \times 10^{-2} \quad (m_c = 1.5\ \mathrm{GeV}/c^2, \alpha_s = 0.120) \tag{2.20}$$

$$g_{c\bar{c}} = 2.0 \times 10^{-2} \quad (m_c = 1.2\ \mathrm{GeV}/c^2, \alpha_s = 0.118) \tag{2.21}$$

The behavior of the predicted value of $g_{c\bar{c}}$ as a function of $\sqrt{s}$ is shown in Fig. 2.2, taken from Ref. [34]. Also shown is the LO result, from which the importance of completing the result with the matched resummation is evident.

The result depends on the heavy quark masses and on the QCD scale constant $\Lambda^{(5)}$ (see Sec. 1.3.3). A rough idea of the influence of these effects can be obtained from the variations shown in Fig. 2.2. The variation with $\Lambda^{(5)}$ gives some indication of the size of the uncertainty resulting from the neglected terms in the perturbation series, since the first neglected term should cancel this dependence [34]. A variation of $\Lambda^{(5)}$ by a factor of two is equivalent to varying α_s by 10%, as can be seen from Eq. 1.23. The uncertainty due to neglected terms in the perturbation series is estimated, in Ref. [34], to be around 30% of the result.

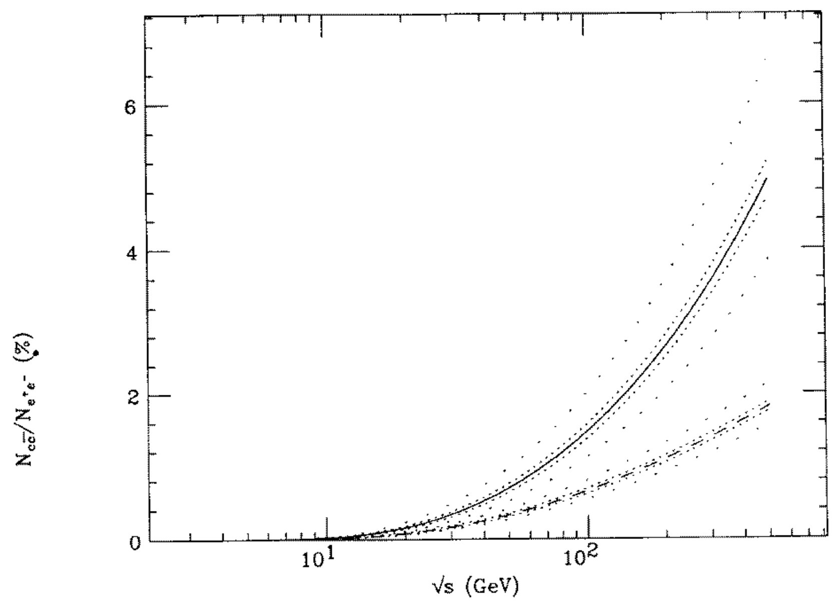

Figure 2.2: $g_{c\bar{c}}$ ratio as a function of the center of mass energy $\sqrt{s}$ for e^+e^- processes, according to the leading-order calculation (dashed) and the complete calculation of Ref. [34] (solid). Also shown are the results of varying the quark mass by 5% (fine-dotted) and $\Lambda^{(5)}$ by a factor of 2 (dotted).

2.3 Previous measurements of the gluon splitting rate into $c\bar{c}$

A typical experimental signature for $g \to c\bar{c}$ are three jets events, with a jet clustering optimized so that c and $\bar{c}$ products are mainly in the same jet (which tends to be the broadest and the softest).

Three methods have been used to measure $g_{c\bar{c}}$:

- D^* reconstruction;
- looking for leptons in three-jet events;
- event shape variables.

2.3.1 Methods based on D^* reconstruction

OPAL [48] and ALEPH [49] reconstruct $D^{*\pm}$ mesons looking for the decay $D^{*\pm} \to D^0\pi^\pm$ followed by $D^0 \to K^\mp\pi^\pm$. The smallness of the phase space available to the background ($M(D^*) - M(D^0) \approx M(\pi)$) compensates the limited statistics available for this channel.

After the selection of a sample of $D^{*\pm}$ candidates OPAL extracts the $g_{c\bar{c}}$ value from a fit to the meson energy spectrum. Signal events are mainly contributing to the low momentum side of the distribution (Fig. 2.3).

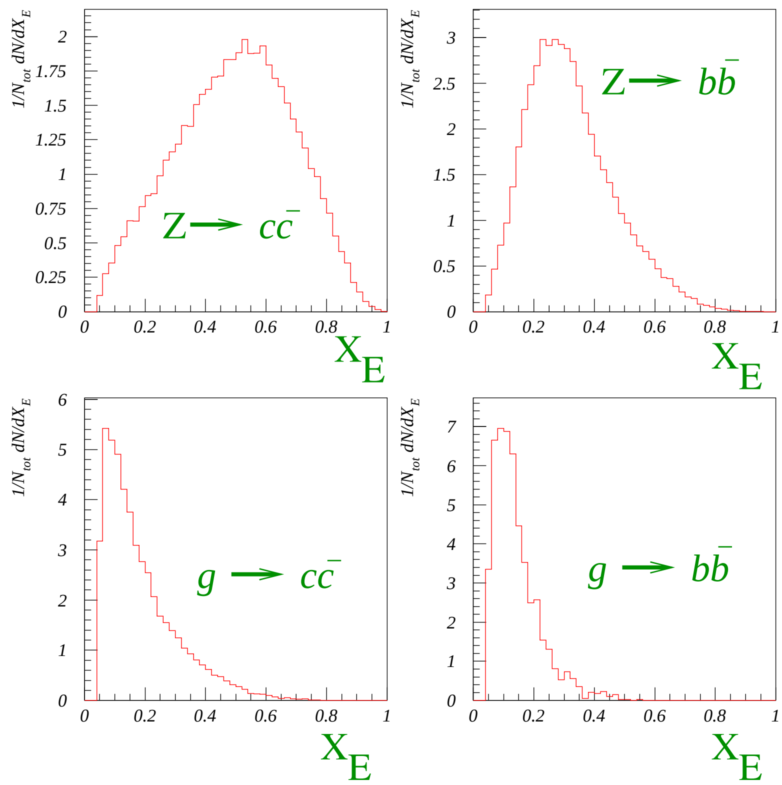

Figure 2.3: Energy spectra of $D^{*\pm}$ coming from different processes.

ALEPH divides the event in two hemispheres separated by a plane orthogonal to the thrust axis. The $D^{*\pm}$ mesons from gluon splitting are preferentially found in the hemisphere with the larger invariant mass, while the mesons from direct $c\bar{c}$ production are found with equal probability in both hemispheres. The $g_{c\bar{c}}$ value is extracted from a fit to the difference in mass between the hemispheres (Fig. 2.4).

The results for the two analyses are:

$$\begin{array}{llcl} \text{OPAL} & g_{c\bar{c}} & = & (4.08 \pm 1.22(stat.) \pm 0.79(syst.)) \times 10^{-2} \\ \text{ALEPH} & g_{c\bar{c}} & = & (3.23 \pm 0.48(stat.) \pm 0.53(syst.)) \times 10^{-2} \end{array}$$

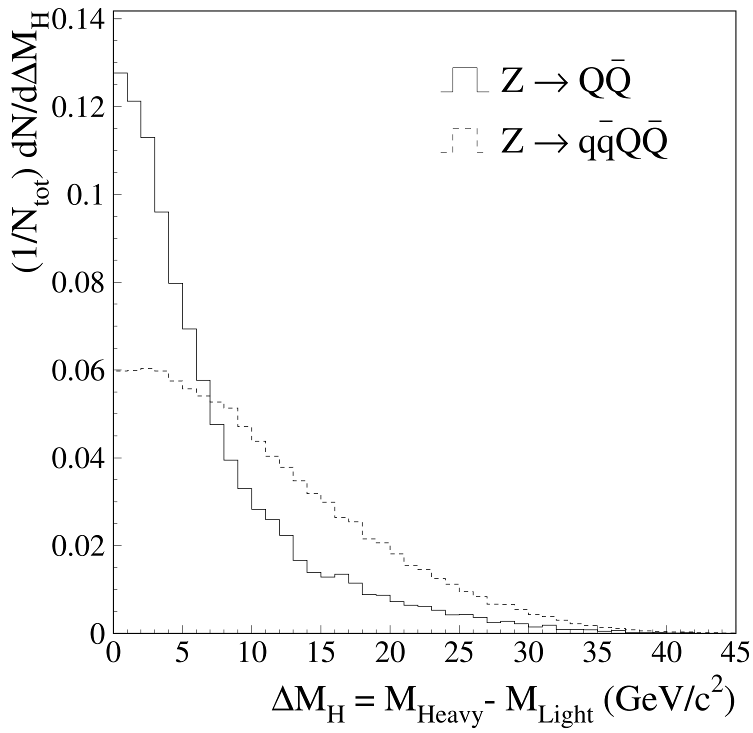

Figure 2.4: Mass difference between hemispheres in events with D^* in ALEPH, for gluon splitting and primary heavy flavour production.

2.3.2 Methods based on leptons in three-jet events

OPAL [48] and L3 [50] identify leptons from charm decays and assume the lowest-energetic jet to be the "gluon jet".

Leptons from $g \to c\bar{c} \to Xl\nu$ have a softer spectrum than leptons coming from primary charm quarks, so momentum is used in the selection. The largest background comes from decays of primary b and c hadrons. Further signal/background discrimination is provided by the invariant mass of the "gluon jet" (which in gluon splitting events contains the remnants of two heavy quarks).

The main systematic errors which are characteristic of this method are the uncertainty on the semileptonic branching ratios of heavy quarks and the uncertainty on the rejection of the fake leptons, due to the soft spectrum of the leptons from gluon splitting into charm quarks. This mainly concerns the muon sample, which suffers from the contamination from misidentified π's and K's and from muons produced in $\pi, K \to \mu\nu$ decays.

The results for the two analyses, separately for electron and muons, are:

$$\begin{array}{llcl} \text{OPAL } (e) & g_{c\bar{c}} & = & (3.03 \pm 0.28(stat.) \pm 0.41(syst.)) \times 10^{-2} \\ \text{OPAL } (\mu) & g_{c\bar{c}} & = & (3.53 \pm 0.37(stat.) \pm 0.79(syst.)) \times 10^{-2} \\ \text{L3 } (e) & g_{c\bar{c}} & = & (3.14 \pm 1.14(stat.) \pm 0.85(syst.)) \times 10^{-2} \\ \text{L3 } (\mu) & g_{c\bar{c}} & = & (3.06 \pm 1.76(stat.) \pm 0.83(syst.)) \times 10^{-2} \end{array}$$

2.3.3 Measurement based on event shape variables

L3 [50] performs an analysis using a neural network (see Chapter 5) having as inputs several global event shape variables, such as three different Fox-Wolfram moments [51] and the mass difference between the heaviest and the other two jets, in three-jet events enriched in heavy quarks.

The weakness of the method lies in the difficulty to obtain a high purity, even with a tight cut on the neural network output; nevertheless, this is largely compensated by the high statistics since all the hadronic decays of the c quarks are used.

The main systematic uncertainties are related to the incorrect modeling of the input distributions, which has an influence during the training of the neural network. The result is:

$$\text{L3} \quad g_{c\bar{c}} \quad = \quad (2.27 \pm 0.30(stat.) \pm 0.59(syst.)) \times 10^{-2}$$

2.3.4 Current world average

The $g_{c\bar{c}}$ and $g_{b\bar{b}}$ measurements are combined taking into account the correlations between different measurements of the same quantity, and the fact that $g_{c\bar{c}}$ is an input to $g_{b\bar{b}}$ and *vice-versa*. The method will be described in Sec. 8.1.

This procedure yields [52]

$$g_{c\bar{c}} = (2.96 \pm 0.38) \times 10^{-2} \,, \tag{2.22}$$

$$g_{b\bar{b}} = (2.54 \pm 0.51) \times 10^{-3} \,. \tag{2.23}$$

Chapter 3

Experimental Setup

3.1 LEP

The **L**arge **E**lectron **P**ositron collider (LEP) [53] was an e^+e^- circular synchrotron, with a circumference of 27 km, located near Geneva, at the French-Swiss border. Built for precision studies of the Standard Model, LEP started the physics runs in 1989; in the first phase, denoted LEP I (1989-1995), it was operated at and near the Z^0 peak, which corresponds to a beam energy of 45.6 GeV. In a second phase, LEP II (1995-2000), the beam energy was increased until 104.5 GeV ($\sqrt{s}$ = 209 GeV). The LEP luminosity was of the order of $10^{31}\mathrm{cm}^{-2}\mathrm{s}^{-1}$.

The electron beam was produced in two steps. Primary electrons were extracted from a metal surface (electron gun), then injected into an electron cyclotron resonance (ECR), where the electron beam was subsequently amplified by stripping off the electron shell of lead atoms. Electrons were first stored and further accelerated in the Electron Positron Accumulator (EPA) ring. Positrons were produced by colliding an electron beam with a heavy metal target, then also stored and accelerated in the EPA. In order to reach the desired energy, the electrons and the positrons were accelerated through a set of four accelerators until finally reaching LEP.

The first stage of acceleration happened in a linear accelerator (LINAC) where the final energy of electrons was 500 MeV. Then all particles passed through the Proton Synchrotron (PS), which had a diameter of 200 m. The beams were then injected into the larger Super Proton Synchrotron (SPS), an underground circular accelerator, 6 km in circumference. This was the final link in the chain of accelerators and operated as an electron/positron injector for LEP.

At four equidistant points around the LEP ring, the bunches of particles were focused,

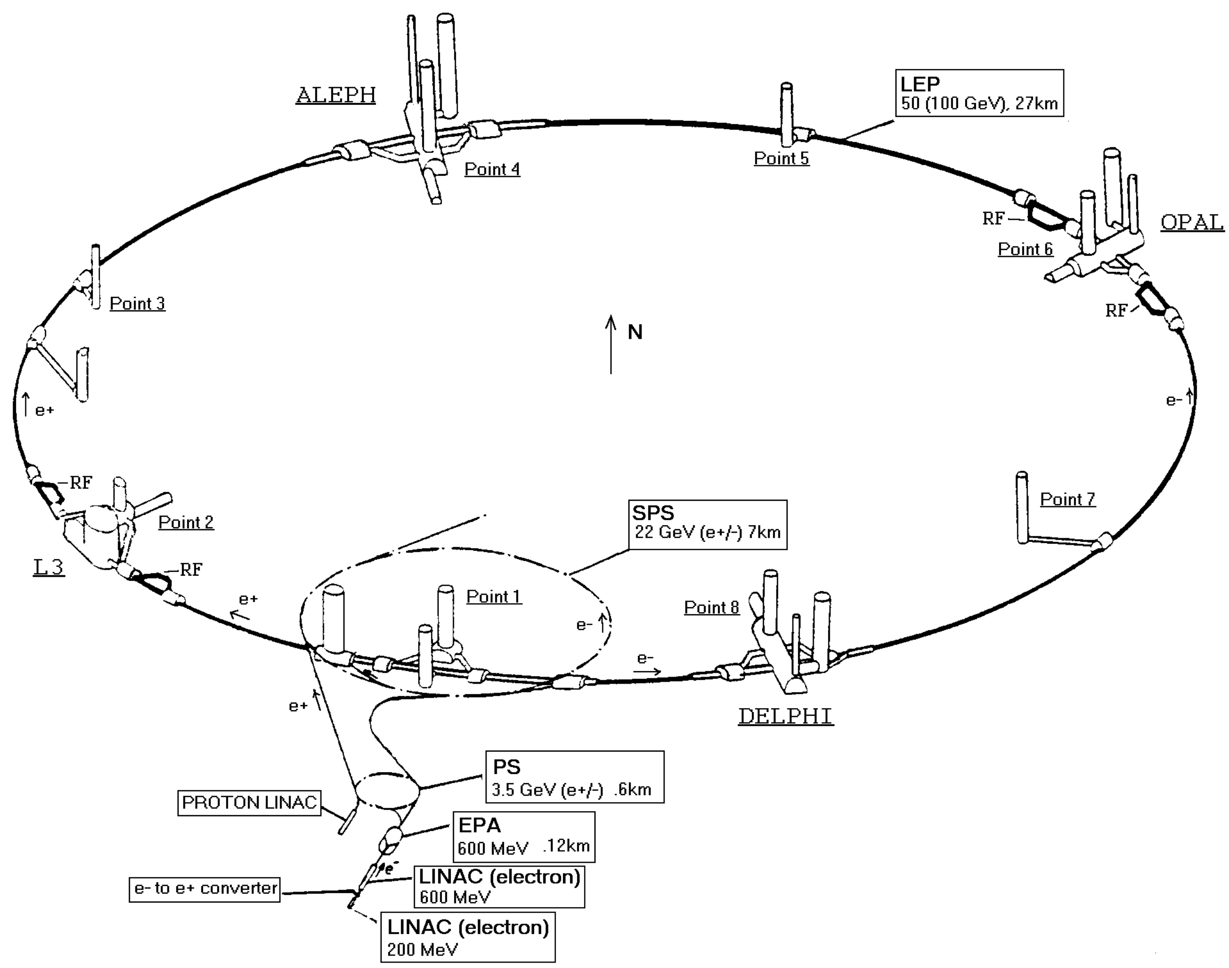

Figure 3.1: Sketch of the LEP ring.

using superconducting quadrupole magnets, down to a transversal area of 10×250 μm and made to collide inside the four LEP detectors: ALEPH, DELPHI, L3 and OPAL. At the Z^0 energy LEP worked with 12 bunches, each containing around 10^{11} particles. On average, one out of 10^8 bunch crossings produced the desired head-on e^+e^- collision. For this reason, the bunches were made to circulate for hours, each bunch traveling round the ring in 89 μs.

The LEP beam energy was measured using resonant depolarization [54] with an accuracy better than 1.1 MeV for $E = 45.6$ GeV.

3.2 ALEPH Detector

The ALEPH (**A**pparatus for **LE**p **PH**ysics) detector [55] has been designed to measure the events produced by the e^+e^- collisions in LEP over almost all the solid angle ("4π" detector), obtaining as much information as possible. Z^0 bosons can decay hadronically producing an average of 21 charged tracks, which requires many tracking measurements to be made to enable reconstruction of all the tracks. The interesting event rate at the Z^0 peak was around 1 Hz. The ALEPH detector was therefore designed to be hermetic, fast and granular in order to collect as much information as possible for each of these tracks.

The detector, shown in Fig. 3.2, had a cylindrical structure around the beam pipe, with the interaction point in the center of the detector. The tracking system and the electromagnetic calorimeter were immersed in a solenoidal magnetic field of 1.5 Tesla produced by a superconducting coil. The iron return yoke was divided into layers and instrumented with streamer tubes and served as a hadron calorimeter. Outside the hadron calorimeter, two double layers of streamer chambers were used to detect the muons that penetrated the iron. Luminosity monitors at very low angle completed the scheme.

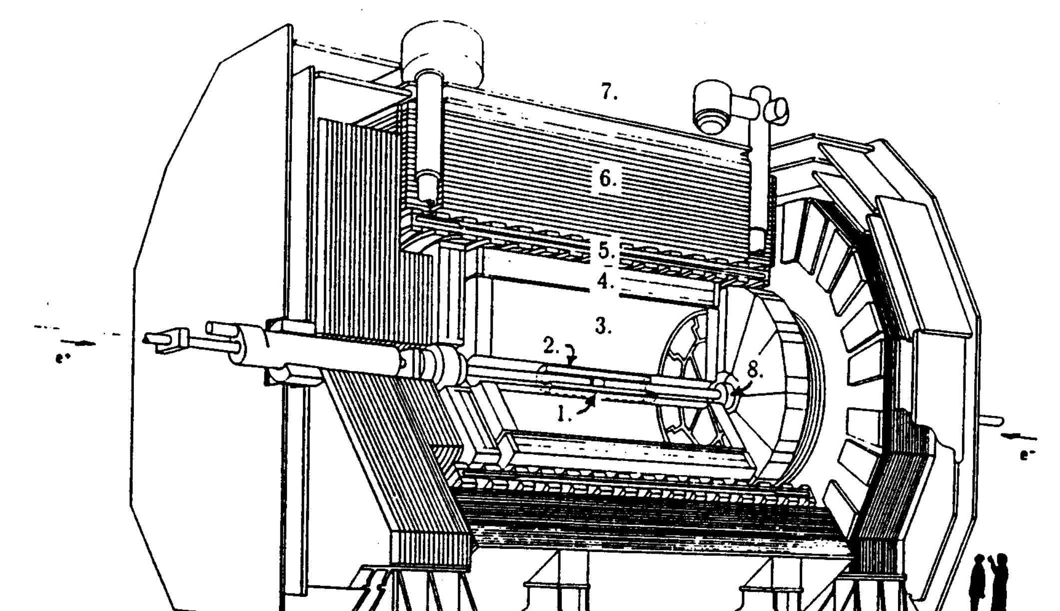

Figure 3.2: The ALEPH detector: 1. Vertex detector, 2. Inner tracking chamber, 3. Time projection chamber, 4. Electromagnetic calorimeter, 5. Superconducting magnet coil, 6. Hadron calorimeter, 7. Muon chambers, 8. Luminosity monitors.

A detailed description of the ALEPH detector can be found in Ref. [55], while its performance is reviewed in Ref. [56]. Here, a brief description of the detector components and of the particle reconstruction is presented.

3.2.1 Silicon vertex detector

The silicon vertex detector (VDET) provided high precision measurements of the trajectories of the charged particles close to the interaction point. It consisted of two concentric layers of silicon strip detectors, with an average radius of $r_1 \approx 6.3$ cm for the inner layer and $r_2 \approx 10.9$ cm for the outer layer. The inner layer had 9 faces, each of two modules, one module consisting of two wafers of 51.2 mm $\times$ 51.2 mm; the outer layer had 15 faces, giving a total of 96 wafers for the whole VDET[1].

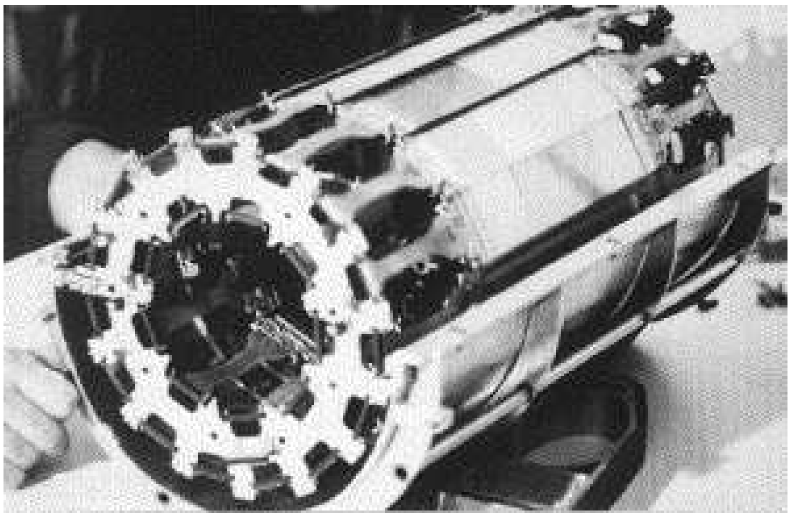

Figure 3.3: Overall view of VDET.

The wafer (Fig. 3.4) had readout strips on both sides. On one side, the strips were perpendicular to the beam direction, measuring the z coordinate; on the other side, the strips were parallel to the beam direction and measured the azimuthal angle ϕ. The physical pitch on both sides was 25 μm.

[1] This description refers to the vertex detector used in the 1991-1995 period [57, 58]; it was replaced in the late summer of 1995 by VDET II. The data analyzed in this dissertation were taken with the old detector.

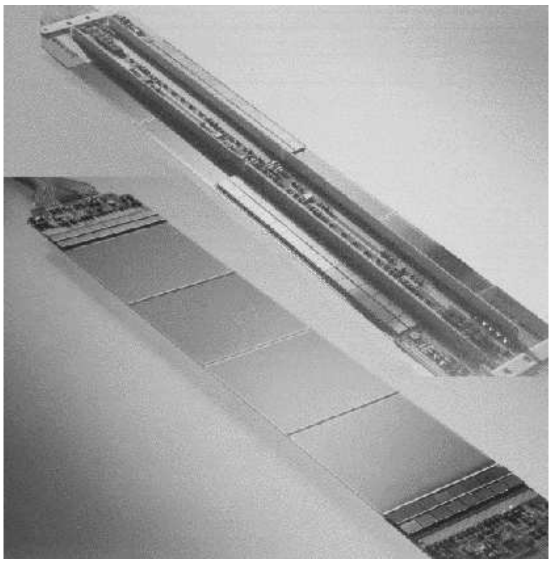

Figure 3.4: View of a face of the VDET.

The VDET hits were reconstructed offline, by averaging the charge-weighted positions of adjacent strips that had at least three times the mean noise charge.Those hits were used to provide additional precision for tracks already reconstructed in the outer tracking, and were associated to tracks by minimizing the χ^2 of a track refit including candidate VDET hits. Monte Carlo studies show that the VDET hit association is correct for 98% (90%) of the hadronic Z^0 decay tracks with hits in both (one) layers.

The relative positions of the silicon wafers are determined from the data with no reference to the outer tracking. Tracks which pass through the $\sim 5\%$ active overlap area between wafers adjacent in ϕ constrain their relative position. Linking the wafers around the full azimuth via their overlap constrains their average radii. Tracks from $Z^0 \to \mu^+\mu^-$ events constrain the relative position of wafers in different layers and on opposite sides of the detector. The resulting alignment contributes negligibly to the hit errors. The point resolution, including all intrinsic and alignment effects, is about 12 μm; the impact parameter resolution is 23 μm in r-ϕ projection and 28 μm in r-z projection.

3.2.2 Inner tracking chamber

The inner tracking chamber (ITC) was a cylindrical multiwire drift chamber. It provided up to 8 accurate r-ϕ points for tracking in the radial region between 160 mm and 260 mm.

The active volume of the ITC was a cylinder of 2 m of length and 570 mm diameter; the outer surface was defined by a carbon fiber tube coated on both surfaces with thin (25 μm) aluminum foil, while the inner surface was defined (after 1991) by a carbon fiber tube, 600 μm thick, with a 50 μm thick aluminum foil on the larger radius surface.

The volume bounded by the outer tube, the inner tube and the electrical end-flanges was filled with a combination of 80% Argon + 20% Carbon Dioxide at atmospheric pressure; a small fraction of ethyl alcohol was added, to inhibit the formation of the polymers and the deposition of dirt on the wires.

The wires ran parallel to the beam direction; 960 sense wires were strung in 8 concentric layers. Each sense wire was surrounded by 6 field wires, forming a hexagonal drift cell (Fig. 3.5), with the sense wire in the center of the cell. Four of these field wires were shared by the neighboring cells in the same layer. To resolve the left-right ambiguity in the track fitting, the drift cells are 'close-packed': cells in contiguous layers are offset by half a cell width.

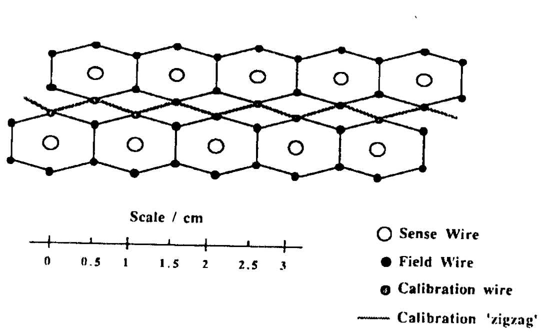

Figure 3.5: The ITC drift cell.

The sense wires were operated at a positive potential, the field wires were held at earth potential.

The r-ϕ coordinate was obtained by measuring the drift time of the electrons produced when a charged particle traversed the gas. The relation between the drift time and the drift distance is extracted from the data because it depends on the gas composition and is strongly influenced by the magnetic field.

The z coordinate was determined by measuring the difference in arrival time of the signal at each end of the wires; it was used only to implement the three-dimensional first-level track trigger (Sec. 3.4) and not in the standard tracking.

The r-ϕ resolution varied with the position in the cell and, to a lesser extent, with the cell size. For a typical sample a mean value of 150 μm was obtained, averaging over all the tracks. The z resolution was of the order of few centimeters.

The position of the drift chamber relative to the TPC was determined with data. Initial values of the alignment constants were determined with the help of cosmic ray tracks and survey data. The three translational alignment parameters and the three Euler angles relative to the TPC were then measured with tracks from the processes $Z^0 \rightarrow \mu^+\mu^-$ and $Z^0 \rightarrow q\bar{q}$, by minimizing the residuals between the measured hits and the expected hit positions of tracks extrapolated from the TPC into the drift chamber.

3.2.3 Time projection chamber

The TPC (Fig. 3.6) was the ALEPH central detector for charged particles. The chamber had a cylindrical structure with the axis parallel to the magnetic field. The volume defined by the outer field cage (with a diameter of 3.6 m) and the inner field cage (with a diameter of 60 cm), both of 4.4 m lenght, were divided into two half-detectors by a central membrane perpendicular to the cylinder axis. The cylinder was closed at the two ends with planar wire chambers and the whole volume was filled with a 91% Argon + 9% methane gas mixture.

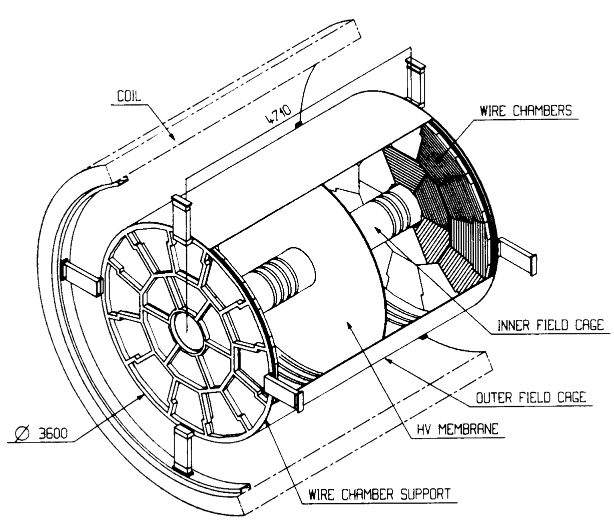

Figure 3.6: TPC structure. All measures are in mm.

A charged particle traversing the gas volume creates pairs of electrons and positive ions along its path. The electrons, under the influence of the electrical field created between the central membrane and the wire chambers, drifted toward one end-plate where they were collected. Their arrival position and time were measured by the wire chambers.

Hence, the trajectory of a charged particle in the TPC (a helix) was projected onto the end-plate plane as an arc of a circle, keeping also the time information.

The central membrane (25 μm Mylar, coated on both sides with a conducting graphite paint) was held at a negative high voltage (-27 kV, typically) and the wire chambers were at a potential near ground. The electrodes of the field cages were held at potentials so that the drift field in the chamber volume was constant (115 V/cm) and parallel to the cylinder axis.

The TPC was operated at a gas pressure of 7-8 mbar above the atmospheric pressure in the experimental zone; the gas temperature was maintained at 21 ± 0.5 °C. The gas quality (gas mixture ratio, contamination by electronegative impurities) influenced strongly the performance of the TPC, therefore the gas was premixed into large buffer vessels to obtain absolute variations of the mixing ratio less than 0.03% and was systematically checked against contamination prior to each buffer refill.

For every track traversing the inner and outer field cages, the TPC measured up to 21 three-dimensional points which are used to determine the track coordinates. Apart from the track parameters, the ionization of every charged track was also sampled by the TPC sense wires and readout pads, with a spacing of 4 mm. The dE/dx information (see Sec. 4.4) is used to separate particle species, according to the specific energy loss, complementing the performance of the electromagnetic calorimeter.

The quality of the track reconstruction in the TPC (whose details will be discussed in Sec. 4.2) depends critically on precise knowledge of systematic distortions of the tracks during the drift of their ionization towards the end-plates. Distortions due to inhomogeneities of the magnetic and electric fields are determined from a magnetic field map, as measured in 1987 [55], and from the straightness of reconstructed laser tracks in the TPC. A detailed description of the methods used to calibrate drift-field distortions with the laser system can be found in Reference [59].

The z-coordinate was obtained from the drift time and the drift velocity. The drift velocity can be set by requiring that the tracks from hadronic Z^0 events in the two halves of the TPC come from the same origin. The drift velocity change was determined and updated on a run-by-run basis in a precursor to the full event reconstruction. The method was regularly monitored by comparing the track polar angle θ reconstructed in the TPC to that observed in the vertex detector, and also by comparing measurements from the laser system.

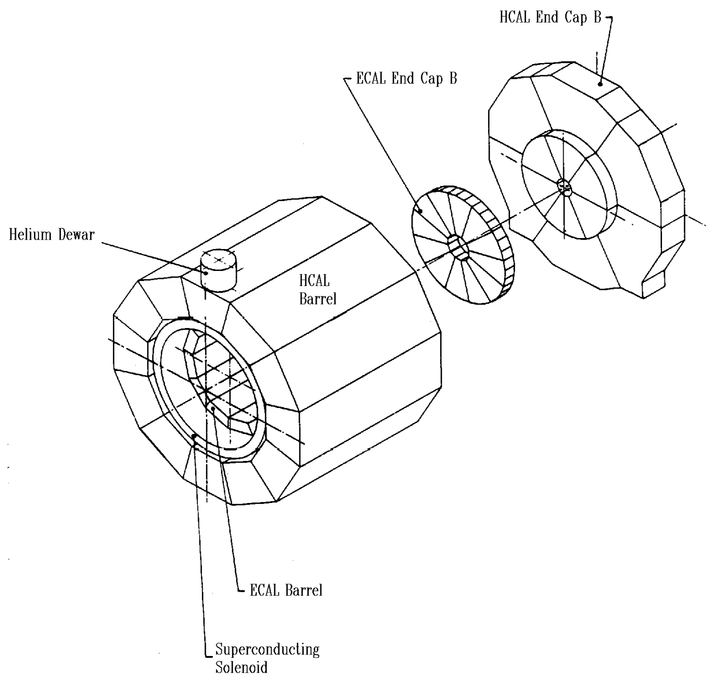

Figure 3.7: ECAL and HCAL structure.

The ϕ-coordinate was computed by interpolating the signals induced on the cathode pads; the r-coordinate was given by the radial position of the pads involved in the measurement.

The z-resolution depends on the polar angle θ of the track, while the azimuthal resolution $\sigma_{r\phi}$ depends on the drift lenght and on the pad crossing angle. For tracks with 90° polar angle a resolution of 740 μm in z and 173 μm in r-ϕ was achieved, while for $\sim 20°$ the uncertainties were almost doubled.

3.2.4 Electromagnetic calorimeter

The electromagnetic calorimeter (ECAL) was formed of a barrel surrounding the TPC, closed at each end by an end-cap (see Fig. 3.7). The calorimeter covered 3.9π sr, with cracks representing 2% of the barrel and 6% of the end-cap surface. The nominal thickness of the calorimeter was 22 radiation lenghts (X_0).

The barrel and every end-cap were divided into modules, each module subtending 30° in azimuthal angle. To avoid overlapping of crack regions, the end-cap modules were rotated by 15° with respect to the barrel modules, while the whole ECAL was rotated by $-1.875°$ with respect to the hadron calorimeter.

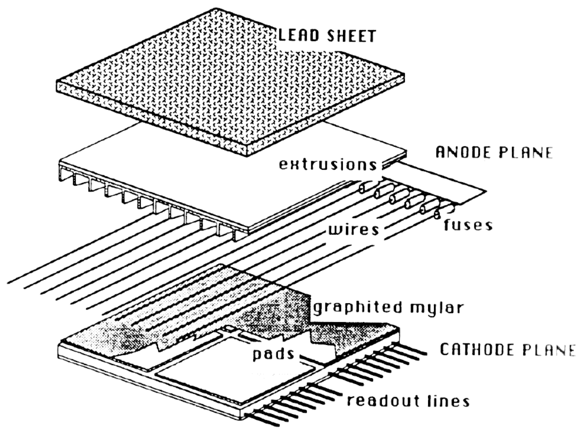

Figure 3.8: A typical layer of ECAL.

Each of the 36 modules consisted of 45 lead/proportional wire-chambers in a sandwich structure (Fig. 3.8). The wire chambers were made from Al extrusions. The wires (gold-plated tungsten, 25 μm in diameter) lied in the channels of the extrusions; the chamber was filled with a gas mixture of Xenon (80%) and CO_2 (20%) at 60 mbar above the atmospheric pressure. The open side of the extrusions was separated by a highly resistive graphite-coated Mylar from the cathode plane; the cathode plane contained small Cu pads of dimension around 30 mm $\times$ 30 mm, variable in θ angle to preserve the projective geometry.

An electromagnetic shower developed in the lead sheets produced ionization in the wire chambers which worked in the proportional regime. The signal was read directly for every wire plane, independently for each module and capacitively via the extrusions open face with cathode pads. The pads from consecutive layers were connected to form towers pointing to the interaction region. Each tower was read out in three segments in depth ("storeys"), corresponding to the first "stack" ($\approx 4X_0 = 10$ layers of 2 mm lead sampling), the second stack ($\approx 9X_0 = 23$ layers of 2 mm lead sampling) and the third stack ($\approx 9X_0 = 12$ layers of 4 mm lead sampling). There were 73728 towers in total, with a $\Delta\phi \times \Delta\theta$ segmentation of $0.94° \times 0.93° \sin\theta$ for the barrel part and $0.9° \times 0.9°$ for the end-caps.

The variation of the gain of a module due to changes in gas pressure, temperature and composition were monitored using, for every module, a small single-wire proportional chamber associated to a ^{55}Fe source, emitting 6 KeV X-rays. The variation of the peak of the spectrum followed the variation of the module response. After correcting for the measured gain variation, the amplitude of the variations was reduced from $2\% - 3\%$ over a year to better than 0.3%.

The absolute calibration was performed with electrons in the energy range 1 to 45 GeV. They were obtained from the reactions: $e^+e^- \rightarrow e^+e^-e^+e^-$ for the 1 to 10 GeV range, $Z \rightarrow \tau^+\tau^-$ with $\tau \rightarrow e\nu\bar{\nu}$ for 10 to 30 GeV, and Bhabha events[2] for 45 GeV. All individual storeys that had a signal corresponding to an energy greater than 30 MeV and had in common at least a storey edge or corner were gathered over a single "cluster". The cluster energy was corrected for:

- Saturation effects.
- Leakage effects (shower not fully contained in ECAL). The value of the correction was of the order of 0.8% in the barrel part and 1.5% in the end-cap, for 45 GeV electrons.
- Ionization losses before entering the calorimeter, in the case of charged particles.
- Energy losses due to the storey threshold.
- Non-linearity of the calorimeter response to electrons. The correction, obtained from test-beam results, can be parameterized as $E_{corr} = E(1 + 0.00078E/GeV)$.

The accuracy of the absolute calibration obtained after all the corrections was better than 0.3% at 45 GeV and 1.5% at lower energies.

The energy resolution, obtained by comparing the ECAL measured energy to the track momentum or beam energy, can be parameterized as

$$\frac{\sigma(E)}{E} = \frac{0.18}{\sqrt{E/GeV}} + 0.009 \ . \tag{3.1}$$

In the overlap regions the resolution was degraded by about 30% by the additional dead material present.

3.2.5 Hadron calorimeter and muon chambers

The hadron calorimeter (HCAL) was a Fe-streamer tube structure; the iron part served as yoke for the magnetic flux return and was the passive absorber for HCAL. Similar to ECAL, HCAL was divided into a barrel part and two end-caps. The barrel part consisted

[2] $e^+e^- \rightarrow e^+e^-$.

of 12 modules, each one split in two symmetrical parts; each end-cap was structured in six modules. Every module was a sandwich of 23 layers of plastic streamer tubes separated by 5 cm thick iron slabs; the first detector layer was positioned in front of the first slab and the next 22 layers were inserted in the gaps between subsequent slabs. The last iron slab was 10 cm thick; the total 120 cm iron corresponded to 7.16 interaction lenghts at $90°$.

The streamer tubes consisted of plastic (PVC) comb profiles, with eight cells each, painted with graphite on the internal surface. On the upper side, copper pads were drawn for a capacitive readout; these pads were summed up in 4788 projective towers pointing to the interaction region, with a typical tower coverage of $3.7° \times 3.7°$ corresponding on average to 14 ECAL towers. On the other side of the comb, 4 mm wide aluminum strips were glued on a plastic support along the tube and gave a standard logic signal providing a two-dimensional view of the development of hadronic showers. This was used in the identification of muons, described in Sec. 4.7.3, and, together with the towers, in the energy-flow algorithm (Sec. 4.3).

The tubes were filled with a mixture of Ar (22.5%), CO_2 (47.5%) and Isobutane (30.0%); a gas monitoring system was used to measure the time dependence of the calorimeter calibration with a precision of about 0.4%; variations of up to 10% due to changes in pressure and temperature have been observed over a year.

Two double layers of streamer tubes, both in the barrel and in the end-caps were added outside the magnet; these "muon chambers" were used together with the digital information given by the strips of the HCAL to detect particles leaving the detector (mainly muons). Each layer of tubes had on one side strips parallel to the wires (x-strips) and on the other side strips orthogonal to the wire (y-strips). Muon chambers were important in muon identification in jets in case of hadronic Z^0 decays, much more than for $Z^0 \to \mu^+\mu^-$ events, which were easily recognized with HCAL alone.

The calibration of HCAL was done using muons of 45 GeV from $Z^0 \to \mu^+\mu^-$ decays; for module intercalibration $q\bar{q}$ events were used.

The energy reconstruction for HCAL was done in a similar way to ECAL, building clusters of energy. For pions at normal incidence, the energy resolution of HCAL was

$$\frac{\sigma(E)}{E} = \frac{0.85}{\sqrt{E/GeV}} \ . \tag{3.2}$$

3.3 Luminosity monitors

The luminosity was measured using small-angle Bhabha events, for which the cross-section is well known, into a precisely defined fiducial region.

Since 1992 the luminosity detectors have been two tungsten/silicon calorimeters covering the 24-58 mrad polar angular interval. They consisted of twelve-layered sandwiches of tungsten and silicon wafers. Each silicon layer was read out on 512 pads, corresponding to 15 radial pad-rows of 5.225 mm width, and 11.25° segmentation in azimuth; successive layers were rotated by one third of this angle, so that the detector had no azimuthal crack.

The energy resolution for electrons was

$$\frac{\sigma(E)}{E} = \frac{0.33}{\sqrt{E/GeV}} \; . \tag{3.3}$$

The integrated luminosity is given by N_{Bhabha}/σ_{corr}, where N_{Bhabha} is the number of events passing the luminosity selection cuts, after subtraction of the background (essentially off-momentum beam particles), and σ_{corr} is the cross-section corrected to take into account the t-channel two (or three) hard-photon background (a +0.015% correction). The experimental precision in the 1992 luminosity measurement is estimated to be 0.09%, shared between several sources including thermal expansion of the silicon-detector support ring, uncertainty in the value of the z separation of the calorimeters, and the fidelity of the Monte Carlo shower parameterization.

3.4 The trigger system

The ALEPH trigger system has been designed taking into account the time interval between two consecutive beam crossings (11 μs) and the time needed to read out data, determined by the drift time of the ionization electrons in the TPC. It was organized in three levels, the first two implemented *via* hardware in order to give a fast response, and the third *via* software.

The first level trigger was based on the use of four approaches to derive trigger signals:

1. Energy deposits in ECAL (*Total-energy trigger*): at least $\sim$ 6 GeV in the barrel, $\sim$ 3 GeV in either end-cap, or $\sim$ 1.5 GeV in both end-caps.

2. Track segments in ITC in coincidence with an energy deposit in the ECAL module intersected by the extrapolation of the track (*Electron-track trigger*): at least 200

MeV, which corresponds to less than 50% of the energy deposit of a muon in ECAL.

3. Track segments in ITC in coincidence with hits in a HCAL module, so requiring a sizeable penetration depth (*Muon-track trigger*). This trigger was sensitive to muons and, with lower efficiency, to hadrons.

4. Two track segments back-to-back in ITC (*Back-to-back trigger*).

The first level trigger was able to yield a response in 5 μs, with a 15 Hz frequency. A positive response started the signal digitization and kept the TPC read-out system operative for the whole drift time (≈ 45 μs).

The second level trigger was analogous to the first one, but with the ITC track segments replaced by those from TPC. If no charged track was detected in the TPC, the data acquisition was stopped. The time needed for a second level trigger response was determined by the drift time of the ionization electrons in the TPC; the response was delivered within ≈ 50 μs after the beam crossing, and its frequency was 10 Hz. A positive response started the read-out of the whole detector.

The third level trigger made use of the informations from every subdetector, and its aim was to separate e^+e^- interactions from the backgrounds (cosmic rays, hardware noise, beam related background) and allow them to be recorded. It started an event reconstruction, stopping the reconstruction process as soon as the collected informations were sufficient to label the event as e^+e^- or background.

The system relied on multiple triggers being delivered for each physics channel. The simplicity of the trigger logic and the redundancy allowed trigger efficiencies close to 100% to be obtained, and provides cross-checks for verifying the efficiency of the individual triggers.

Hadronic Z^0 decays were collected using the Total-energy and Muon-track triggers, whose combination had an efficiency greater than 99.99%, with an uncertainty of less than 0.01%, determined by comparing the rates for one or both of the triggers firing.

Leptonic events have a lower multiplicity than hadronic events, and so require larger redundancy. For $Z^0 \to \mu^+\mu^-$ events three triggers were used: Muon-Track, Electron-track and Back-to-back, whose combined efficiency is very near to 100%. The same triggers were used to select $Z^0 \to \tau^+\tau^-$ events, again achieving close to 100% efficiency. Bhabha events, however, were only triggered by the Total-energy trigger with 100% efficiency, since they deposited almost all their energy in the electromagnetic calorimeter. For each of the lepton triggers the efficiencies quoted above are for events in the angular range $|\cos\theta| < 0.9$. The knowledge of the uncertainty on the trigger inefficiency for leptonic events is limited by statistics to 0.05%.

The trigger for Bhabha events at low angle used for the luminosity measurement depended on the total energy deposited in the luminosity calorimeter. Triggers were constructed using single-arm high threshold triggers, and double-arm low threshold triggers. The efficiencies of those triggers were cross-checked against each other, and against similar downscaled triggers with lower energy thresholds, and the overall trigger efficiency was found to be 100% with an uncertainty of 0.01%.

The trigger rate was typically 4-5 Hz, where Bhabha events in the luminosity calorimeter contributed 2-3 Hz, Z^0 events at the mass peak and two-photon events contributed $\sim$ 0.5 Hz each, and the remainder was accounted for by cosmic rays, noise and beam related background.

Chapter 4

Reconstruction and simulation algorithms

In this chapter some of the algorithms used in the analysis and of common use in ALEPH are described.

4.1 Event simulation

A univoque determination of the primary elementary process in an event is possible only in a few reaction channels; in general the event type can be recognized only on a statistical basis, from the observation of a sufficiently large sample of events. The technique generally used is the so called *"Monte Carlo"* method: both the physical process in its evolution (from the e^+e^- collision to the "visible" particles) and the response of the detector are simulated in order to see how the different event categories behave and how they can be discriminated.

4.1.1 Simulation of the physics process

The simulation of a $e^+e^- \to hadrons$ process is divided in successive steps which reflect the different phases discussed in Sec. 1.3.4. The high-Q^2 processes give origin to a certain number of final state quarks and gluons by means of radiative processes; these partons, when their mutual distances reach the femtometer scale, begin the fragmentation or hadronization process; then, weak decays of the unstable hadrons follow.

The simulated events used in this analysis have been generated with the PYTHIA 5.7 / JETSET 7.4 Monte Carlo [20], which is the most widely used event generator for the simulation of hadronic events (cf. Ref. [60, 61], where this generator is compared to the data in ALEPH). Another commonly used simulation program is HERWIG[21]. The effect of the choice of a particular generator on this analysis is estimated in Sec. 7.1.7 by comparing results obtained with these two Monte Carlo programs.

PYTHIA combines a *Parton Shower* (PS) algorithm with the Lund string fragmentation model. The parton shower represents an approximate perturbative treatment of QCD dynamics at Q^2 scales greater than some infrared cut-off value Q_0^2, typically taken to be of order 1 GeV^2. A quark with initial virtuality Q^2 evolves down in virtuality via successive small-angle gluon emissions. Any parton (quark or gluon) has the possibility to emit an undefined number of other partons, and the final number depends only on the phase space available.

The bulk properties of hadronic events in Z^0 decays are established early in the fragmentation when virtualities are large and perturbative QCD is reliable. It was already stated that the final state hadrons form jets with directions and energies quite close to the ones of the primary energetic partons. The fact that "soft QCD" does not heavily modify the properties of these jets might be a result of several effects. Multiple gluon radiation is restricted in phase space such that subsequent soft gluons cannot be radiated at arbitrarily large angles (this is called *angular ordering*); furthermore, the hadronization phase involves only small momentum transfers, thus the main topological properties of the event remain almost untouched. Therefore, the interface between perturbative and soft QCD is implemented at two levels in PYTHIA: soft gluon emission is introduced in the parton shower, which also includes our knowledge on pQCD; then, at the end of the shower, the partons undergo hadronization.

At this stage quarks and gluons have too low energies to be considered "free". At "distances" ($r \sim 1/\sqrt{Q^2}$) bigger than 1 fm, quarks and gluons are strongly interacting. The "fragmentation" process, in JETSET [62], is described on the basis of the Lund "string model" [63], which describes phenomenologically the quark-antiquark pair as connected by a flux tube which contains all the energy of the pair (see Fig. 4.1) with a linear constant energy density $\kappa \approx 1$ GeV/fm. Increasing the quark-antiquark distance, the energy in the tube increases, reaching at last a value sufficient for a new quark-antiquark pair to be created from the vacuum (by a tunneling effect, or equivalently by the breakup of the flux tube).

The energy spectrum of the hadrons from heavy quarks (b and c) is well parameterized by the Peterson fragmentation function[64], $D_Q^H(z)$. The production by the heavy quark

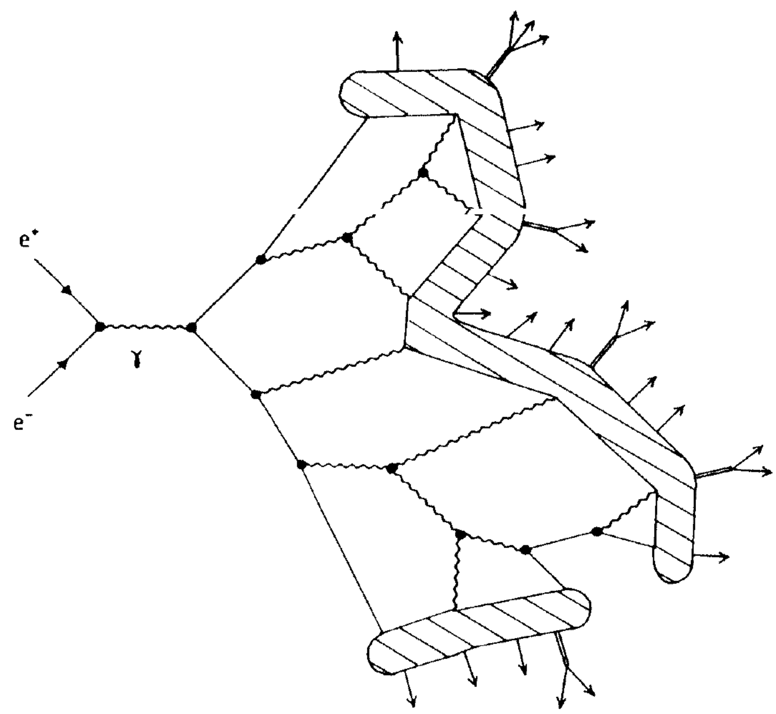

Figure 4.1: Quark fragmentation in the "string model".

Q of a hadron H containing the same flavour and a light quark q[1] is described by means of the parameter z, defined as follows:

$$z = \frac{(E + p_{\|})_{hadron}}{(E + p)_{original\ quark}} \tag{4.1}$$

where $p_{\|}$ is the momentum of the hadron along the direction of the original quark Q. With this notation the fragmentation function is

$$D_Q^H(z) \propto \frac{1}{z[1 - 1/z - \varepsilon_Q/(1-z)^2]^2} \tag{4.2}$$

This expression is monoparametric in $\varepsilon_Q \approx \frac{m_q^2}{m_Q^2}$. Obviously, the z parameter is not accessible experimentally, so it is impossible to directly test $D_Q^H(z)$. At LEP, given the precise knowledge of the beam energy, it is customary to use instead x_E^Q, defined as the ratio between the energy of the heavy hadron and that of the e^+e^- beams:

$$x_E = \frac{E_{\rm hadron}}{E_{\rm beam}} \tag{4.3}$$

Experimental measurements[52, 65] give, for b and c quarks, the following values:

$$\langle x_E^{(b)} \rangle = 0.702 \pm 0.008 \quad \langle x_E^{(c)} \rangle = 0.484 \pm 0.008 \; . \tag{4.4}$$

[1]In the string model the probability of $c\bar{c}$ production is suppressed by roughly eleven orders of magnitude compared to light quark production.

The Monte Carlo has been tuned to those results.

The last step of the simulation concerns the weak decay of the particles with lifetime short enough to decay inside the detector volume. The weak process responsible for these decays is perfectly known at quark level, but when hadrons are considered, the modeling of non-spectator effects is not trivial. The ACCMM model (described in Sec. 1.3.5) is chosen, with the parameters tuned to experimental results.

4.1.2 Simulation of the interaction of the particles with the detector

After the generation of the final state particles, the response of the ALEPH detector has to be taken in account. To simulate it, the structure and composition of the ALEPH detector are implemented in GALEPH, a package based on GEANT [66]. The GEANT program describes the passage of elementary particles through the matter.

Its main applications are the tracking of particles through an experimental detector model for acceptance studies (i.e. the fraction of a certain physics process that is observed in a detector) or simulation of detector response, and the graphical representation of the model and of the particle trajectories.

In GEANT a particle trajectory is a set of points at which a “discrete process” has happened. A discrete process in this respect is either a discrete physical interaction of a particle or its crossing of a volume boundary. From one trajectory point to the next the evolution of the particle is achieved by integrating the equations of motion taking into account the presence of matter.

When tracking particles through a complex structure one of the critical tasks is the estimation of an a priori step size. For a particle with a given energy the step size depends primarily on the intrinsic properties of the particle (mass, charge, lifetime, etc.) and on the characteristics of the current medium. The dependence may be due either to the (quasi)continuous processes which usually impose a limit on the interval of integration (energy loss, multiple scattering, deflection due to magnetic field, etc.) or to the occurrence of a discrete process which introduces a discontinuity in the trajectory (decay, electromagnetic or hadronic interaction). The change of the kinematic parameters (position and energy) according to continuous processes between two discrete ones is applied at the end of the step.

4.2 Track reconstruction and momentum measurement

The reconstruction of charged particle tracks starts from the TPC. From all the TPC raw data (pad or wire number, pulse lenght and arrival time of each pulse) "good" subclusters are selected fulfilling certain criteria (minimum and maximum cluster size, the maximum number of samples in saturation, etc.); for each of these subclusters a three dimensional coordinate and its errors are calculated and corrected for misalignment and distortions of the drift field. A 'chain' is formed from a set of coordinates, no more than one per pad row, consistent with an arc of a helix. The chains belonging to the same helix are linked together into a single "track candidate" (see Fig. 4.2). From the fit of a helix to the pad coordinates within the first half turn of each track candidate (with the possibility to remove outlying coordinates and to break a track between two coordinates) five parameters (R, ϕ_0, d_0, z_0 and $\tan\lambda$ in Fig. 4.2) are determined. In the end, a set of TPC-fitted tracks is obtained.

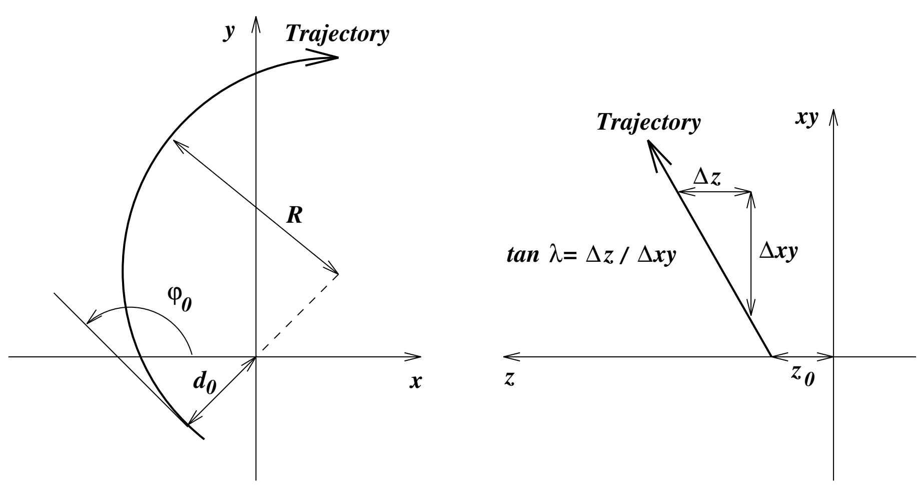

Figure 4.2: Helix parameters used in the tracking programs.

These TPC-tracks are then extrapolated to ITC, where consistent hits are assigned (taking into account the resolution of ITC, the precision of the extrapolation and the possible multiple scattering between the ITC and TPC). A χ^2 is computed from the coordinates and their errors, measured in TPC and ITC, with multiple scattering included. If χ^2 is greater than a given value, the ITC point is not included.

The tracks found in TPC+ITC are then extrapolated in the same way to VDET, where two points could be further associated. The final overall fit (up to 31 points: 21 in

TPC, 8 in ITC and 2 in VDET), based on the Kalman filtering technique [67], gives the five parameters of the helix.

The transverse momentum of a charged track is determined from the curvature of the track in the TPC, knowing the magnetic field ($p_T = qBR$); from the transverse momentum the total momentum is found as $p = p_T/\sin\theta$.

The track finding efficiency, studied with MC simulations, was determined to be 98.6% for tracks in hadronic events that have at least four hits in TPC pads. The small inefficiency, due to track overlaps and cracks, is reproduced to better than 10^{-3} by the simulation. The efficiency of associating a VDET hit to an isolated track is about 94% per layer, within the geometrical acceptance. The performance of the track reconstruction is studied using $Z^0 \to \mu^+\mu^-$ decays. Fig. 4.3 shows the ratio of the beam energy to the measured momentum for tracks from dimuon events. Here a track is required to have at least 19 TPC hits, at least six ITC hits and at least one VDET hit in the $r\phi$ plane. The acollinearity angle between the positive and the negative muon is required to be smaller than 0.2° in order to eliminate events in which part of the final state momentum is carried by a photon. These events are also removed by requiring the sum of the energies of all clusters in the electromagnetic calorimeter which are not associated with the two muons to be less than 100 MeV. A transverse momentum resolution of

$$\sigma(1/p_T) = 0.6 \times 10^{-3} (\mathrm{GeV}/c)^{-1} \tag{4.5}$$

is measured (for 45 GeV muons). Table 4.1 summarizes the measured resolution for TPC only, for TPC and ITC, and for all the three tracking detectors together. At low momentum multiple scattering dominates and adds a constant term of 0.005 to $\sigma(p_T)/p_T$.

Detector	$\sigma(1/p_T)$ $(\mathrm{GeV}/c)^{-1}$
TPC	1.2×10^{-3}
TPC+ITC	0.8×10^{-3}
TPC+ITC+VDET	0.6×10^{-3}

Table 4.1: Transverse momentum resolution; the successive rows show the effect of including the detectors indicated in the fit.

The angular and momentum resolution of the tracking system both contribute to the precision achieved on the invariant mass of states that decay into charged particles. This is illustrated in Fig. 4.4, where the $\mu^+\mu^-$ invariant mass spectrum is shown, with a clear peak seen in correspondence to the J/ψ mass; the resolution on the mass is 25 MeV/c^2.

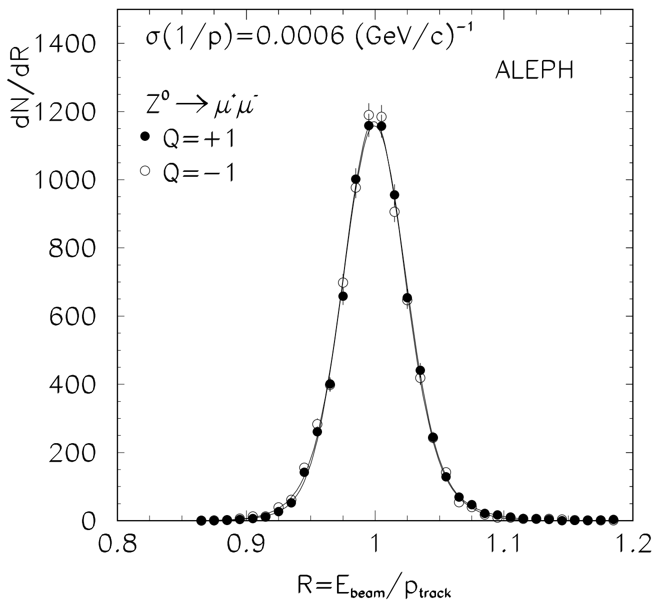

Figure 4.3: The ratio of the beam energy to the track momentum measured in the tracking system for muons from $Z^0 \to \mu^+\mu^-$ decays.

4.3 Energy flow measurement

To measure the total energy released in the whole detector, an *"Energy flow"*[56] algorithm has been developed in ALEPH, combining charged particle measured momenta and calorimetric information.

The first stage of the algorithm ("cleaning") selects the charged tracks that originate from the interaction point or from a reconstructed neutral vertex (a V^0, i.e. a long lived neutral particle which decays in a pair of oppositely charged particles) and rejects those tracks and calorimeter clusters which could originate from the rare misbehaviors of the front-end electronics, the data acquisition system or the reconstruction chain:

1. the charged particle tracks are required to have at least four hits in the TPC and to originate from within a cylinder of length 20 cm and radius 2 cm coaxial with the beam and centered at the nominal collision point (if $p > 15$ GeV/c at least eight points are required in the TPC and one in the ITC);

2. the charged particle tracks rejected by this selection are recovered if they belong to a reconstructed V^0 compatible with originating from the nominal collision point

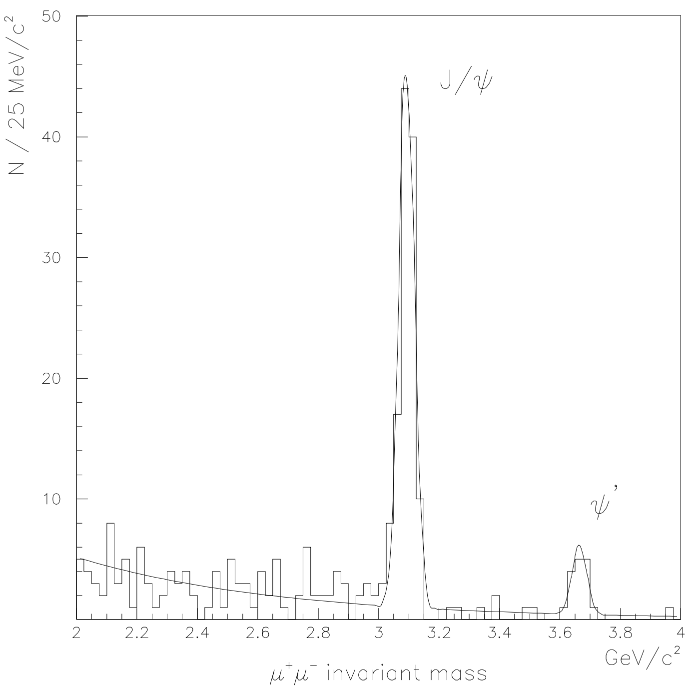

Figure 4.4: Invariant mass of $\mu^+\mu^-$ pairs, showing a peak at the J/ψ mass (and also at the ψ' mass). The superimposed fit is of Gaussian type for the peaks with an exponential background.

within a cylinder of length 30 cm and radius 5 cm coaxial with the beam;

3. the noisy channels of the ECAL and HCAL, appearing systematically in many consecutive events, are located prior to the event reconstruction and are not used in the cluster finding;

4. the fake energy deposits due to occasional noise in the towers of the calorimeters are detected and removed when the corresponding signal is incompatible with the signal measured independently on the wire planes.

The efficiency of the last step of this cleaning procedure can be tested on events randomly triggered where no signal should be present. Fig. 4.5 shows the energy distribution for events randomly triggered, before and after this cleaning. Before the cleaning, one third of these events contains a fake signal in the calorimeters, with a mean value of 1 GeV; after the cleaning, no energy remains in 98% of these events and the mean energy becomes 15 MeV per event. Thanks to the redundancy in the readout of both calorimeters, the real signal is not noticeably affected by this efficient cleaning stage.

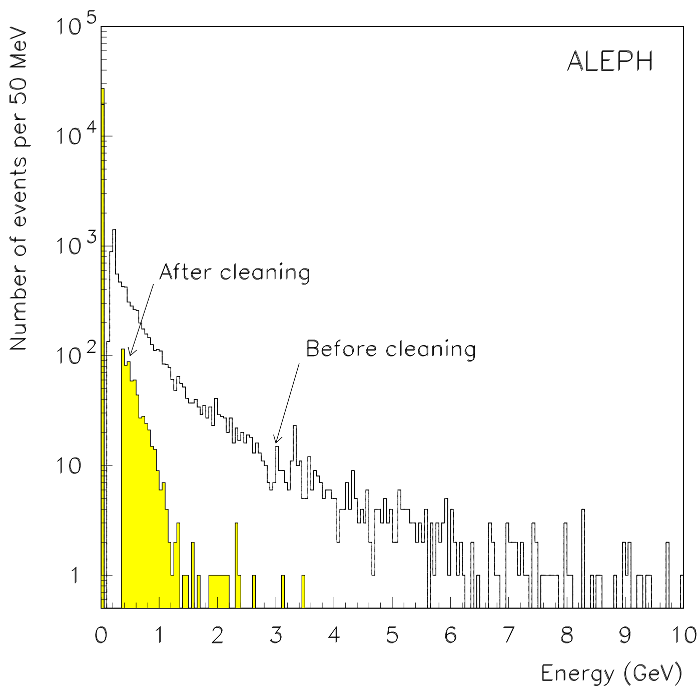

Figure 4.5: Energy distribution for events randomly triggered, before (empty histogram) and after (shaded histogram) cleaning. The gap after cleaning at low energy results from the energy threshold for identifying photon clusters.

After the cleaning, the selected charged tracks are extrapolated to the calorimeters and groups of topologically connected tracks and clusters, called “calorimeter objects”, are formed.

For each event, the magnitude and direction of the energy flow is reconstructed using:

- charged particle tracks survived to the cleaning procedure, which are counted as charged energy;
- V^0's;
- photons, identified as clusters in the electromagnetic calorimeter, which are counted as neutral electromagnetic energy;
- the remaining neutral hadronic energy is determined from the calorimeter clusters; for every cluster, the neutral hadronic energy is evaluated as $E_n = E_h + rE_e - E_c$, where:

- E_c is the charged track energy topologically associated to the cluster, and not identified as an electron or muon;
- E_e is the energy in ECAL not attributed to e (see Sec. 4.7.1) or γ;
- E_h is the energy in HCAL not attributed to μ (see Sec. 4.7.3);
- r is the response ratio for electrons over pions in the ECAL ($r \approx 1.3$).

The resolution on the total energy with this method is determined using the hadronic events selected as in Sec. 6.2 accompanied by an isolated energetic photon or π^0 (see Fig. 4.6). These events provide two methods for the determination of the visible mass m_{vis} using the energy flow algorithm, and the computation of the mass m_{rec} recoiling against the precisely determined photon energy E_γ. This mass is given by $m_{rec}^2 = s - 2E_\gamma\sqrt{s}$, allowing hadronic masses below 70 GeV/c^2 to be tested.

The result is:

$$\sigma(E) = (0.59 \pm 0.03)\sqrt{E/GeV} + (0.6 \pm 0.3)GeV \tag{4.6}$$

which is considerably better than the resolution obtained by simply adding the raw energy of all calorimetric cells, that is

$$\sigma(E) = 1.2\sqrt{E/GeV}GeV \tag{4.7}$$

4.4 dE/dx measurement

The energy loss by ionization for a particle traversing the TPC is measured combining the informations given from the TPC sense wires and from the TPC pads.

Wire hits are associated with the fitted TPC tracks using a window in drift time around the projected helix positions. When the wire pulse is associated to more than a track, it is impossible to distinguish the individual contribution, and the measurement for that particular wire is ignored. This leads to an average inefficiency of about 15% in the hadronic environment, while the pad information is available for all tracks.

The sensitivity to the nominal ADC threshold is minimized by rejecting the lowest 8% of the hits, ordered by pulse height, when calculating the mean dE/dx. This worsens the resolution but gives a dE/dx estimator independent of the track angle and drift length. In addition, the large fluctuations due to the Landau tail are suppressed by omitting the highest 40% of the hits.

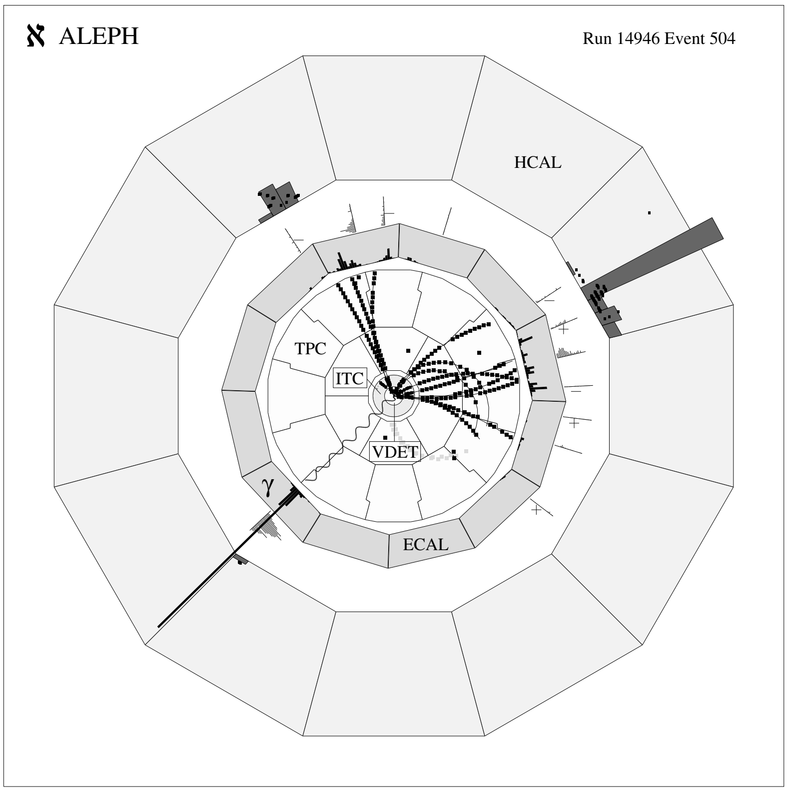

Figure 4.6: An hadronic event accompanied by an isolated energetic photon, represented by a wiggly line, carrying an energy of (30.8 ± 1.1) GeV. The mass recoiling against the photon is (52.0 ± 1.9) GeV/c^2, while the visible mass of the hadronic system is (53.6 ± 4.9) GeV/c^2.

Since the TPC operates at atmospheric pressure, the effective gain changes from run to run, with a measured pressure ($\mathcal{P}$) dependence of $\mathcal{P}^{-3.7}$. The gain is calibrated directly from data using minimum-ionizing pions in the momentum range from 0.3 GeV/c to 0.6 GeV/c, i.e. the momentum interval where pions are most easily separable from the other particle types (see Fig. 4.7). The gain is arbitrarily normalized such that minimum-ionizing particles have $\langle dE/dx \rangle = 1$.

For a track in the TPC, two estimators are constructed for the specific energy loss by ionization, for every particle hypothesis considered, from wires and pad outputs respectively. The wires estimator is defined as

$$R_I^w \equiv \frac{(dE/dx)^w - \langle dE/dx \rangle_i^w}{\sigma_{dE/dx}^w} \tag{4.8}$$

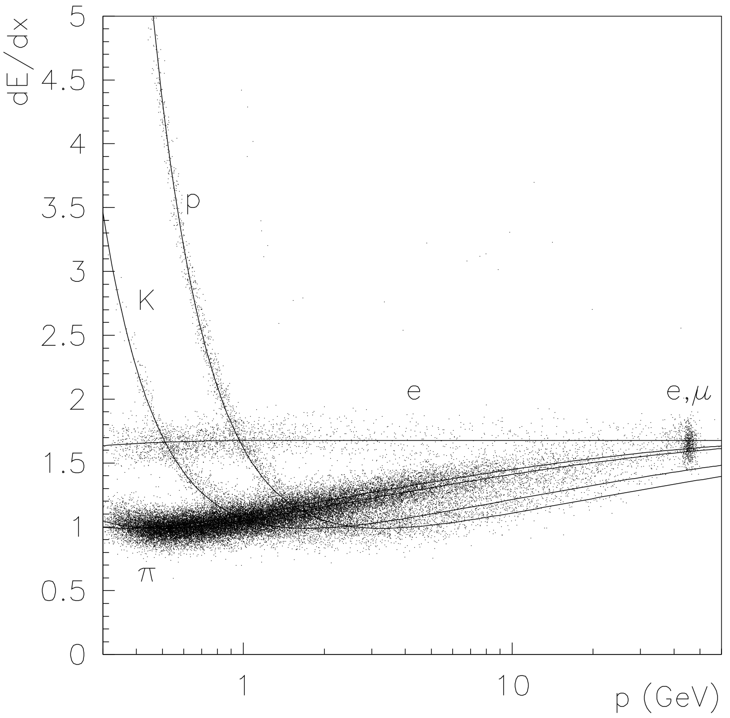

Figure 4.7: dE/dx as a function of momentum for electrons, pions, kaons and protons.

where $\langle dE/dx \rangle_i^w$ is the specific energy loss expected for particle type i. A similar equation defines the pad estimator R_I^p, and a new estimator R_I is built from those two. For tracks that do not fulfil the requirement on the minimum number of isolated wire signals, $R_I = R_I^p$; otherwise it combines wire and pad information using the B.L.U.E. technique (described in Sec. 8.1), taking into account the correlation of about 50% between the two measurements.

The dependence of the mean dE/dx on particle velocity is measured from data using a variety of event types. Minimum-ionizing pions fix the minimum of the curve, protons are used to fit the low momentum $1/\beta^2$ region, Bhabha events give the plateau position, and muons from $Z^0 \rightarrow \mu^+\mu^-$ and from tau decays give points slightly below the plateau. The mean dE/dx of pions in the *relativistic rise* region is determined from fits to dE/dx measurements in hadronic events (and checked with pions from tau decay) as follows. In hadronic events, each momentum bin is fitted to a sum of four Gaussian contributions, for electrons, pions, kaons and protons, with only the position of the pion peak and the normalizations of the four contributions allowed to vary. The results of the fits for the position of the pion peak are then combined with the points from protons, minimum-ionizing pions, and dileptons in a fit of a modified Bethe-Bloch formula with six free parameters. The parameterization obtained after several iterations of this procedure is plotted for a sample of the data in Fig. 4.7. The height of the plateau relative to minimum ionization is found to be 1.66.

Since the goal of measuring dE/dx is particle identification, the interesting quantity is the number of standard deviations of distance between the different particle species, as shown in Fig. 4.8.

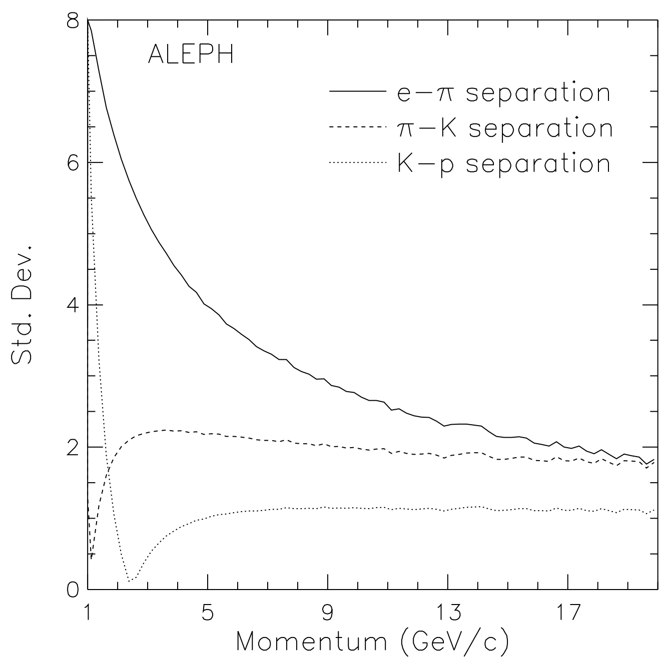

Figure 4.8: Mean separation in standard deviations for several particles in hadronic Z^0 decays.

4.5 Hadronic jets reconstruction

After the reconstruction of the charged tracks (see Sec. 4.2), and the identification of the neutral particles by means of the deposits in the calorimeters (see Sec. 4.3), it is possible to give a first physical interpretation of the event. This is quite simple when studying the leptonic decays of the Z^0, since only a few particles are produced, but in hadronic Z^0 decays the multiplicity is higher (usually more than 10 charged tracks).

The grouping ("clustering") of particles in jets is performed by specific algorithms, which can be of various types, reflecting the arbitrariness of the grouping criteria. In this analysis, the JADE[68] algorithm is chosen, with the "E-scheme". This algorithm scans the calorimetric objects reconstructed in the event, looking for the pair (i and j) having the smallest invariant mass in the zero particle mass approximation (justified at the high energies involved), i.e. using the formula

$$M_{ij}^2 = 2E_iE_j(1 - \cos\theta_{ij}) \ . \tag{4.9}$$

For the pair of objects which minimizes this relation, it is checked if the following inequality holds:

$$(M_{ij}/E_{vis})^2 < y_{cut} \ , \tag{4.10}$$

where E_{vis} is the total energy measured in the event, while y_{cut} is the adjustable resolution parameter. It determines the masses of the jets.

If the pair (i, j) satisfies the inequality 4.10, the two objects are merged into a single pseudo-object ij, with a four-vector

$$\vec{p}_{ij} = \vec{p}_i + \vec{p}_j \tag{4.11}$$

$$E_{ij} = E_i + E_j \tag{4.12}$$

(i.e., the usual sum of two four-vectors; other schemes use different sum rules).

At this point a new scan begins on the new set of objects, and so on, iteratively, until no pair of pseudo-objects satisfies relation 4.10. The remaining pseudo-objects are called "jets".

The y_{cut} parameter determines the number of hadronic jets in the output of the algorithm: a high value (e.g. 0.07) means "masses" up to ≈ 45 GeV^2, so that simple phase space arguments limit the number of jets.

A modification of the JADE algorithm, used in this analysis, permits to choose a fixed number of jets in the event, stopping the clustering when the desired number of pseudo-objects is reached.

[2] As said, JADE uses an approximate invariant mass relation, so that the "real" mass of a jet has not this value as upper limit.

4.6 Heavy quarks identification based on impact parameter

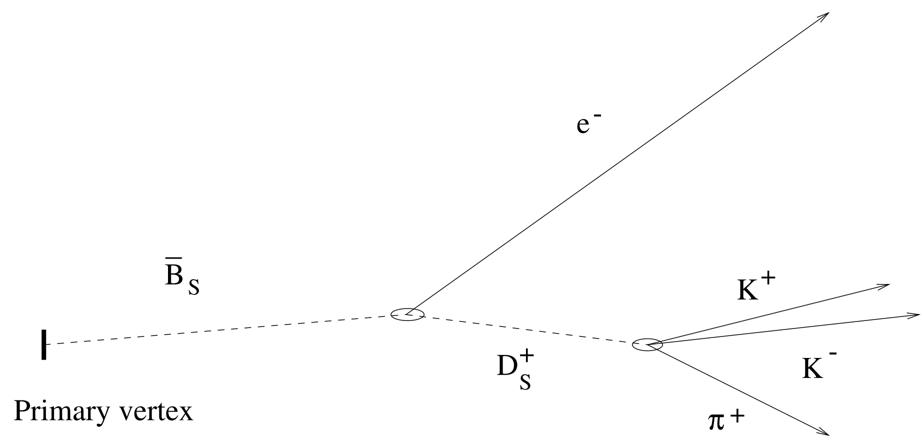

Figure 4.9: An example of b hadron decay.

This section describes the QIPBTAG algorithm [30], a procedure which allows to discriminate between tracks coming from the decays of particles with "long" lifetime ($10^{-11} - 10^{-12}$ sec) and tracks originating directly from the primary interaction vertex, by means of the track *impact parameter*.

The secondary decay vertex of a hadron containing a b quark has an average distance from the primary vertex of 2.5 mm at LEP, and this distance can be accessed thanks to the information from VDET. Figure 4.9 shows a b hadron decay following the $b \to c \to s$ chain.

After the clustering into jets, the trajectories of the charged tracks are linearized in their point of maximum approach to the jet axis (point S in figure 4.10). The impact parameter [69] is defined as the distance D of nearest approach between the linearized trajectory and the primary vertex V of the event; its sign is defined as positive if the vector joining V with S points in the direction of the jet, negative otherwise.

The impact parameter resolution for high momentum charged particles is measured in $Z^0 \to \mu^+\mu^-$ events from the distance between the two tracks at the interaction point, obtaining 23 μm in the $r\phi$ view and 28 μm in the rz view for tracks measured in all three tracking detectors. Table 4.2 summarizes the impact parameter results for high momentum tracks when detectors are successively included in the fit.

The impact parameter resolution of lower momentum charged particles is measured in hadronic Z^0 decays. The impact parameter D is measured relative to an event-by-event

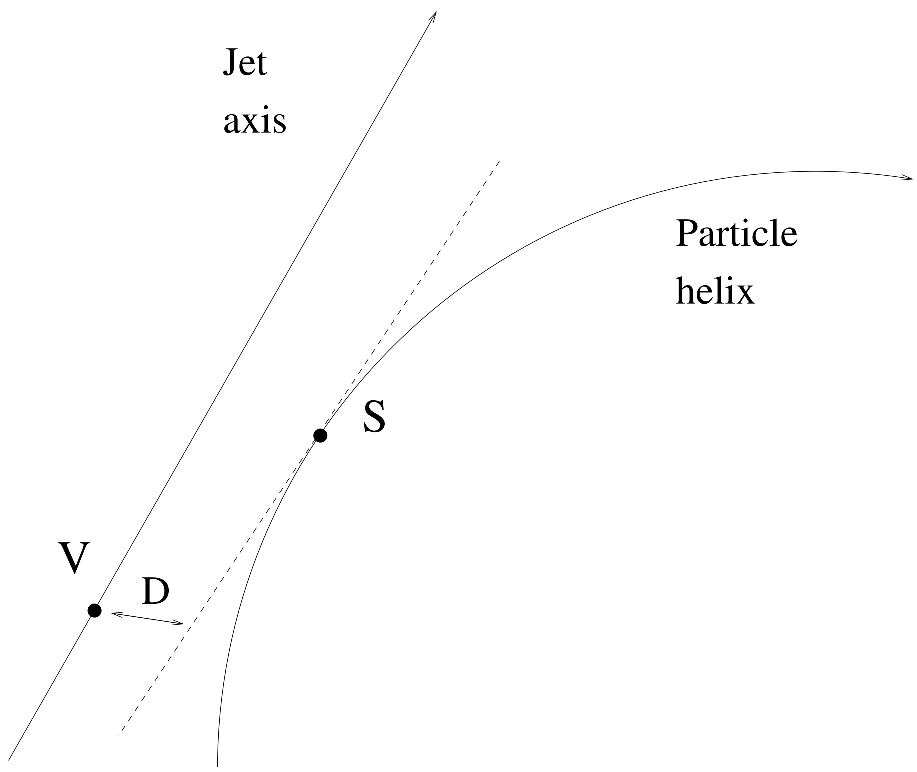

Figure 4.10: Impact parameter determination. S is the point of the helix nearest to the jet axis, D the minimum distance between the linearized trajectory and the primary vertex V.

Detector	$r\phi$ (μm)	rz (μm)
TPC	310	808
TPC+ITC	107	808
TPC+ITC+VDET	23	28

Table 4.2: Impact parameter resolution; the successive rows show the effect of including the detectors indicated in the fit.

reconstructed Z^0 decay vertex.

The quantity of interest is not the impact parameter itself, but its "significance": $\Delta \equiv D/\sigma_D$, where σ_D is the statistical error on the impact parameter and takes into account the uncertainties on the fit of the track and on the primary vertex reconstruction. It can be demonstrated that for events without any secondary vertex, if the reconstruction errors were strictly gaussian, the resolution function $\frac{dN^{uds}}{d\Delta}$ would be $|\Delta|e^{-\Delta^2/2\sigma^2}$. This is the main contribution to the Δ distribution, but a better description is obtained adding to this two independent exponential functions of type $|\Delta|e^{-\Delta/\lambda}$, which give a tail with slower decrease.

The function which describes properly the distribution of negative Δ is called *resolution function* ($\mathcal{R}(\Delta)$). The impact parameter resolution is taken as the r.m.s. of this distribution, subtracting the estimated primary vertex resolution in quadrature.

Fig. 4.11 shows the impact parameter resolution for tracks with VDET hits in both layers, as a function of momentum, in $r\phi$ and rz views. The resolution can be parameterized as

$$\sigma(D) = 25\mu\text{m} + \frac{95\mu\text{m}}{p(\text{GeV}/c)} , \tag{4.13}$$

in both the $r\phi$ and rz views.

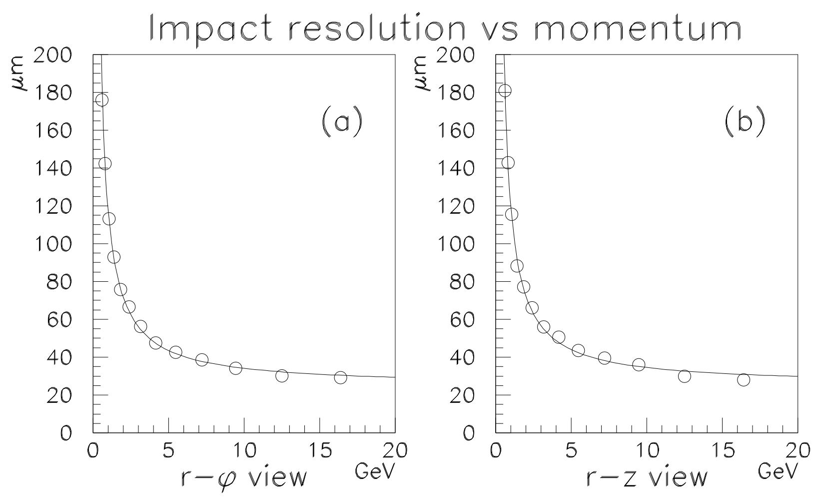

Figure 4.11: The impact parameter resolution for tracks with two VDET hits as a function of their momentum in (a) the $r\phi$ view and (b) the rz view.

$\mathcal{R}(\Delta)$ is used to define the probability that a track with positive $\Delta \geq \Delta_0$ comes from the primary vertex, as:

$$\mathcal{P}(\Delta_0) = \int_{\Delta_0}^{+\infty} \mathcal{R}(\Delta) d\Delta \tag{4.14}$$

$\mathcal{R}(\Delta)$ is measured from events with $\Delta < 0$, and for $\Delta > 0$ is defined by symmetry: $\mathcal{R}(\Delta) = \mathcal{R}(-\Delta)$. This definition implies that for tracks coming from the primary vertex the $\frac{dN^{uds}}{d\mathcal{P}}$ distribution is constant. In fact:

$$\frac{dN^{uds}}{d\mathcal{P}} = \frac{\partial N^{uds}}{\partial \Delta} \times \frac{\partial \Delta}{\partial \mathcal{P}}$$

but, by definition, $\frac{\partial \mathcal{P}(\Delta)}{\partial \Delta} = -\mathcal{R}(\Delta)$ and $\frac{\partial N^{uds}}{\partial \Delta} = \mathcal{R}(\Delta)$, so that $\frac{dN^{uds}}{d\mathcal{P}}$ is constant for tracks from the primary vertex. But for tracks from the decay of a "long" lived particle,

$\frac{dN^b}{d\mathcal{P}}$ is far from being flat; in particular, there is an excess (with respect to the flatness hypothesis) with very low probability of coming from the interaction point.

This algorithm is useful only for tracks with a signal in VDET (at least one hit), since ITC and TPC are too far from the interaction point to give a reliable information when extrapolating the track back to the primary vertex (see Tab. 4.2).

What said above concerns a single track; in this analysis also a combined probability for hemispheres is used.

For a group of N tracks with positive impact parameter a combined probability [70] is defined as:

$$\mathcal{P}_N \equiv \Pi \cdot \sum_{j=0}^{N-1} \frac{(-\ln \Pi)^j}{j!} , \tag{4.15}$$

where

$$\Pi \equiv \prod_{i=1}^{N} \mathcal{P}_i$$

and $\mathcal{P}_i$ is the probability that track number i comes from the primary vertex. $\mathcal{P}_N$ is the confidence level that in a set of N tracks coming from the interaction vertex, the product of the single probabilities is lower than Π.

The $\mathcal{P}^1_{hemi}$ and $\mathcal{P}^2_{hemi}$ variables, constructed as in Eq. 4.15 with the tracks belonging to the first and the second hemisphere respectively, have lower values for hemispheres containing secondary vertices, and this is very useful to reject events with b's (both from Z^0 and from gluon splitting), which are a very important background in this analysis, as shown later.

4.7 Lepton identification

The lepton identification is of paramount importance in this thesis, since this measurement makes use of the $g \to c \to l$ ($l = e, \mu$) decay chain.

Lepton candidates might come from one of the following processes [71]:

1. *Prompt leptons* from semileptonic decays of heavy flavoured hadrons: $b \to l$ and $c \to l$.

2. *Non-prompt leptons* from decay of light flavoured hadrons such as Dalitz decay of neutral pions ($\pi^0 \to \gamma e^+ e^-$), leptonic decay-in-flight of charged hadrons ($\pi, K \to \mu\nu$) and conversions of photons in the detector material ($\gamma \to e^+ e^-$).

3. Hadrons misidentified as leptons (*fake leptons*).

In this section the electron and muon identification criteria are described, along with a discussion of the sources of contamination.

4.7.1 Electron identification

The electrons are identified using the characteristic ionization (dE/dx) measurements from the TPC and the energy released in ECAL.

The dE/dx measurement is a powerful tool to identify electrons; as shown in Fig. 4.7, the electron energy loss in the TPC gas is localized in the plateau, while the other charged particles are on the relativistic rise region. The electron-pion separation is larger than 3σ up to $p \approx 8$ GeV/c.

Furthermore, as the probability of emitting a bremsstrahlung photon is proportional to $\frac{1}{m^2}$, and electrons have a low mass (0.511 MeV/c^2), they are the most electromagnetically active of all charged particles. The process known as "electromagnetic shower" begins with the emission of a bremsstrahlung photon in a dense absorber (in our case, the ECAL lead), followed by several $\gamma \to e^+e^-$ and $e \to e\gamma$ steps. The shower is detected by the induced ionization in the active material (the gas of the chambers located between the lead sheets).

Three estimators are defined for each charged track: R_I defined as in Sec. 4.4, and R_T and R_L (described in the following) which take into account the fact that the electromagnetic showers initiated by an electron are characterized by the compactness of the energy deposition around the original track direction and its longitudinal shape. Cuts on these estimators are used to select electron candidates.

The track is extrapolated from TPC to ECAL and its crossing point is computed in each of the three stacks. For every stack the four segments nearest to the extrapolated track are considered and the energy fraction released in those segments (E_4/p) is computed. The estimator R_T is built to compare this to the energy fraction expected in the electron hypothesis:

$$R_T \equiv \frac{E_4/p - \overline{E_4/p}_{el}}{\sigma_{E_4/p}} \tag{4.16}$$

Another parameter used to identify electrons is the depth of the electromagnetic shower in ECAL. The depth X_L of the maximum energy release along the shower is used to build the estimator R_L:

$$R_L \equiv \frac{X_L^{-1} - \overline{X_L^{-1}}_{el}}{\sigma_{X_L^{-1}}} \tag{4.17}$$

Fig. 4.12 shows how the electron candidates are distributed in the $R_L - R_T$ plane. True electrons are clustered around the (0,0) point.

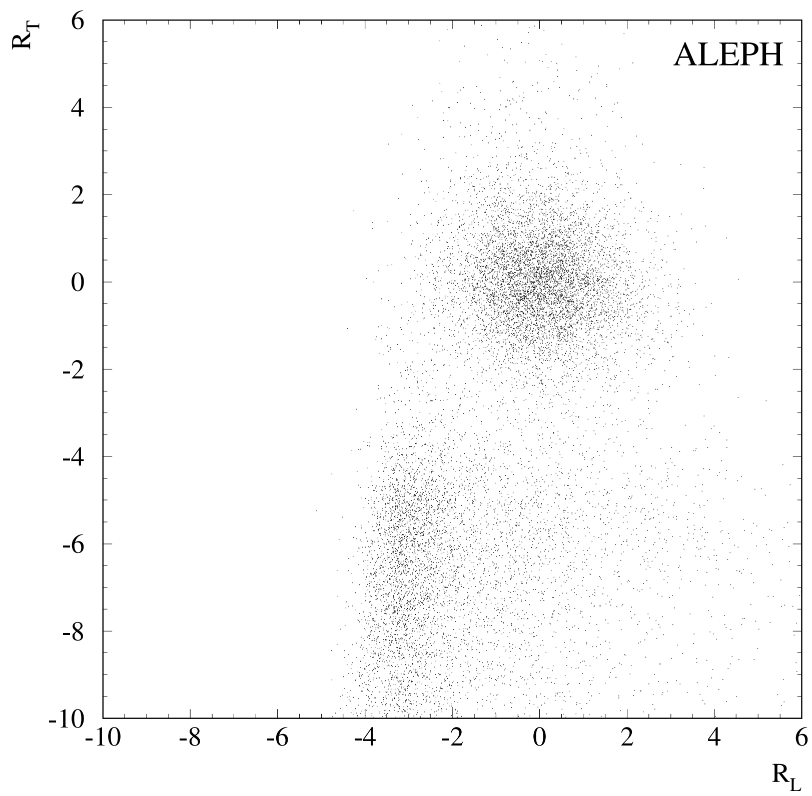

Figure 4.12: ECAL estimators for electron candidates.

The cuts applied to the estimators for an electron candidate in a hadronic Z^0 decay are: $R_I > -2.0$, $-1.8 < R_L < 3.0$ and $R_T > -1.6$. In addition, the momentum of the selected track must be greater than 2 GeV/c.

4.7.2 Non-prompt and fake electrons

The background is estimated from the Monte Carlo to be 31% of the electron sample (see Tab. 4.3 for details).

prompt e's	69%
$\gamma \to ee$	26%
misidentified π	4%
others	1%

Table 4.3: Composition of the electron sample after the preselection cuts that will be discussed in Sec. 6.4.

The reliability of this estimate of the composition of the electron sample has been checked [72] by removing the cut on the energy loss, and studying the shape of the R_I estimator. This study is performed in data and Monte Carlo and no significant deviation is observed. An uncertainty of 20% on the background level is assigned from the statistical precision of the method, and taken into account when estimating the systematic uncertainty on $g_{c\bar{c}}$ (see Sec. 7.1.6).

The background from unidentified photon conversions ($\gamma \to e^+e^-$) is estimated by studying the shape of the variable

$$\rho_\gamma = q d_0 p_T \ , \tag{4.18}$$

where q is the charge of the track, d_0 is the distance of closest approach to the primary vertex in the xy plane signed according to the track angular momentum around the origin, and p_T is the component of the track momentum transverse to the beam axis (see Sec. 4.2). The variable ρ_γ is expected to be zero for prompt electrons and proportional to the square of the materialization radius for electrons coming from photon conversions. The study of the positive tail of the distribution yields a correction factor of 1.05 to be applied to the simulation, with a statistical error of 0.02. The correction factor is removed to estimate the systematic uncertainty in Sec. 7.1.6.

4.7.3 Muon identification

Muons, in contrast to electrons, are the most penetrating of the charged particles commonly produced in hadronic Z^0 decays. With a mass of 200 times the electron mass, the muon has a probability of 2.5×10^{-5} of the electron for the production of bremsstrahlung photons; so, very few muons initiate electromagnetic showers. Hence, muons penetrate through the thick material of the detector while other charged particles are absorbed.

Muons in ALEPH are identified using the digital signals of the strips in HCAL and the muon chamber information.

The tracks considered for muon identification in hadronic jets must have a momentum greater than 2.5 GeV/c and must penetrate through the whole depth of HCAL. Around the track, a "road" is defined, whose width is three times the estimated standard deviation for multiple scattering[3]. The extrapolated track is considered penetrating if:

- it intersects at least ten planes in HCAL
- the number of planes which give a signal inside the 'road' in the last 10 expected planes is greater than 4
- the ratio between the number of planes which give a signal in the 'road' and the total number of expected ones is greater or equal to 0.4.

In addition, the cut $X_{mult} < 1.5$ is applied, where X_{mult} is obtained by counting the number of hits within a distance of 30 cm from the extrapolated track in the last 11 HCAL planes and dividing it by the number of planes giving signals. In this way, X_{mult} can be considered an estimator of the multiplicity of particles originating from the muon candidate in traversing HCAL. This cut reduces the hadron background by a factor of two, losing just 1% of the muons.

For what concerns the selection in the muon chambers, the distance between the extrapolated track and a reconstructed hit must be less than four times the estimated standard deviation for multiple scattering.

4.7.4 Non-prompt and fake muons

A light hadron (K, π), or a light hadron decaying to a muon within the tracking volume ($K \to \mu$, $\pi \to \mu$), can be selected by the muon identification algorithm with a certain probability. Table 4.4 shows the composition of the muon sample after the muon selection cuts listed in Sec. 4.7.3 and the additional requests, present also in the preselection described in Sec. 6.4, of $|d_0| < 0.1$ cm (where d_0 is the distance of closest approach of the track to the beam axis) and at least one hit in the VDET.

Two high-purity samples of light hadrons have been selected in data and Monte Carlo, and the muon selection has been applied to them, comparing the resulting efficiencies.

[3] For example, the road for a 45 GeV/c muon is 3 cm wide, and about 15 cm wide for a 3 GeV/c muon.

prompt μ's	56%
$\pi \to \mu\nu$	25%
misidentified π's	10%
$K \to \mu\nu$	5%
misidentified K's	3%
others	1%

Table 4.4: Composition of the muon sample after the preselection cuts (Sec. 6.4).

The first sample is selected inclusively by means of a dedicated "uds" tag, designed to select event hemispheres that do not contain decay products of heavy flavoured particles. Such a tag is based on:

- the lack or presence of secondary vertices (*uds* events do not contain any);
- the momentum of the fastest charged particle (heavy quark decays produce fast particles, due to the large mass difference between initial and final states);
- the total visible energy (the presence of neutrinos from heavy quark semileptonic decays results in a large missing energy);
- the lack or presence of prompt lepton candidates and their transverse momentum with respect to the jet axis (prompt leptons mostly come from heavy quark decay, and their transverse momentum is related to the mass difference between initial and final states);
- the momentum of the softest pion (very soft pions are produced by the decay $D^{*\pm} \to D^0\pi^{\pm}$, since $M(D^*)-M(D^0) \approx M(\pi)$, see Sec. 2.3.1, and this provides an additional specific anti-c criterion; the "soft pion" method as used in ALEPH is described in Ref. [73]).

These informations are combined in a global variable, shown in Fig. 4.13. A cut is performed on this variable at 0.95, yielding a *uds* purity of 93.3%.

A second sample is obtained by reconstructing K^0_S decays in charged pions, as in [74]. The candidates are required to have a decay length larger than 1 cm, and an invariant mass in a window of width $(0.014+0.3P_K/\sqrt{s})$ GeV/c^2 around the nominal K^0_S mass. The contamination of prompt muons from heavy flavour decays is further reduced by applying to the event a mild cut (0.5) on the uds-tag variable described above. With these cuts, 93% of the selected events contain a $K^0_S \to \pi^+\pi^-$ decay.

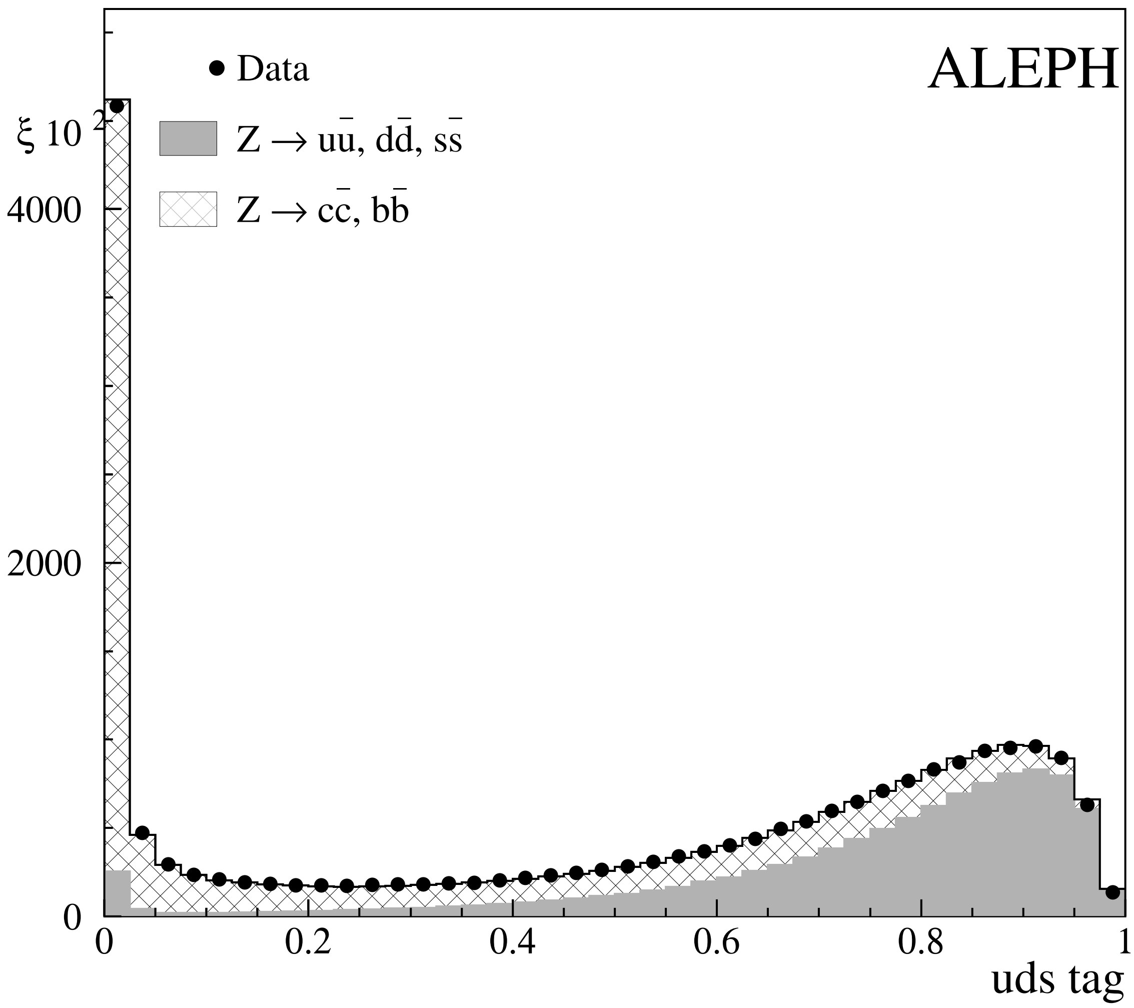

Figure 4.13: Distribution of the *uds* tag combined variable.

	Simulation	Data
Number of tracks (N_{tot})	564396	332103
Number of prompt μ (N_μ)	432	—
Tracks identified as μ (n_{tot})	3072	2077
Prompt μ identified as μ (n_μ)	351	—
Mistag (10^{-3})	4.83 ± 0.08	5.64 ± 0.13

Table 4.5: Performance of the prompt-muon identification on *uds*-fragmentation hadrons.

The number of tracks selected and identified as muons in data and simulation are shown, for the two samples, in Tables 4.5 and 4.6. The mistag probability in the data is calculated after subtracting the prompt muon component estimated from the simulation,

	Simulation	Data
Number of tracks (N_{tot})	113068	50162
Number of prompt μ (N_{μ})	199	—
Tracks identified as μ (n_{tot})	662	326
Prompt μ identified as μ (n_{μ})	156	—
Mistag (10^{-3})	4.48 ± 0.20	5.13 ± 0.31

Table 4.6: Performance of the prompt-muon identification on pions from K^0_S decays.

as

$$\epsilon^{\text{mistag}}_{\text{data}} = \frac{n^{DT}_{tot} - n^{DT}_{\mu}}{N^{DT}_{tot} - N^{DT}_{\mu}} , \tag{4.19}$$

where N^{DT}_{μ} is estimated as the total number of tracks N^{DT}_{tot} in the data sample times the fraction $C_{\mu} \equiv N^{MC}_{\mu}/N^{MC}_{tot}$ of prompt muons in the selected Monte Carlo sample, while n^{DT}_{μ} is calculated as N^{DT}_{μ} times the ratio $n^{MC}_{\mu}/N^{MC}_{\mu}$. This is compared to

$$\epsilon^{\text{mistag}}_{\text{MC}} = \frac{n^{MC}_{tot} - n^{MC}_{\mu}}{N^{MC}_{tot} - N^{MC}_{\mu}} \tag{4.20}$$

where N^{MC}_{μ} and n^{MC}_{μ} are directly counted since in the Monte Carlo it is possible to access the "true" identity of a track.

The two samples (fragmentation pions and $K^0_S \to \pi^+\pi^-$) consistently indicate that the mistag probability is higher in data than in the simulation, by the ratios 1.17 ± 0.03 and 1.15 ± 0.09. A correction factor of 1.17 ± 0.05 has been conservatively applied to the simulation. The resulting uncertainty on the measurement is taken into account in Sec. 7.1.6.

Chapter 5

Neural Networks

Neural networks [75, 76, 77, 78] (NN) are a powerful tool for pattern recognition, and are widely applied in several fields, ranging from financial predictions to weather forecasts to character recognition. In particle physics they are mostly used for event or particle classification tasks.

The analysis described in this dissertation makes use of a neural network to separate the $g \to c\bar{c}$ events from the backgrounds.

5.1 What is a Neural Network

Several definitions exist of what is meant by "neural network". One of the most agreed on is the following [76]:

A neural network is an interconnected assembly of simple processing elements, **units** *or* **nodes***, whose functionality is loosely based on the animal neuron. The processing ability of the network is stored in the inter-unit connection strengths, or weights, obtained by a process of adaptation to, or* **learning from***, a set of training patterns.*

The "neuron" is the fundamental processing element of a neural network. It takes its name from the analogy with the cells responsible of signal transmission in the brain.

The information processing performed by the real (biological) neuron may be crudely summarized as follows: it receives inputs from other neurons (or from the surrounding environment), combines them in some way, performs a generally non-linear operation on the result, and then outputs the final result. The artificial neuron mimics the real one by multiplying the input values by some number or weight to indicate the strength of the link (the "synapse", following the biological similitude); the weighted signals are then summed to produce an overall unit activation. If this activation exceeds a certain threshold the unit produces an output response. This functionality is captured in the artificial neuron known as the Threshold Logic Unit (TLU) (see Fig. 5.1).

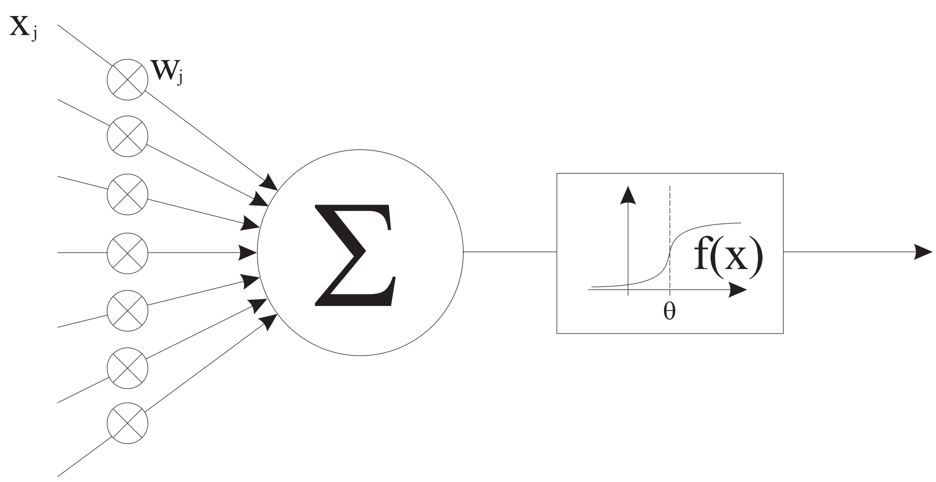

Figure 5.1: Schematic structure of a neuron.

In principle, neural networks can compute any *computable function* (i.e. they can do everything a digital computer does), under some assumptions. In practice, NNs are particularly useful for classification and function approximation/mapping problems which are tolerant of some imprecision, which have lots of training data available, but to which hard and fast rules cannot be applied easily. Almost any finite-dimensional vector function on a compact set can be approximated by a NN to arbitrary precision if enough data and enough computing resources are available.

Practical applications of NNs most often employ *supervised learning*. In supervised learning, training data are provided that include both the input and the desired result (the *target value*). After successful training, input data alone are presented to the NN (that is, input data without the desired result), and the NN will compute an output value that approximates the desired result. However, for training to be successful, lots of training data and lots of computer time for the training are often required. This topic will be best covered in Sec. 5.2.

Neural nets without supervised learning are not provided with target values during training. Unsupervised NNs are used to recognize regularities (a task which is present also in supervised nets, but usually considered secondary or auxiliary with respect to the classification, fitting or forecasting task for which the network is designed) and are usually employed for data compression, such as dimensionality reduction or clustering.

Neural networks can have any topology suitable to the problem to which they are tailored (bi- or three-dimensional, layered or unlayered, and so on). The two major kinds of network topology are *feedforward* and *feedback* nets. In a feedforward NN, the connections between units do not form cycles, while in a feedback or recurrent NN there are cycles in the connections. In some feedback NNs, each time an input is presented, the NN must iterate for a potentially long time before it produces a response, while feedforward NNs usually produce a response to an input quickly. Feedback NNs are usually more difficult to train than feedforward NNs. The topology chosen for this analysis is a subcategory of the feedforward networks, namely the Multi-Layer Perceptron (MLP). MLPs are the logical extension of the "Perceptron", i.e. the simplest possible neural network topology: a single neuron which combines several inputs to obtain its output. MLP's structure consists of one "input layer", made of neurons having one single input each from the environment, one "output layer" whose neurons communicate their outputs to the user, and one or more "hidden layers" whose neurons have as input the outputs of all the neurons of the preceding layer and give their outputs as inputs of the following layer. No "horizontal" (i.e. between neurons of the same layer) communication is allowed. A scheme of a typical MLP is shown in Fig. 5.2.

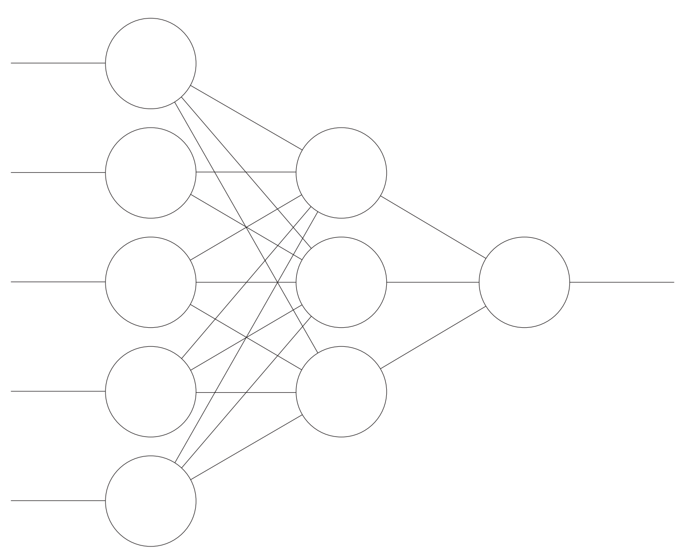

Figure 5.2: Typical architecture of a Multi-Layer Perceptron with a single hidden layer.

5.2 Supervised learning

In supervised training both the inputs and the desired outputs (*target values*) are provided. To start this process the initial weights are chosen randomly; then the network processes the inputs and compares its resulting outputs against the desired outputs. An "error" is defined, as the "distance" (in some metric) between the NN output and the target value. Typical error definitions are functions of $|O_i - T_i|$ (where O_i is output of the net for the i-th event, and T_i is the corresponding target value). Errors are then propagated back through the system, causing the system to adjust the weights which control the network, with the aim of minimizing the expected error at the next iteration. This process occurs over and over as the weights are continually tweaked. The set of data which enables the training is called the *"training sample"*. During the training of a network the same set of data is processed many times as the connection weights are ever refined.

It is important to have a second data set, the *"test sample"*, to which apply the neural network during the training phase to test its performance, with a given set of weights, on events that have not been used to adjust those weights. This is of great importance since a neural network is completely useless if it is not able to generalize. For example, if the training has gone too far the weights can be optimally adapted to the data set used to learn but the network can have poor performance on any other analogous data set; this is called *"over-learning"* (or *"over-fitting"*) and is usually avoided choosing a statistical criterion to stop the learning based on the performances on the test set, instead of the training set.

In "batch learning", in every learning cycle (or "epoch") the total error is summed over all the events in the training set and is the quantity to minimize; in "incremental learning", instead, the NN weights are updated after every single event.

Apart from the learning algorithm, supervised training methods can be classified in two subvarieties: auto-associative and hetero-associative. In auto-associative learning, the output variables are the same as the inputs, whereas in hetero-associative learning, the outputs are generally different from the inputs. For example, in most forecast problems one tries to predict the future values of some variables according to their history; in this case auto-associative learning is appropriate. An example of a problem in which hetero-associative training is used is the fitting of a function $y = f(x)$: if a data set of N values for the x variable is given, being f known, in every training cycle the network computes a single value as its best guess for y; this is compared with the target value $y_{true} = f(x)$, and the distance $y_{guess} - y_{true}$ is used to decide the adjustment of the synaptic weights.

A less trivial problem, in which neural nets are particularly useful, is the case in which the function f is completely unknown, but both x and the corresponding y are available as an experimental data set; the network, trained with N pairs (x_i, y_i), $i = 1, ..., N$, can "generalize", i.e. make a fair guess of the value y_{N+1} corresponding to x_{N+1}. An interesting feature of neural networks is that under certain assumptions they can approximate with arbitrary accuracy any continuous function. The method, of course, usually gives fairly good results even for quasi-continuous curves: the result will be an approximation of a continuous curve that approximates the discontinuous one.

Classification problems, when events have to be classified in one of two mutually exclusive categories, can be viewed as the fitting of a function having value *1* for one category (the "signal") and *0* for its complementary ensemble (the "background"). When N categories have to be recognized, it is customary to build neural networks with $N - 1$ outputs in order to map the categories in different regions of the $(N-1)$-dimensional space of the outputs. For example, to classify three categories of events A, B, C it is possible to assign target values $(0, 0)$ to A events, $(0, 1)$ to B events, and $(1, 1)$ to C events; after training, the A events should gather in the proximity of the point $(0, 0)$, and so on.

In classification problems, events of all the categories (which in this thesis are the signal, i.e. the $g \to c\bar{c}$ events, and the background consisting of all the other events) have to be shown to the net. Training a net with signal events only, for example, would yield a net which recognizes them with very high probability of success, but is completely unable to reject the background. A careful balance of the number of events for every category in the training sample is needed, to reach a fair separation between the different categories and so an optimal balance between high efficiency (i.e. low percentage of false negatives) and high purity (i.e. low percentage of false positives).

5.3 Training algorithms

The error (summed over the data set, or concerning a single event) is considered as a function of the synaptic weights of all the neurons, so that the learning process is essentially a minimization problem in the space of the weights. To perform this minimization several algorithms are available. Some of the most popular belong to the family of the "backpropagation algorithms", and are modified versions of the so called "standard backpropagation" [79].

"Standard backpropagation" is an application to the NNs of the *generalized delta rule*, also called the "heavy ball method" in the numerical analysis literature [80]: the variation of the weight for the link (synapsis) between unit j and unit i (with i being in the layer forward, in the net, with respect to j) is:

$$\Delta w_{ij} = \eta \delta_i o_j \tag{5.1}$$

where η is the "learning rate" (which is fixed in the standard backpropagation, but not in most of its variants), o_j is an output of the unit j (which is an input to i), and δ_i is a function of the outputs of the preceding layer's neurons which is calculated slightly differently for output and hidden units. For output units, under the assumption of a sigmoid[1] activation function, it is

$$\delta_i = o_i(1 - o_i)E_i \tag{5.2}$$

(where E_i is the error, as said above, calculated according to some distance definition), and for hidden units

$$\delta_i = o_i(1 - o_i) \sum_k \delta_k w_{ki} \tag{5.3}$$

In other words, the learning cycle in a backpropagation network involves the repetitive simultaneous presentation of matching input and output patterns while the weights are adjusted using a *gradient descent* search, i.e. the minimum is looked for by calculating the direction and magnitude of the gradient of the "error surface" in the space of the weights, $\frac{\partial E}{\partial w_{ij}}$. Thus a neural network can also be viewed as a non-linear numerical optimization procedure. Backpropagation can be used for both batch training (in which the weights are updated after processing the entire training set) and incremental training (in which the weights are updated after processing each case). For batch training, standard backpropagation usually converges to a local minimum, if one exists. For incremental training, standard backpropagation does not converge to a stationary point of the error surface. To obtain convergence, the learning rate must be slowly reduced, so that η in

[1]Best known to physicists as the Fermi-function: $f(x) = \frac{1}{1+e^{-x}}$. This function is approximately linear around $x = 0$ and reaches 0 or 1 asymptotically for large negative or large positive values of the argument, respectively. Due to this fact it is not possible for a single neuron to have an excessively large influence.

Eq. 5.1 is not constant anymore. This methodology is called "stochastic approximation" or "annealing".

Other variants are designed to avoid as much as possible to be trapped in a small local minimum failing to reach the absolute minimum. For example, a *momentum term* can be added in order to accelerate convergence when large plateaus of the error surface are present. At the n-th epoch the weights are updated as follows:

$$w_{ij}(n+1) = w_{ij}(n) + \Delta w_{ij}(n) + \alpha \Delta w_{ij}(n-1) \tag{5.4}$$

where Δw_{ij} is the variation defined in Eq. 5.1, and $0 < \alpha < 1$ (typically $\alpha \approx 0.9$) is the momentum term, whose effect is to impart enough "momentum" to "roll" quickly over the plateau.

In this thesis the Resilient Propagation algorithm, or RPROP [81], one of the most popular variants of the Standard Backpropagation, has been used as training algorithm. In contrast to other gradient descent algorithms, RPROP does not use the magnitude of the gradient $\frac{\partial E}{\partial w_{ij}}$, but only its direction. It begins with an initial small update value, and then increases this value if the current gradient points towards the same direction as the previous gradient, but decreases it if the gradient has the opposite direction. This update value is then added to the weight, if the gradient points towards the minimum, and subtracted from the weight in the opposite case.

5.4 Optimal number of layers in a Multi-Layer Perceptrons

No general rule exists about the optimal number of units per (hidden) layer in a MLP for a given problem [77], so that it is customary to proceed by trial and error: beginning with only one unit per layer, the number of units is increased until the performance of the network ceases to improve. When the number of units is too large, the number of connections, and consequently the number of weights to variate, makes the training very slow and a larger training sample becomes necessary to avoid over-fitting.

Instead, some considerations can be made about the number of layers needed to properly treat a problem, according to its complexity. These extra layers are needed to take into account the nonlinearities of the function to approximate (see Ref. [75, 76]). Consider Fig. 5.3a, which shows a classification problem with two input variables: it is possible to find a single hyper-plane (in the bidimensional case a straight line) separating class "A" from class "B". The task of finding this hyper-plane is called a "linearly separable problem". This problem can be solved by a MLP with no hidden layer (a Perceptron), which essentially performs a *linear regression* [82]. After proper training with a target function which takes on 0 for "A" events and 1 for "B" events, the output of the NN will be close to 0 on the "A" side, to 1 on the other side, and will have intermediate values in the proximity of the separating line. Even if the separation hyper-surface (called *decision surface*) to learn is mildly nonlinear, a better generalization can be obtained with a simple Perceptron than with a multilayered net if there is too little data or too much noise to estimate the nonlinearities accurately.

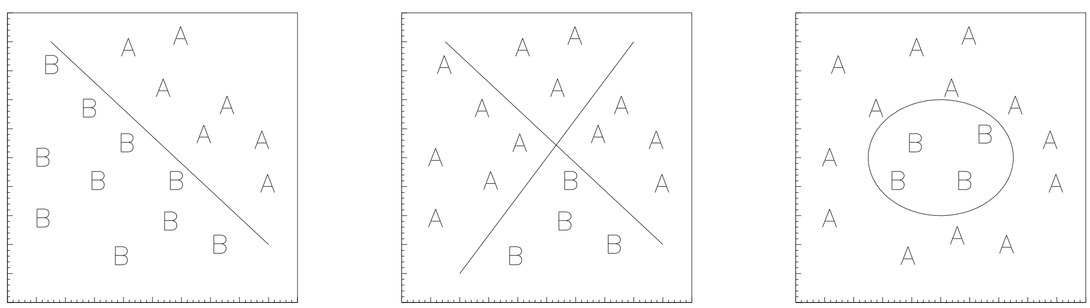

(a) (b) (c)

Figure 5.3: (a) Linearly separable problem, (b) non-linearly separable problem, (c) non-linearly separable problem with a closed contour.

Fig. 5.3b shows an example of "non-linearly separable problem": no straight line can properly separate the two categories of events. The introduction of a hidden layer overcomes the problem [83]. Intuitively, dividing the neurons in the hidden layer in two independent sub-groups, each one can be used by the net to find a straight line which confines all of the "B" events on one side, even if this means to have also a lot of "A" events on the same side. Working independently, the two groups will find, in general, different lines which obtain the same result in different ways; the neuron on the output layer can then make use of both the results. Other decision surfaces having more complex shapes can need more sub-groups, and so more units in the hidden layers, to be approximated. Problems with higher complexity (like the closed contour in Fig. 5.3c) can be better approximated with the help of a second hidden layer [84]. More than two hidden layers are shown to be unnecessary [77].

Chapter 6

Description of the analysis

6.1 Method

This analysis is based on a lepton tag. The advantage of this strategy over the D^* reconstruction (see Sec. 2.3.1) is in the higher efficiency of signal selection, at the cost of lower signal purity in the selected sample. Strategies based on event shape variables only, like the analysis by L3 [50] (shortly described in Sec. 2.3.3), suffer from very poor discriminating power, so that even higher efficiency can be reached but with very poor sample purity, and the high backgrounds yield very large systematic uncertainties which spoil the reliability of the result.

A selection is made on the full LEP I data set ($\approx$ 4 millions $e^+e^- \rightarrow Z^0 \rightarrow q\bar{q}$ events) from which only events with a lepton in the jet of smallest momentum are retained. The principle is that the jet which contains most of the final products of the process $g \rightarrow c\bar{c}$ is expected to be the one with the smallest momentum, since the gluon retains only a fraction of the momentum of the quark from which is emitted.

An important selection criterion is obtained by cutting on the thrust of the event (see Section 6.4), since a signal event is expected to be more spherical than a typical $Z^0 \rightarrow q\bar{q}$ event.

Further signal/background discrimination is reached by means of a neural network combining lepton properties and event topology variables.

6.2 Hadronic events in ALEPH

The standard selection of hadronic events in ALEPH makes use of the charged tracks information only.

At least five "good" tracks have to be reconstructed by the TPC for the event to be considered hadronic. This requirement rejects almost all the leptonic events and most of the $\gamma\gamma \to q\bar{q}$ events, i.e. events in which both the electron and the positron radiate photons whose interaction generate hadronic final products (Fig. 6.1).

A track is considered "good" if it fulfills the following requirements:

- At least four TPC coordinates are used in the track reconstruction.

- The track goes through a cylinder of radius 2 cm and length 10 cm surrounding the beam axis in the crossing point. This rejects spurious tracks and tracks not belonging to the event, e.g. those generated by cosmic rays or by interactions in the detector material.

- The angle between the track and the beam axis has to be larger than 18.2° ($|\cos\theta| < 0.95$), to ensure the crossing of at least six TPC rows of sense wires.

To further reject $\gamma\gamma$ background and interactions of the e^+e^- beams with gas molecules in the LEP beam pipe, a cut is applied to the sum of the energies of the charged tracks, which has to be larger than 10% of the centre-of-mass energy.

With all these requirements, the selection efficiency for hadronic events is 97.5%. The contamination of $\gamma\gamma$ and $Z^0 \to \tau^+\tau^-$ events is below 0.3%.

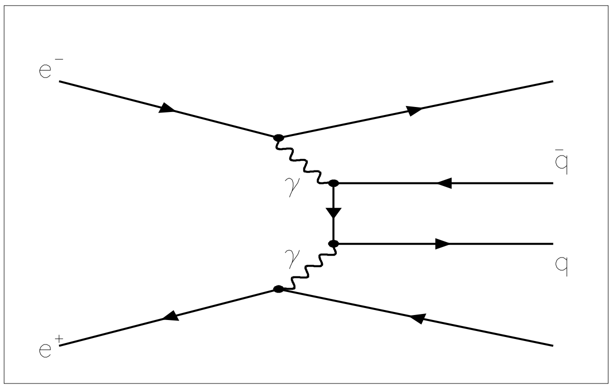

Figure 6.1: Lowest order Feynman diagram of a $\gamma\gamma \to q\bar{q}$ event.

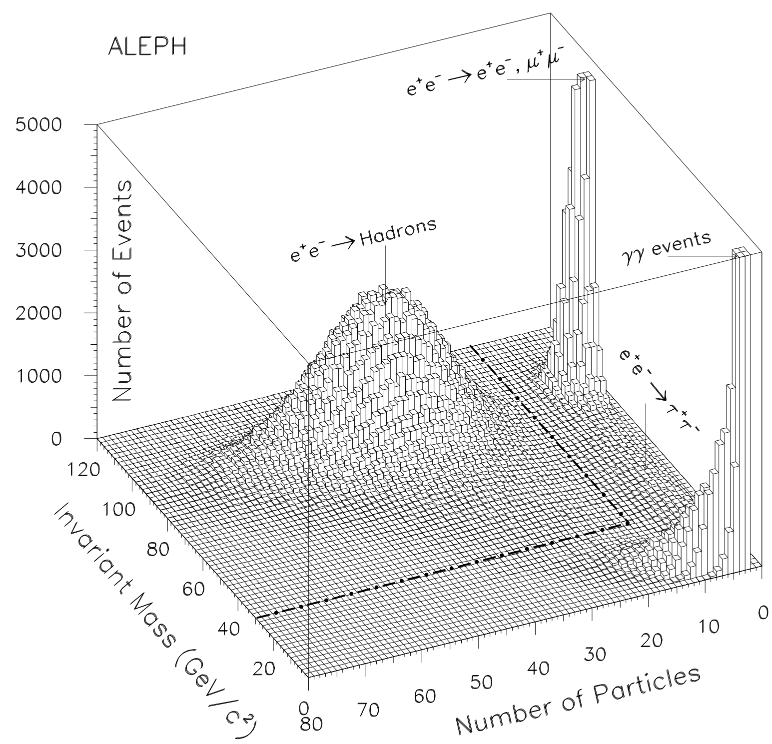

Figure 6.2: Number of particles and invariant mass for hadronic, leptonic and $\gamma\gamma$ events [56].

Figures 6.3 and 6.4 show a leptonic and hadronic Z^0 decay, respectively. In the first case only two charged tracks are reconstructed, while in the second case the charged multiplicity is very high. The average number of charged tracks in a hadronic event is 21.

The number of hadronic events found with this selection gives the denominator of the $g_{c\bar{c}}$ definition (Eq. 2.1). Afterwards, other cuts are needed in order to enrich the sample in signal events.

6.3 Event samples

The measurement is based on the LEP I data sample: about 3.9 million $Z^0 \rightarrow q\bar{q}$ decays collected by ALEPH from 1991 to 1995. The analysis makes also use of 8.7 million simulated $Z^0 \rightarrow q\bar{q}$ events, 5.1 million $Z^0 \rightarrow b\bar{b}$ events, 2.3 million $Z^0 \rightarrow c\bar{c}$ events, and 1.8 million signal events, generated specifically for this analysis, containing the $g \rightarrow c\bar{c}$ process. All the simulated events were generated using JETSET [20], and all events are passed through a detailed simulation of the detector based on GEANT 3 [66] (see Sec. 4.1.2). The $g_{c\bar{c}}$ and $g_{b\bar{b}}$ rates in the simulated samples were found to be too low with respect to

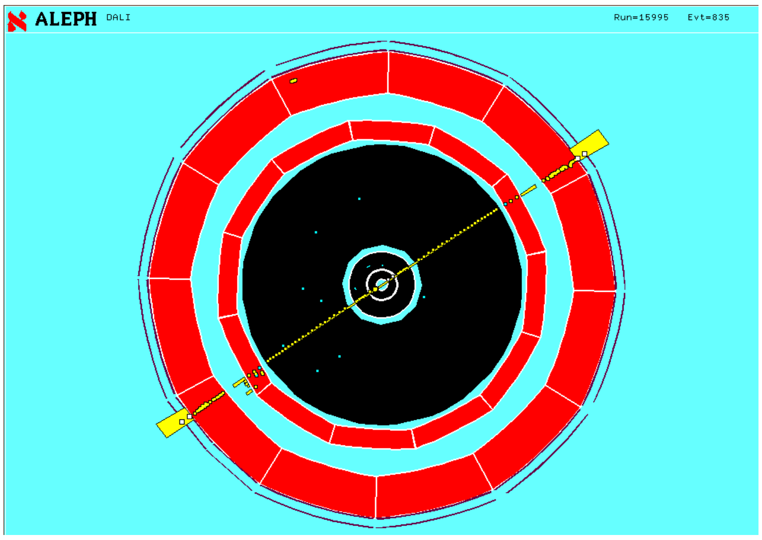

Figure 6.3: A $Z^0 \rightarrow \mu^+\mu^-$ event.

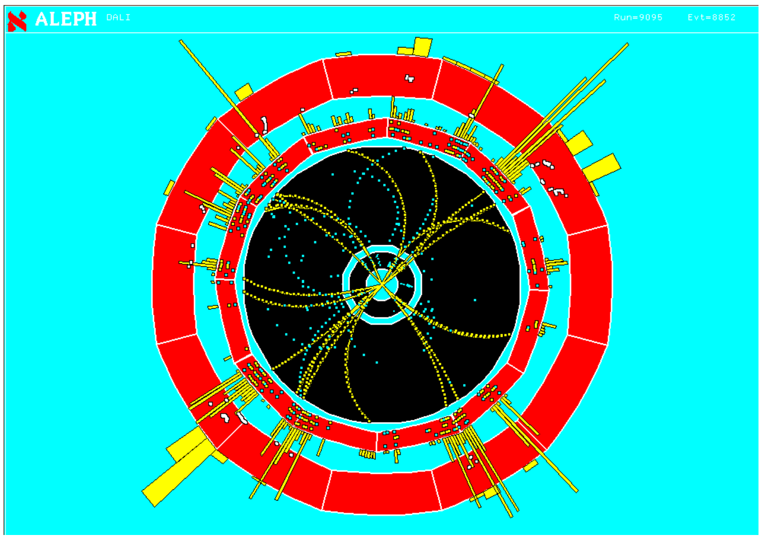

Figure 6.4: A hadronic Z^0 decay.

the measured values: $g_{c\bar{c}}^{MC} = 1.79 \times 10^{-2}$ and $g_{b\bar{b}}^{MC} = 1.69 \times 10^{-3}$ to be compared with the current world averages $g_{c\bar{c}}^{exp} = (2.96 \pm 0.38) \times 10^{-2}$ and $g_{b\bar{b}}^{exp} = (2.54 \pm 0.51) \times 10^{-3}$. This affects the distributions of the variables used in the analysis (see Sec. 6.6), so that the simulated events have to be reweighted in order to reproduce the experimental values of $g_{c\bar{c}}$ and $g_{b\bar{b}}$. For the same reason, a reweighting is performed on the following quantities, whose Monte Carlo value has been tuned to the experimental determination:

- semileptonic branching ratios in heavy quark decays ($BR(b \to l)$, $BR(b \to c \to l)$, $BR(c \to l)$);
- mean lifetimes of the B_d^0, B_S^0, $B^{\pm}$, Λ_b hadrons;
- $\langle x_E^{(b)} \rangle$ and $\langle x_E^{(c)} \rangle$ (assuming a Peterson distribution for $x_E \equiv p_{\text{had}}/E_{\text{beam}}$, see Sec. 4.1.1; the procedure is described in Sec. 7.1.4);
- lepton identification efficiency (see Sec. 4.7).

The composition of the $Z^0 \to q\bar{q}$ sample after reweighting is shown in Tab. 6.1.

$g \to c\bar{c}$	2.96 %
$g \to bb$	0.254 %
uds	58.8 %
c	16.5 %
b	21.4 %

Table 6.1: Composition of the total sample before any cut.

6.4 Preselection

The principle of the method is to look for leptons in the least energetic jet (after clusterization in three jets), since the "gluon jet", in signal events, is expected to be soft, and additional background-rejecting power is gained by means of a neural network.

First, events with a small value of thrust (defined in Sec. 1.5.2) are selected ($T < 0.94$), since this variable gives information on the topology of the event: a final state with two back-to-back particles has $T = 1$ by definition, while a three particle final state has $2/3 < T < 1$ (very close to 1 if two of the three are almost collinear, and 2/3 in the case of equal angles between the three directions), a four particle state $1/\sqrt{3} < T < 1$, and in general $1/2 < T < 1$ for any number of particles (close to 1 for two back-to-back very collimated jets, and close to 1/2 for an isotropic angular distribution in which no jet structure is recognizable).

Even after hadronization, final states originating from $Q\bar{Q}$ and $q\bar{q}$ can be discriminated by means of this variable. Fig. 6.5 shows the thrust distribution for data and simulated hadronic events, together with the distribution of signal events. The thrust cut < 0.94 is chosen in order to maximize the product "efficiency times purity" of the selection (see Fig. 6.6), where the efficiency is defined as the fraction of signal events passing the cut, and the purity as the fraction of the selected sample belonging to the signal class. The slight discrepancy between data and simulation is accounted for in the estimate of the systematic uncertainty (Sec. 7.1.3).

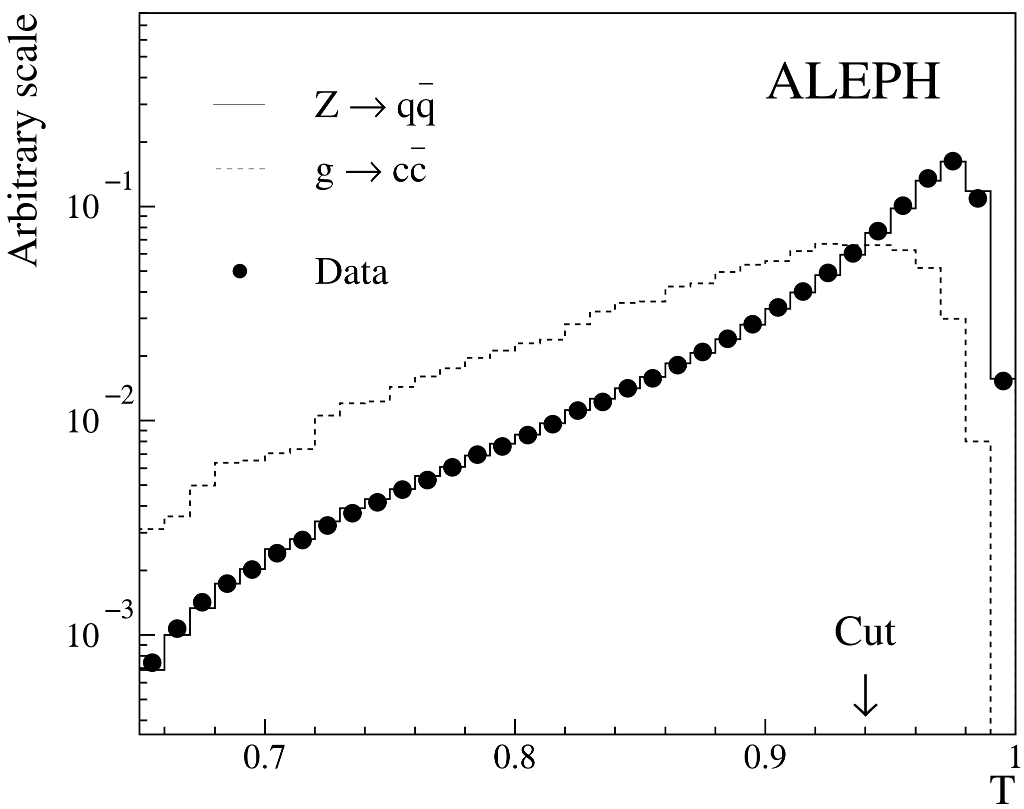

Figure 6.5: Thrust distributions for data and Monte Carlo (total and signal only) events, with arbitrary normalization.

In the events selected, particles are clustered in three jets, using a modification of the JADE algorithm [68] ("E scheme"), described in Sec. 4.5, which stops the clusterization

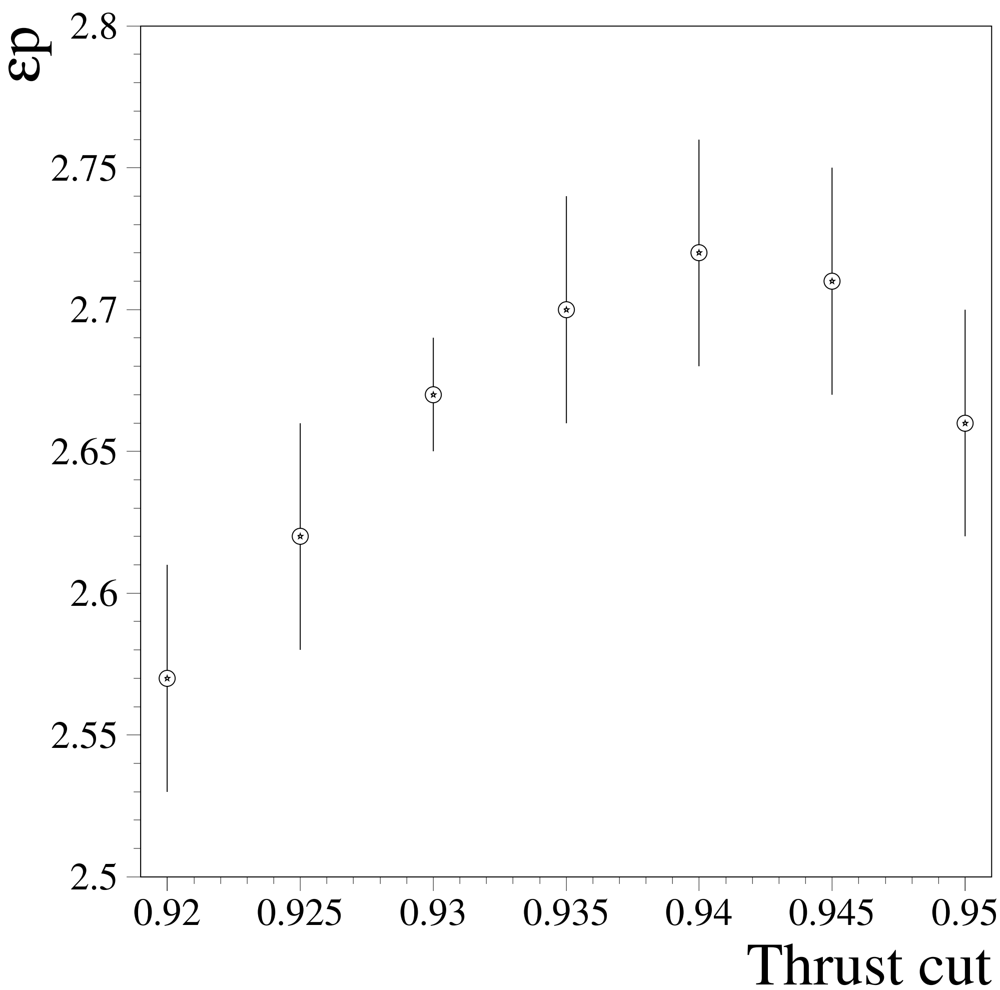

Figure 6.6: Efficiency times purity as a function of the thrust cut value.

when the desired number of jets is reached.

The momenta of the jets are calculated by enforcing energy-momentum conservation, under the assumption that jet directions are perfectly measured and that jets are massless, as

$$p_i = E_{cm} \frac{\sin \psi_{jk}}{\sin \psi_{jk} + \sin \psi_{ij} + \sin \psi_{ik}} \tag{6.1}$$

where E_{cm} is the centre-of-mass energy and ψ_{ij} is the angle between jets i and j. The jet momenta calculated in this way are used to order the three jets by decreasing momentum.

Any event, in ideal conditions (no initial state radiation, full detector acceptance, all the particles measured with infinite resolution), would have all three jets in a plane. Due to the limited acceptance and the finite resolution of the detector, and due to the impossibility of measuring the neutrinos (detected as "missing energy" or "missing momentum"), non-planar events are obtained. If the sum of the three angles is lower than 358°, the event is rejected (too far from coplanarity, Eq. 6.1 is no longer valid).

Leptons with missing or poor impact parameter information are not considered (candidates with no VDET hit are rejected), since the QIPBTAG routine (see Sec. 4.6) has an important role in this analysis, as will be shown in Sec. 6.5 and Sec. 6.6. Furthermore, the distance of closest approach of the lepton track to the beam axis (d_0) is required to be less than 0.1 cm, to better reject the leptons from K or π decays (Section 7.1.6).

This preselection yields 13363 events, out of which 5639 contain an electron candidate and 7724 a muon candidate.

The contaminations to the samples of muon and electron candidates are discussed in Sec. 4.7.2 and Sec. 4.7.4, respectively.

6.5 Background after the preselection

The flavour composition of the electron and muon subsamples evaluated with simulated events is shown in Table 6.2: the flavour content of the background is substantially different in the two cases. The larger fraction of light quark events for the muon subsample is related to the contamination of pions (punching through the calorimeters, and so being mistakenly recognized as prompt muons, or decaying in flight in $\mu\nu$), as discussed in Sec. 6.5.3.

Here a short description of the background categories is given, followed in Sec. 6.6 by the list of variables used in this analysis to discriminate them from the signal.

	e	μ
$g \to c\bar{c}$	17.0 ± 0.3 %	12.8 ± 0.3 %
$g \to bb$	3.4 ± 0.2 %	2.5 ± 0.1 %
uds	10.9 ± 0.3 %	27.7 ± 0.4 %
c	21.5 ± 0.4 %	20.0 ± 0.3 %
b	47.2 ± 0.4 %	37.0 ± 0.4 %

Table 6.2: Composition of the preselected sample.

6.5.1 Primary heavy quarks

By far the main background is given by the $Z^0 \to c\bar{c}$ and $Z^0 \to b\bar{b}$ events, as obvious due to the request of a prompt lepton in the event, which strongly reduces the *uds* component.

This kind of events are characterized by the presence of secondary vertices, like the signal, but more marked due to the larger momentum of the primary quarks with respect to the c's from gluon splitting, resulting in higher impact parameters for the decay leptons. So the b-tagging variables related to the QIPBTAG algorithm (see Sec. 4.6), typically used to discriminate between heavy and light quarks, can as well help to separate the signal from this background.

6.5.2 Gluon splitting in $b\bar{b}$

These events are topologically very similar to the signal events and for this reason the preselection yields an enrichment of this background.

Nevertheless, this is not particularly dangerous, due to the smallness of the contamination (before any selection, the signal events overwhelm this background by a factor of 10, and even after preselection there is still a factor of 5 between the two categories). The b-tagging variables used in this analysis give similar results for this category and for the primary heavy quarks events, so that in the following discussion the two categories will be grouped in one[1].

6.5.3 Light quarks

According to the Monte Carlo, about 56% of the muon candidates are coming directly from a heavy quark decay (*"prompt muons"*), 30% are coming from π or K decays, while 13% are hadrons which pass the standard identification criteria for prompt muons (see Table 4.4 in Sec. 4.7.4 for details). In the electron sample the contamination is significantly lower: 69% of the candidates are prompt electrons, and the main contamination (26%) comes from photon conversions in the detector material (see Table 4.3 in Sec. 4.7.2).

This contamination results in a corresponding contamination of *uds* events in the preselected sample, as shown in Tab. 6.2. This background is quite harmful, since the leptons coming from a $g \to c \to l$ chain are "softer" than leptons from primary charms,

[1] In Eq. 6.3 this background is treated as a category on its own, while the other two backgrounds are unified in only one category. This is done to make more evident the influence of the $g_{b\bar{b}}$ measured value on the determination of $g_{c\bar{c}}$.

so that their spectra resemble the ones from the fake and non-prompt components of the lepton samples.

6.6 Neural network inputs

The purity of the sample selected as in Sec. 6.4 is inadequate to perform a measurement of $g_{c\bar{c}}$ with interesting precision. Further separation between signal and background is provided by the variables described below; such variables are combined by means of a neural network into single discriminants N_e and N_μ, for the electron and the muon subsamples.

- the projection $P^3_{\rm miss} = \vec{P}_{\rm miss} \cdot \vec{n}_3$ of the missing momentum along the axis of the lowest momentum jet;
- the b-tag probabilities B_1 and B_2 of the two hemispheres divided by a plane perpendicular to the thrust axis (i.e. the confidence levels that the charged particle tracks of each hemisphere originate from the primary vertex);
- the thrust T of the event;
- the momentum P_l of the tagged lepton;
- the b-tag probability b_l of the tagged lepton in the third jet (i.e. the confidence level to originate from the primary vertex);
- the cosine $|\cos\theta_l|$ of the angle between the tagged lepton and the beam line.

In the following, the role of these variables is discussed, and the shapes of their distributions are shown for signal, uds and cb events (where the last category includes $g \to b\bar{b}$ events). A comparison between data and Monte Carlo events after the preselection cuts is shown for every variable, since the reliability of the net depends critically on the reliability of the simulation.

6.6.1 Missing momentum along the third jet

This variable has never been used before in gluon splitting measurements. The "missing momentum" vector is defined as $\vec{P}_{\rm miss} = -\sum_i \vec{P}_i$, where the index i runs on all the reconstructed particles (including photons and neutral hadrons). $P^3_{\rm miss}$ is the component of this vector parallel to the axis of the third jet.

In *uds* events the expectation value of $P^3_{\rm miss}$ is zero. The broadness of the distribution is due to the energy resolution of the "energy flow" algorithm (see Sec. 4.3), and to the presence of neutrinos from light hadron decays.

In heavy quark events, gluon splitting included, the missing momentum due to the neutrino from the semileptonic decay is mostly along the jet axis, so that this variable can help the neural net to perform a discrimination, as shown in Fig. 6.7a.

The $P^3_{\rm miss}$ distribution in data and simulation is shown in Fig. 6.7b.

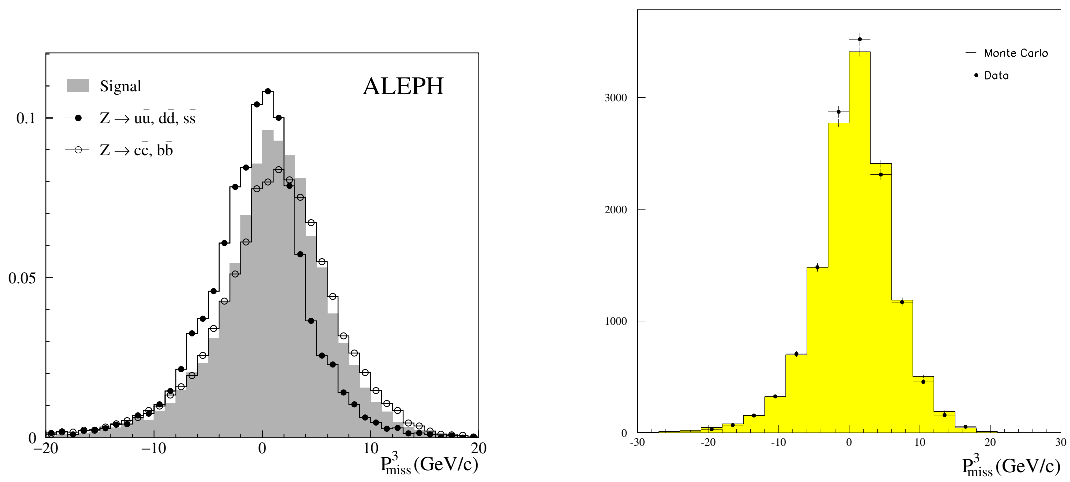

(a) (b)

Figure 6.7: Distribution of $P^3_{\rm miss}$, (a) for different event classes in Monte Carlo events (normalized to the same arbitrary area) and (b) in data and simulation (normalized to data).

6.6.2 B-tag probabilities of the two hemispheres

The combined QIPBTAG probability for hemispheres has been defined in Sec. 4.6. The two hemispheres are labeled according to their invariant mass: the first is the lightest, so that the second is the one with higher probability to contain the decay products of the c and $\bar{c}$ from gluon splitting in signal events. In both hemispheres the *uds* distribution is almost flat, as shown in Fig. 6.8a and Fig. 6.9a, while for heavy flavours it clearly decreases with B_1 and B_2. The signal distributions are less peaked at zero due to the smaller momentum of the charm quarks from the gluon, that results in smaller impact parameters of the decay products.

The B_1 and B_2 distributions in data and simulation are shown in Fig. 6.8b and Fig. 6.9b.

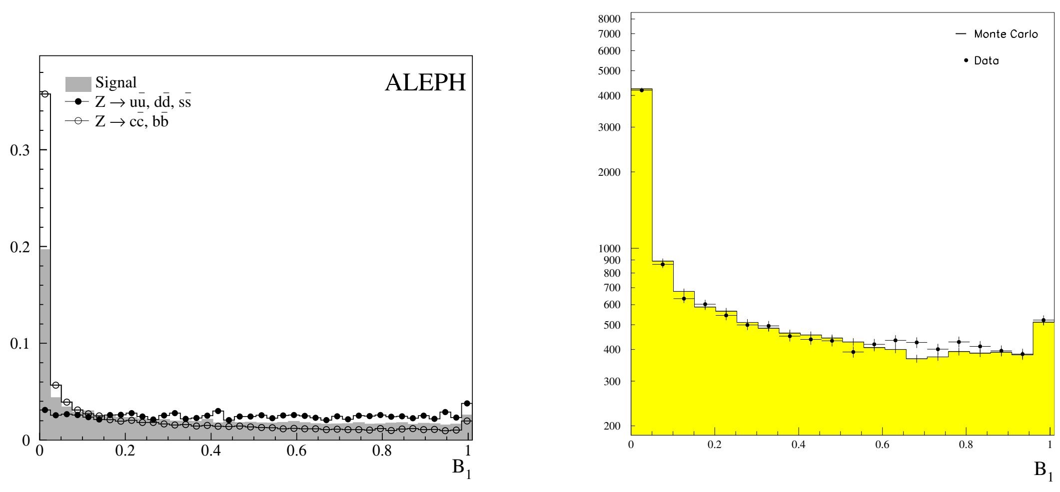

(a) (b)

Figure 6.8: Distribution of B_1, (a) for different event classes in Monte Carlo events (normalized to the same arbitrary area) and (b) in data and simulation (normalized to data).

6.6.3 Thrust

Thrust has already been discussed in Sec. 6.4 and a cut has been applied in the preselection; this variable is used again as an input for the neural network since the distributions of signal and background are significantly different also below the cut, as shown in Fig. 6.10a.

This is the only variable used in this analysis which discriminates both *uds* and *cb* events against the signal.

The T distribution in data and simulation after preselection is shown in Fig. 6.10b (to be compared to Fig. 6.5).

6.6.4 Lepton momentum

Lepton momentum is measured as described in Sec. 4.2).

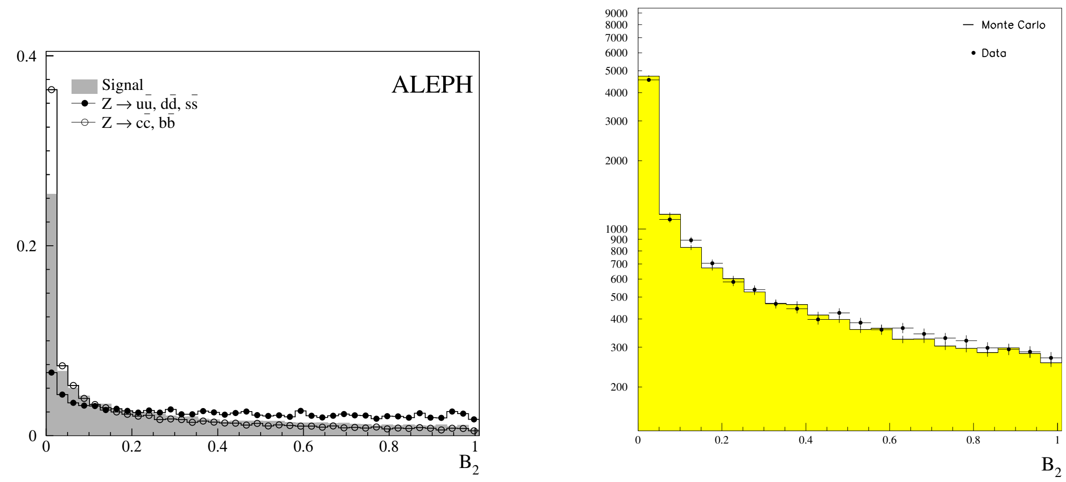

(a) (b)

Figure 6.9: Distribution of B_2, (a) for different event classes in Monte Carlo events (normalized to the same arbitrary area) and (b) in data and simulation (normalized to data).

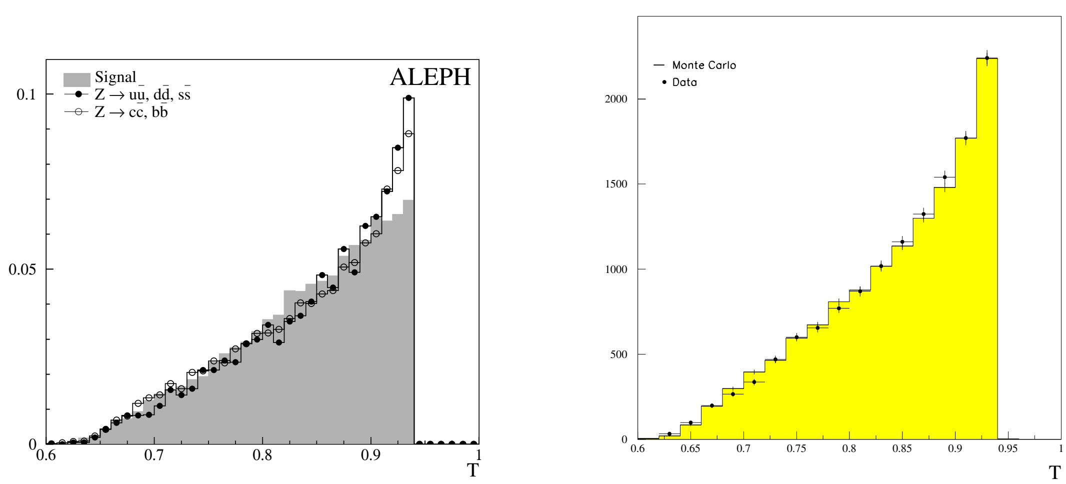

(a) (b)

Figure 6.10: Distribution of T, (a) for different event classes in Monte Carlo events (normalized to the same arbitrary area) and (b) in data and simulation (normalized to data)..

The momentum spectrum for prompt leptons is harder than for non-prompt or fake leptons, which give rise to the uds background. Nevertheless, signal events, due to the smaller energy, on average, of the charm quarks from gluon splitting, are harder to separate from *uds* events, as shown in Fig. 6.11a.

The P_l distribution in data and simulation is shown in Fig. 6.11b.

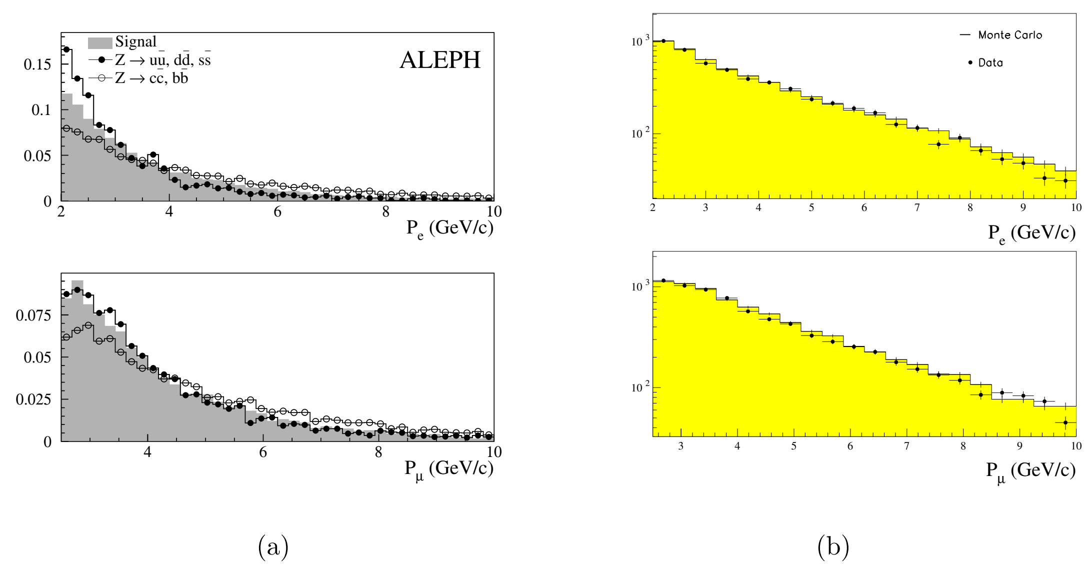

Figure 6.11: Distribution of P_e and P_μ, (a) for different event classes in Monte Carlo events (normalized to the same arbitrary area) and (b) in data and simulation (normalized to data).

6.6.5 B-tag probability of the lepton

This variable has already been described in Sec. 4.6. As already stated, the softness of the momentum spectrum of the leptons from the $g \to c \to l$ chain results in smaller impact parameters for leptons in signal events, and this explains why the signal distribution is intermediate between the two backgrounds in Fig. 6.12a.

The b_l distribution in data and simulation is shown in Fig. 6.12b.

6.6.6 Leptonic angular distribution

The cosine of the angle between the lepton track and the beam line is correlated with the quality of the lepton reconstruction, and therefore with the discriminating power of some of the variables described above.

Furthermore, this variable has a slight discriminating power between light and heavy quarks (independently of their origin from gluon or directly from Z^0), as shown in

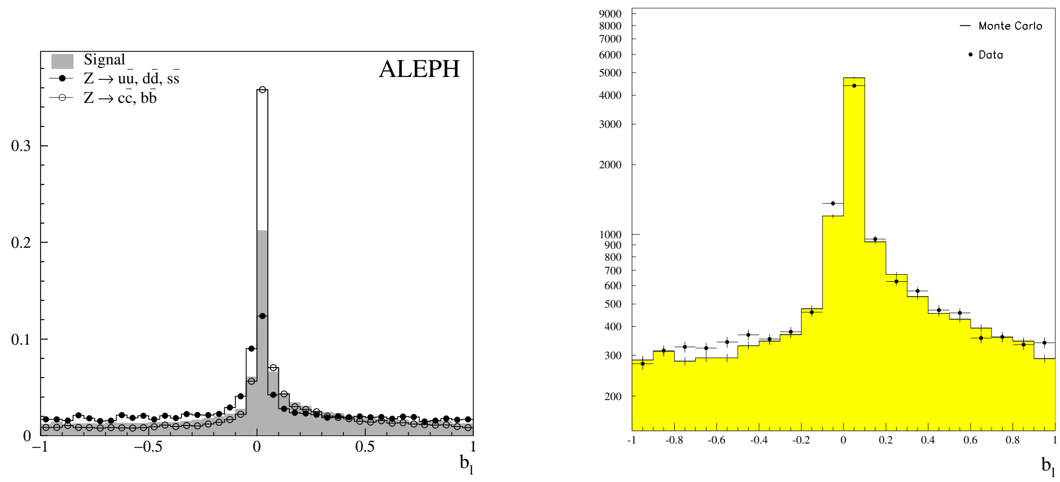

(a) (b)

Figure 6.12: Distribution of b_l ($l = e, \mu$), (a) for different event classes in Monte Carlo events (normalized to the same arbitrary area) and (b) in data and simulation (normalized to data).

Fig. 6.13a. The *uds* distribution is higher in the angular region corresponding to the transitions between barrel and end-caps of the calorimeters, where the lepton identification criteria are less reliable.

The $|\cos\theta_l|$ distribution in data and simulation is shown in Fig. 6.13b.

6.6.7 Other discriminant variables not used in this analysis

Two previous measurements [48, 50] made use of the mass of the least energetic jet in three jet events (with an optimized choice of the resolution parameter of the jets). In a generic $g \to Q\bar{Q}$ event (where Q is a heavy quark) this jet contains most of the remnants of the two Q's, so that its mass spectrum is harder than for background events. Its use in the present analysis, after preselection and clusterization in three jets, has been considered. Fig. 6.14 shows that this variable has a good discriminant power, but is poorly reproduced by the Monte Carlo simulation. This discourages from its use as an input in the neural network. A similar data / Monte Carlo discrepancy is observed, in the preselected sample, for the mass difference between hemispheres (this variable is used in Ref. [49]). This is not surprising, since there is a correlation between the mass (and thus the broadness) of the least energetic jet and the number of particles belonging to this jet assigned to the

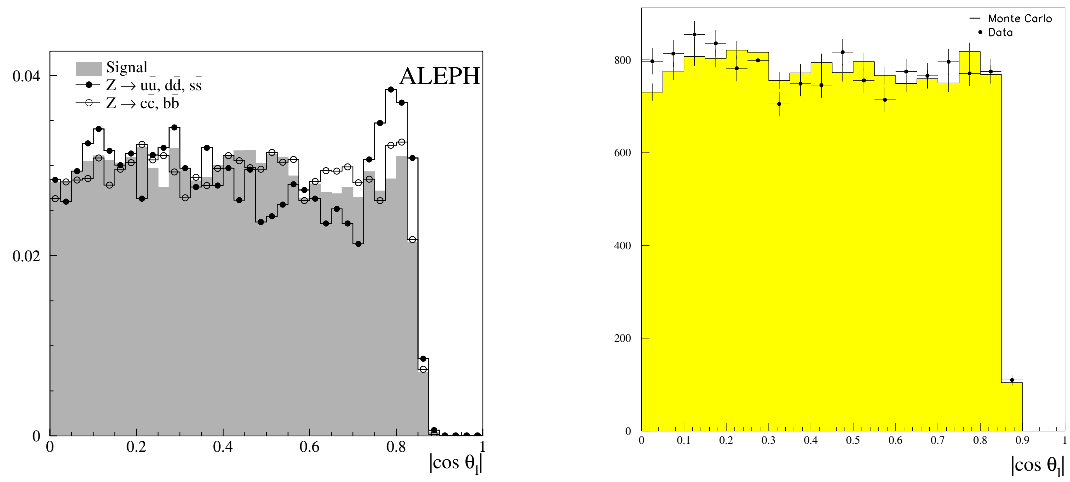

(a) (b)

Figure 6.13: Distribution of $|\cos\,\theta_l|$ ($l = e, \mu$), (a) for different event classes in Monte Carlo events (normalized to the same arbitrary area) and (b) in data and simulation (normalized to data).

"wrong" hemisphere.

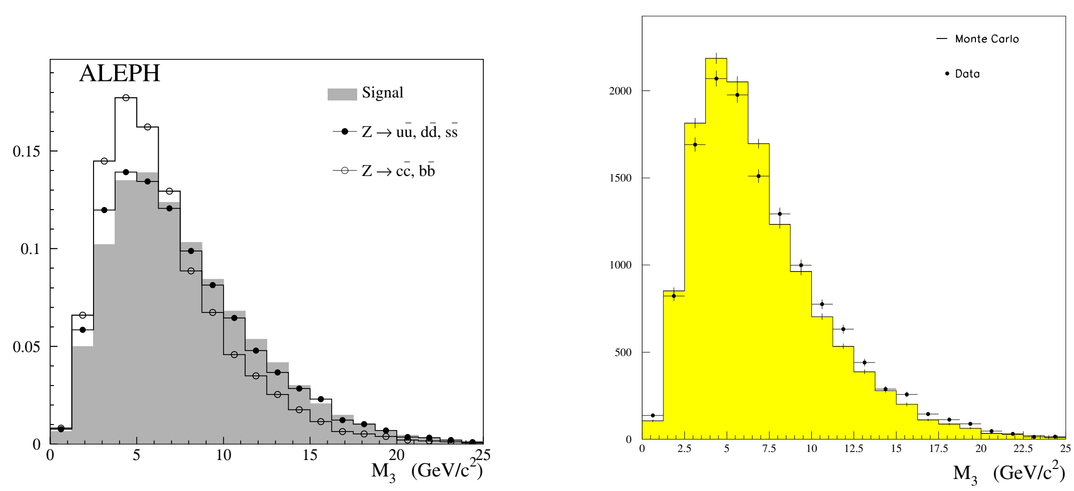

(a) (b)

Figure 6.14: Distribution of M_3, (a) for different event classes in Monte Carlo events (normalized to the same arbitrary area) and (b) in data and simulation (normalized to data).

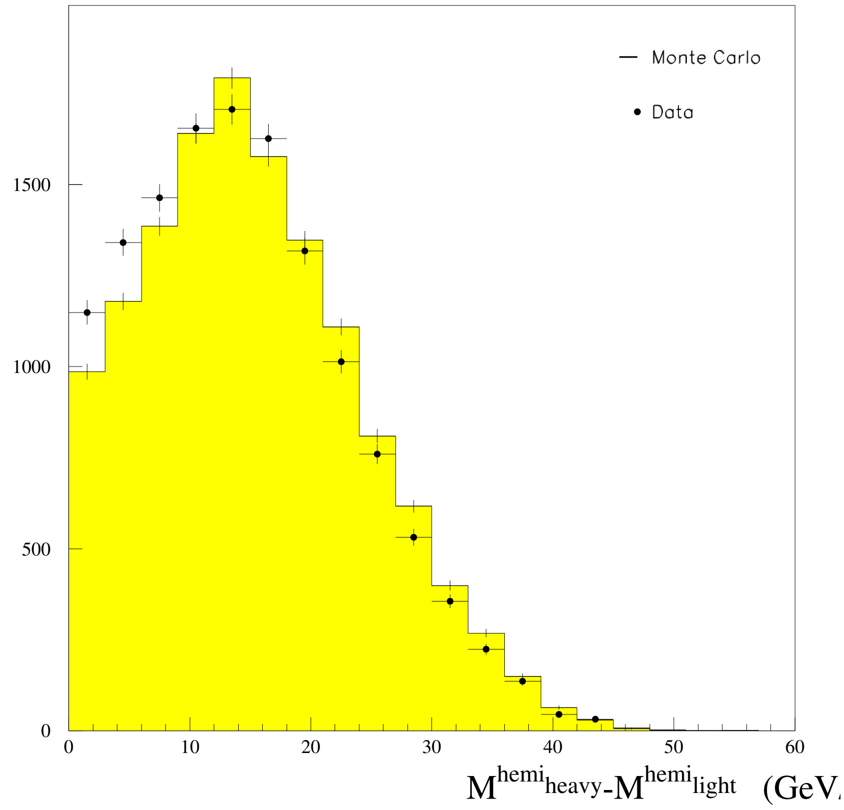

Figure 6.15: Distribution of $M_{heavy}^{hemi} - M_{light}^{hemi}$ in data and simulation (normalized to data).

A lot of effort was put in the search for the causes of this discrepancy (affecting to a lesser extent also the other two jets, as shown in Fig. 6.16). Among the first hypotheses considered was an incorrect simulation of the calorimetric response (affecting neutral objects reconstruction). This was ruled out from the observation that the discrepancy is present even when jets are constructed out of charged tracks only, as in Fig. 6.17.

Also the possibility of an incorrect simulation of the baryonic content of jets was considered, and to test this hypothesis the jet mass was computed assuming particle mass equal to the pion mass (139.5 MeV/c^2) for all the charged tracks, and null mass for all the neutral objects. This way the distribution is insensitive to the baryon/meson ratio in the jet, but Fig. 6.18 shows that the discrepancy is still present: both data and simulation average values for the jet masses are shifted by approximately the same amount (134 and 137 MeV/c^2 for M_3, respectively).

The possible connection between the discrepancy and the sample composition was

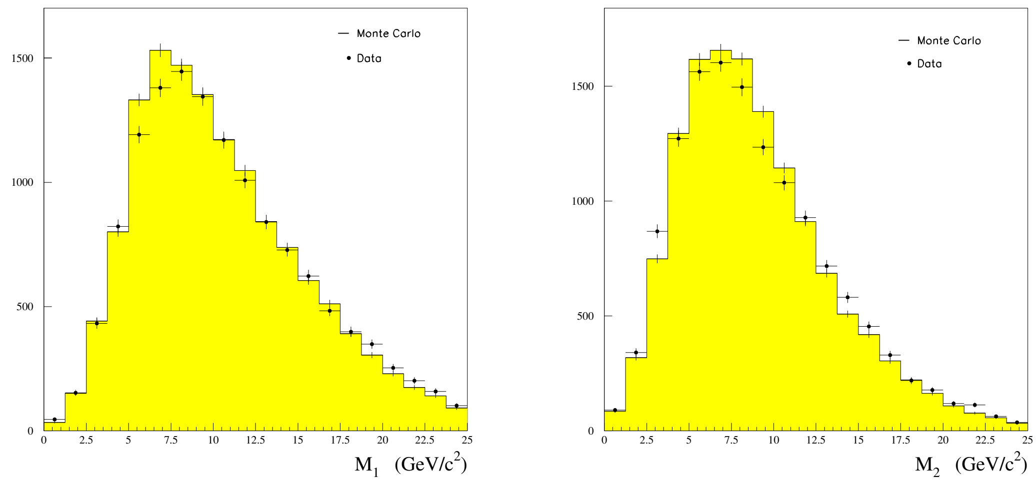

(a) (b)

Figure 6.16: Distribution of M_1 and M_2 in data and simulation (normalized to data).

checked by means of b-tags and uds-tags. Fig. 6.19 shows the presence of the discrepancy for two subsamples with very different composition, one enriched in heavy quarks (80% b, 6% uds) and the other in light quarks (33% b, 42% uds) by the application of a cut on the b-tag probability of the lightest hemisphere (see Sec. 6.6.2).

To find the source of the discrepancy, some cuts were removed or relaxed. For example Fig. 6.20, obtained removing the thrust cut, shows that the discrepancy is not related to the average sphericity of selected events. Instead, keeping the thrust cut but allowing the tagged lepton to be in any of the three jets, as in Fig. 6.21, the discrepancy disappears, demonstrating that the source of the problem is the attribution of the lepton to a jet, for high sphericity events. Some attempts were done to perform an analysis without the request of a lepton in the third jet, but none of these attempts managed to achieve the same signal purity.

6.7 Choice of the neural network topology and of the learning algorithms

The neural network used in this analysis was generated with the help of the SNNS program [78], a NN simulator which offers a large choice of network topologies and learning algorithms. The network chosen for this analysis is a feedforward network, more specifi-

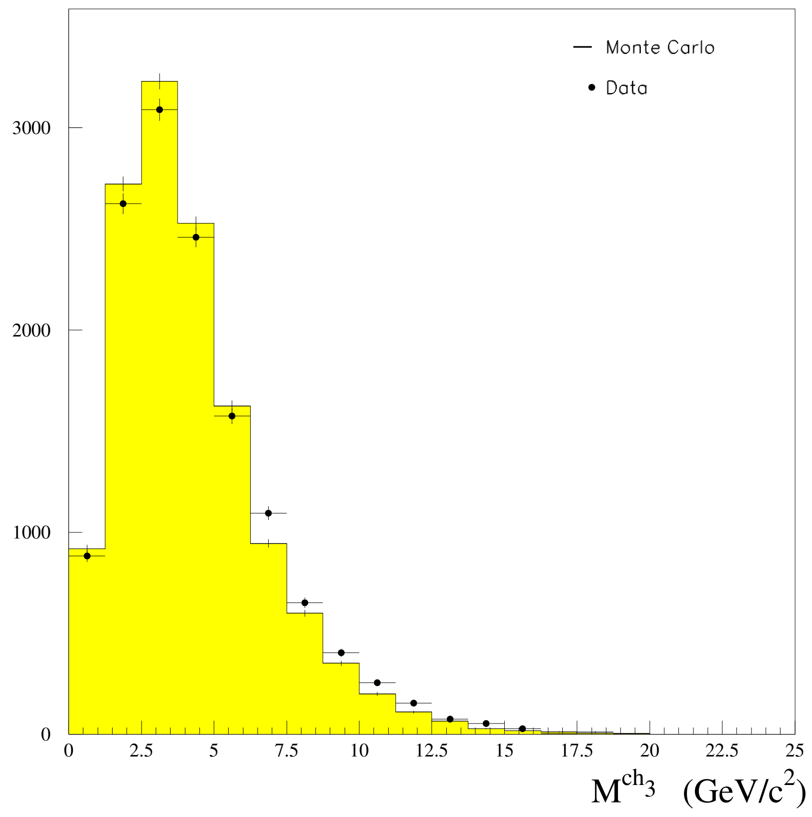

Figure 6.17: Distribution of M_3 in data and simulation (normalized to data) using only charged tracks.

cally a Multi-Layer Perceptron with two hidden layers (see Chapter 5).

The choice of the MLP topology is motivated by theoretical considerations about its performances in classification problems like the signal/background separation needed in this analysis.

Also the presence of two hidden layers is theoretically motivated, as explained in Sec. 5.4. Nevertheless, a comparison has been done between the performance of nets with one and two hidden layers, showing that, independently from the learning algorithm and the number of units per layer tried, for the specific problem of the $g \to c\bar{c}$ separation from the background almost the same discriminant power is obtained, but the number of cycles needed to reach it differs roughly by a factor of 10, in favor of the two hidden layers structure.

The choice of the number of units in both hidden layers, and of the training algorithm, has been based on trial and error, with the aim of optimizing the separation between signal

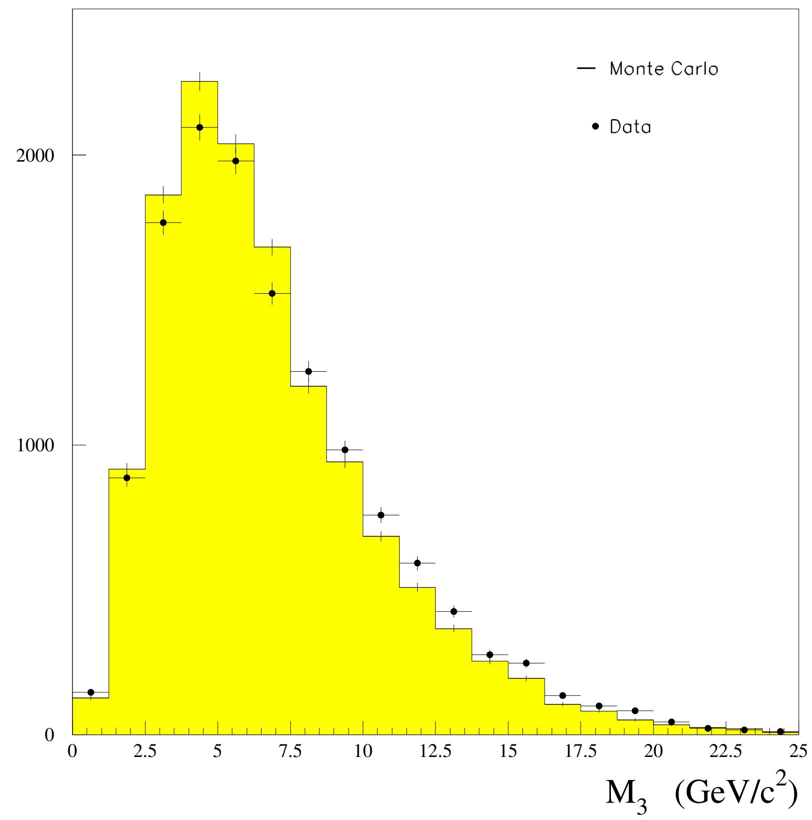

Figure 6.18: Distribution of M_3 in data and simulation (normalized to data) assuming $m_{ch} = m_\pi$ and $m_{neutr} = 0$.

and background. The best configuration was found to be seven units both in the first and the second hidden layer (equal to the number of input units), but with a fair tolerance to small variations (i.e., nets with six or eight units per hidden layer give essentially the same performance). For what concerns the training algorithms, the SNNS program provides quite a large variety of choices, but the trials have been restricted to the members of the backpropagation family (see Sec. 5.3), i.e. the “standard backpropagation” and several of its variants. It has been found that the majority of the variants reach the same minimum in the error surface, and so almost the same weight configuration, and in consequence the same discriminant power, but with different speeds. The Resilient Propagation algorithm or RPROP [81], described in Sec. 5.3, was found to be the fastest between the algorithms tested.

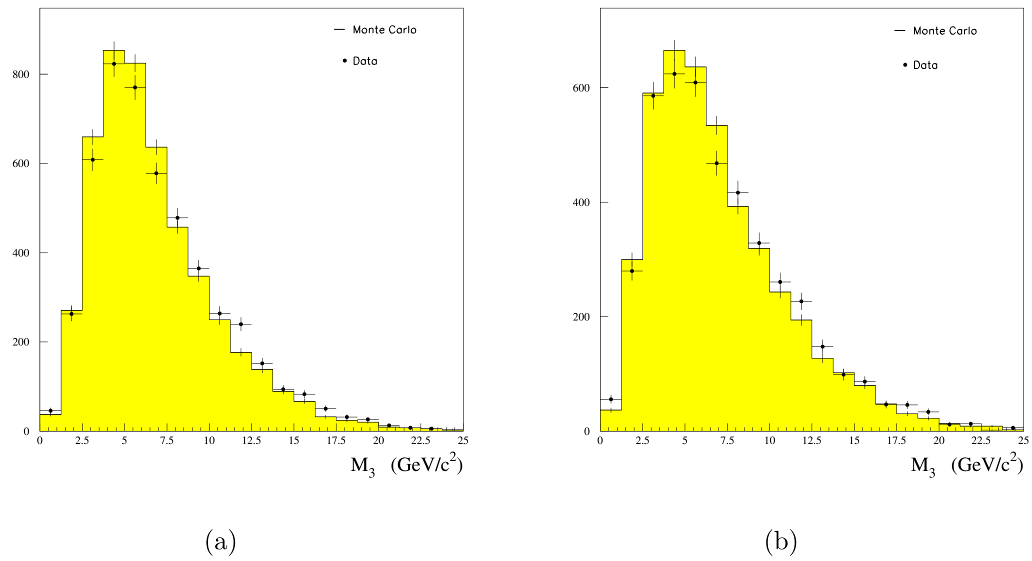

Figure 6.19: Distribution of M_3 in data and simulation (normalized to data) for subsamples enriched in (a) b quarks and (b) uds quarks.

6.8 The extraction of $g_{c\bar{c}}$

The neural network has been trained with half of the simulated $Z^0 \to q\bar{q}$ sample and half of the simulated signal sample. The remaining statistics, together with the $Z^0 \to b\bar{b}$ and $Z^0 \to c\bar{c}$ simulated sample, have been used to estimate the efficiencies of the selection.

The discriminating variable provided by the neural network is shown in Fig. 6.22, for the electron and muon subsamples. The separation between signal and background is worse for the muon subsample, due to the high contamination of non-prompt muons in the preselected sample. Figure 6.23 shows the agreement between data and simulation.

Cut	σ^e_{stat}	σ^e_{syst}	σ^e_{tot}	σ^μ_{stat}	σ^μ_{syst}	σ^μ_{tot}
0.30	0.26	0.54	0.80	0.33	0.80	1.13
0.35	0.26	0.52	0.78	0.34	0.77	1.11
0.40	0.26	0.51	0.77	0.36	0.75	1.10
0.45	0.27	0.48	0.75	0.38	0.72	1.10
0.50	0.27	0.45	0.72	0.45	0.65	1.10
0.55	0.28	0.42	0.70	0.58	0.62	1.20
0.60	0.29	0.41	0.70	0.88	0.73	1.61
0.65	0.32	0.39	0.71			

Table 6.3: Statistical, systematic and total uncertainties for different cuts on N_e and N_μ. The total error is taken as the ordinary sum of the statistical and systematic error.

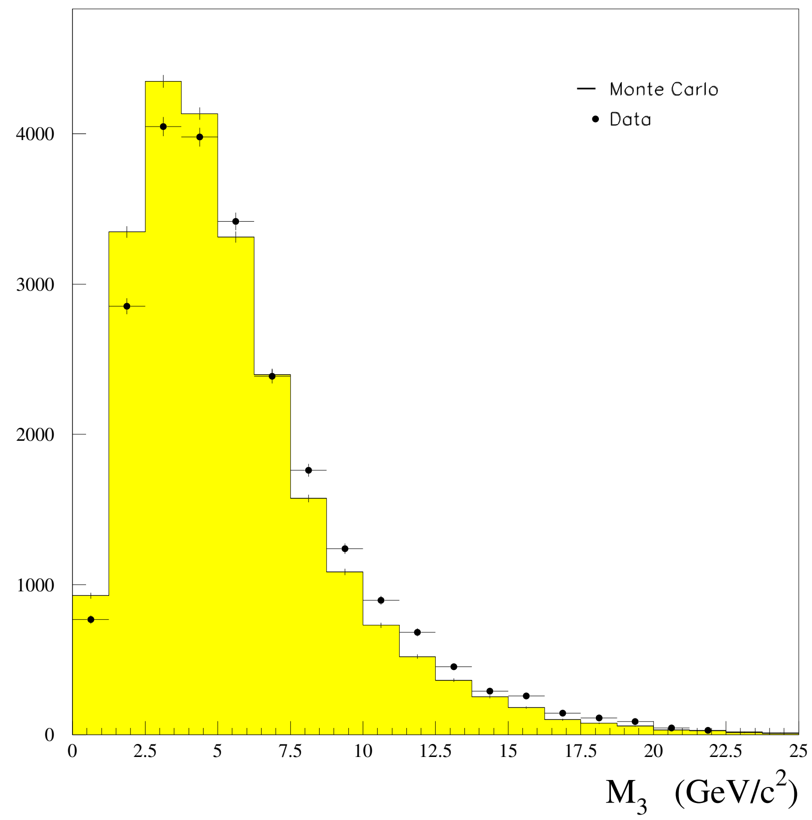

Figure 6.20: Distribution of M_3 in data and simulation (normalized to data) for a larger sample with no thrust cut.

The cut on the neural network output has been optimized separately for the electron and the muon subsamples, to minimize the total error: $N_e > 0.55$ and $N_\mu > 0.45$, respectively. The statistical, systematic (discussed in Sec. 7.1) and total uncertainties for different cut values are listed in Tab. 6.3 and shown in Fig. 6.24. The variation of the extracted $g_{c\bar{c}}$ value when choosing a different cut is shown in Sec. 7.2.1.

This final selection cut yields 2258 events containing an electron candidate and 3332 events containing a muon candidate, with the sample composition shown in Table 6.4 (estimated from the simulation).

The number of signal events N_S in the data sample can be written as

$$N_S = N_H \left[(1 - g_{c\bar{c}} - g_{b\bar{b}})\ \epsilon_Q + g_{c\bar{c}}\ \epsilon_C + g_{b\bar{b}}\ \epsilon_B \right] , \tag{6.2}$$

where N_H is the number of hadronic events selected as in 6.2 and ϵ_Q, ϵ_C, ϵ_B are the selection efficiencies for events with, respectively, no gluon splitting, gluon splitting in $c\bar{c}$,

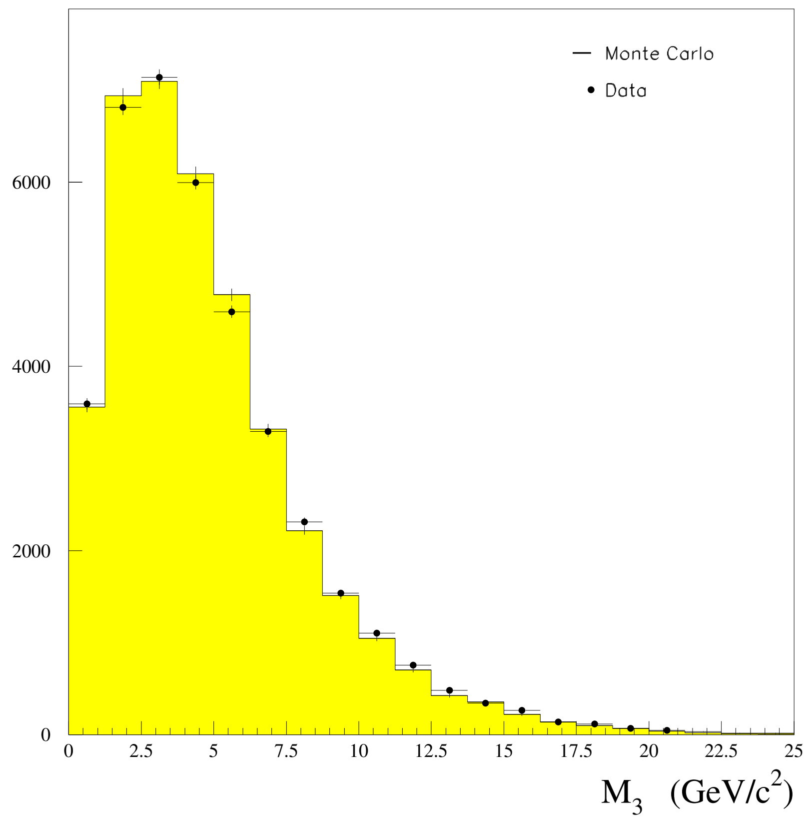

Figure 6.21: Distribution of M_3 in data and simulation (normalized to data) for a larger sample with the lepton allowed to be in any jet.

	e	μ
$g \to c\bar{c}$	25 %	18 %
$g \to bb$	4 %	2 %
uds	18 %	35 %
c	28 %	22 %
b	25 %	23 %

Table 6.4: Composition of the selected sample, after the cut on the neural network output.

and gluon splitting in $b\bar{b}$ (Table 6.8). From this equation the value of the gluon splitting rate is extracted as

$$g_{c\bar{c}} = \frac{f \ - \ (1 - g_{b\bar{b}})\ \epsilon_Q \ - \ g_{b\bar{b}}\ \epsilon_B}{\epsilon_C \ - \ \epsilon_Q} \ , \qquad (6.3)$$

where $f \equiv \frac{N_S}{N_H}$.

In the calculation of $g_{c\bar{c}}$, $g_{b\bar{b}}$ is fixed to the latest world average value $(2.54 \pm 0.51) \times 10^{-3}$ [52]. The results extracted from the two subsamples are $g^e_{c\bar{c}} = (3.32 \pm 0.28) \times 10^{-2}$ and $g^\mu_{c\bar{c}} = (2.99 \pm 0.38) \times 10^{-2}$,

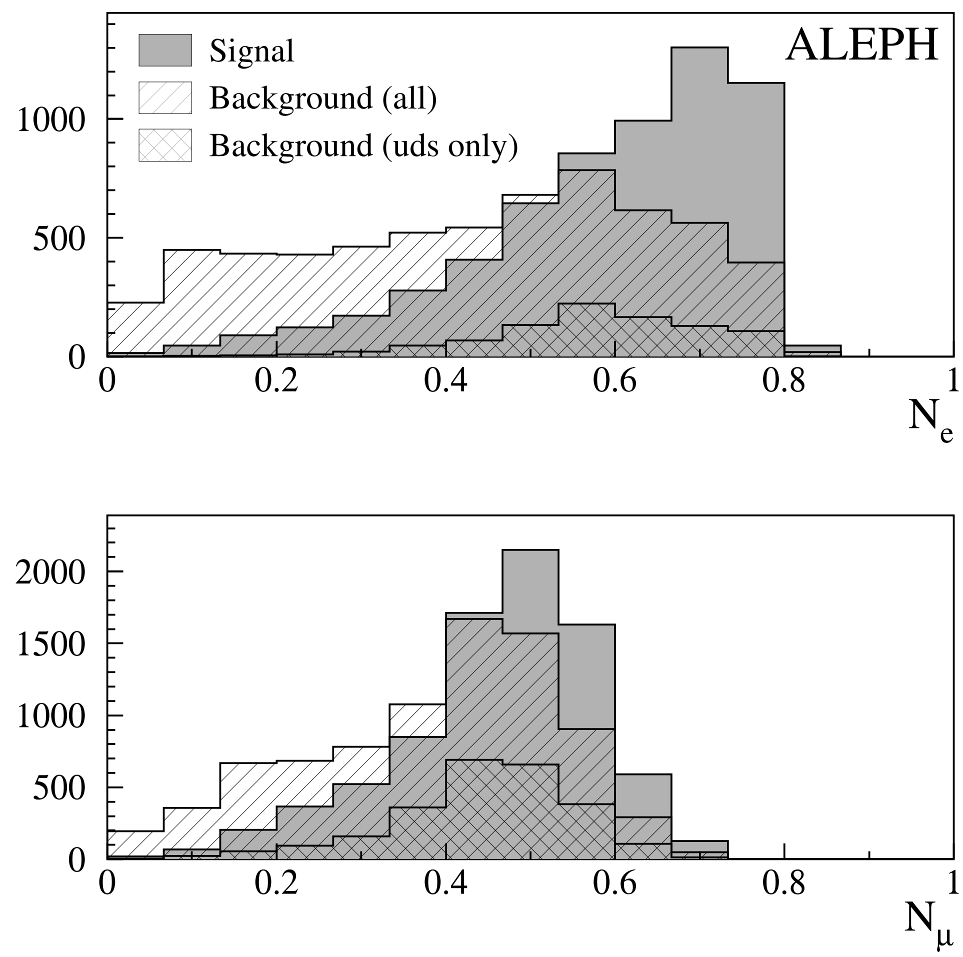

Figure 6.22: Output of the neural network for (a) electrons and (b) muons. (The signal area is normalized to the same area as the total background).

where the errors account for the statistical uncertainty on f only.

	electrons (%)	muons (%)
f	0.0600 ± 0.0013	0.0885 ± 0.0015
ϵ_Q	0.0431 ± 0.0006	0.0747 ± 0.0009
ϵ_C	0.491 ± 0.005	0.473 ± 0.005
ϵ_B	0.81 ± 0.06	0.80 ± 0.06

Table 6.5: Fraction of events selected and selection efficiencies for the different event categories.

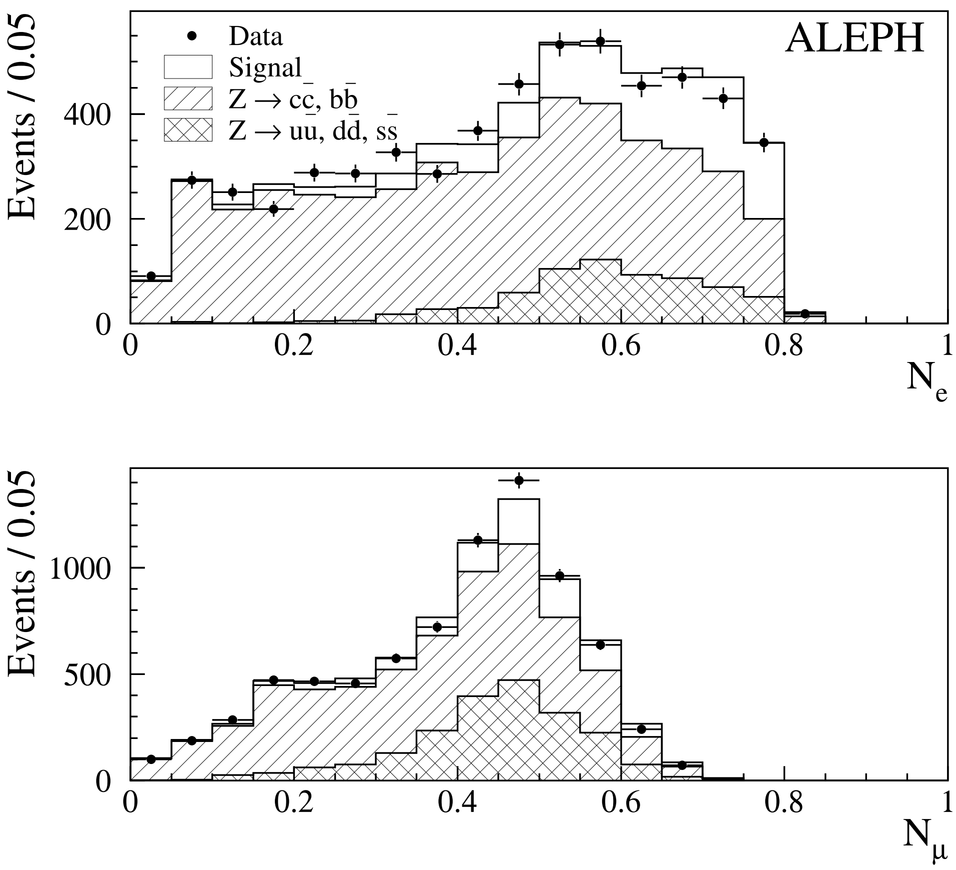

Figure 6.23: Output distribution of the neural network in data and simulation (normalized to the same area) for electrons and muons.

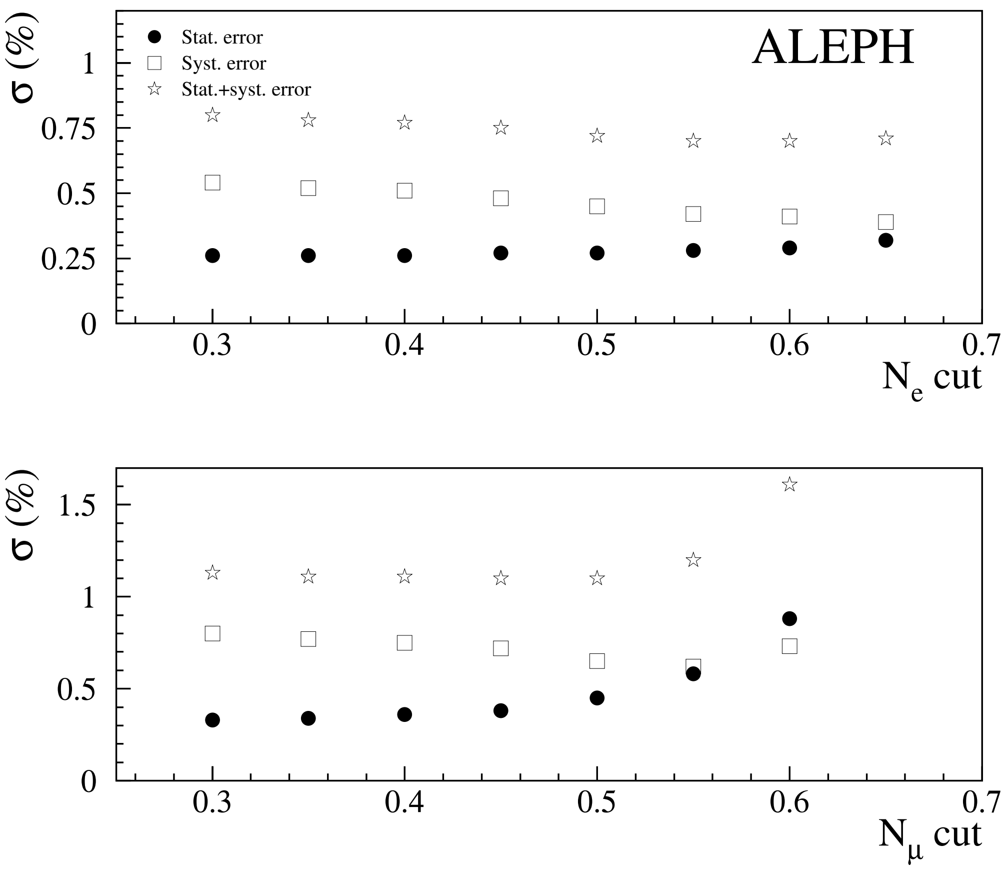

Figure 6.24: Statistical, systematic and total uncertainties for different cuts on N_e and N_μ. The total error is taken as the ordinary sum of the statistical and systematic error.

Chapter 7

Systematic errors and consistency checks

7.1 Sources of systematic error

Systematic uncertainties can arise from imperfections of the simulation of the physics processes, from the uncertainties in the parameters used in the simulation, from the model used to simulate the hadronization, and from deficiencies in the description of the detector performance.

The sources of uncertainty on the selection efficiencies given in Table 6.8 are discussed in this section. The resulting systematic uncertainties on $g_{c\bar{c}}$ are summarized in Table 7.4.

7.1.1 Monte Carlo statistics

The statistical uncertainties on the Monte Carlo efficiencies (Table 6.8) through Eq. 6.3 translate to $\Delta g^{e}_{c\bar{c}} = \pm 0.13 \times 10^{-2}$ and $\Delta g^{\mu}_{c\bar{c}} = \pm 0.21 \times 10^{-2}$.

7.1.2 Gluon splitting to $b\bar{b}$ pairs

Propagating the effect of the uncertainty in the $g_{b\bar{b}}$ value in Eq. 6.3 yields $\Delta g^{e}_{c\bar{c}} = \pm 0.09 \times 10^{-2}$ and $\Delta g^{\mu}_{c\bar{c}} = \pm 0.10 \times 10^{-2}$.

7.1.3 Thrust cut

One of the main preselection requests is the thrust cut (see Sec. 6.4). The efficiency of the thrust cut is found to be different in the simulation compared to the data, as shown in Table 7.1. The effect is taken into account by reweighting, on a year by year basis, the Monte Carlo efficiencies to the data efficiencies. If no reweighting is performed, a shift is observed in the result: $\Delta g^{e}_{c\bar{c}} = +0.07 \times 10^{-2}$ and $\Delta g^{\mu}_{c\bar{c}} = +0.11 \times 10^{-2}$. This shift is taken as an error estimate, with full correlation between the two channels.

year	data (%)	MC (%)
1991	39.73 ± 0.10	39.96 ± 0.08
1992	39.60 ± 0.07	40.11 ± 0.04
1993	39.98 ± 0.06	40.09 ± 0.04
1994	40.00 ± 0.04	40.28 ± 0.03
1995	40.47 ± 0.06	40.32 ± 0.04

Table 7.1: Efficiency for the thrust cut.

7.1.4 Heavy quark properties

The lifetimes of the b hadrons determine the impact parameter distribution of the decay products, which is the basis of the "anti-b tag" method used in this analysis (see Sec. 4.6). Their values, with the current uncertainties, are taken from [2, 85] and shown in Table 7.2. The uncertainties translate to $\Delta g^{e}_{c\bar{c}} = \pm 0.03 \times 10^{-2}$ and $\Delta g^{\mu}_{c\bar{c}} = \pm 0.03 \times 10^{-2}$.

B hadron	Mean lifetime (ps)
B_d	1.540 ± 0.014
B_u	1.656 ± 0.014
B_s	1.461 ± 0.057
b-baryons	1.208 ± 0.051

Table 7.2: Lifetimes of the main b hadrons [2, 85].

The semileptonic branching ratios of c and b hadrons [86], BR($b \to l$),BR($b \to c \to l$) and BR($c \to l$), affect the flavour composition of the samples. Their uncertainties and their influence on the result of the analysis are shown in Table 7.3. The values used are taken from the fit to the LEP and SLD results [86, 13] excluding measurements of the heavy flavour asymmetries [87].

The energy spectra of leptons coming from $b \to l$, $c \to l$ and $b \to c \to l$ decays in the rest frame of the weakly decaying heavy hadron in simulated events have been tuned and varied as in [88] to reproduce the spectra given by the ACCMM model (described in Sec. 1.3.5) tuned to CLEO data [89] in the $b \to l$ case ($p_F = 0.298$ GeV/c from the fit)[1],

[1]The CLEO experiment studied only B^0 and $B^{\pm}$ mesons produced by the decay of the $\Upsilon(4S)$ resonance. Here the assumption is made that the result applies also to B_S mesons and Λ_b and other b baryons. This assumption is justified within the framework of the spectator model.

	$\Delta g^{e}_{c\bar{c}}(\times 10^{-2})$	$\Delta g^{\mu}_{c\bar{c}}(\times 10^{-2})$
$\mathrm{BR}(b \to l) = (10.65 \pm 0.23)\%$	± 0.05	± 0.06
$\mathrm{BR}(b \to c \to l) = (8.04 \pm 0.19)\%$	± 0.02	± 0.03
$\mathrm{BR}(c \to l) = (9.73 \pm 0.32)\%$	± 0.23	± 0.20
$b \to l$ modelling	-0.01	< 0.01
$b \to c \to l$ modelling	$+0.02$	$+0.02$
$c \to l$ modelling	$+0.03$	$+0.12$

Table 7.3: Effect of the uncertainties on the rates and energy spectra of heavy hadron semileptonic decays.

to MARK III [90] and DELCO [91] data in the $c \to l$ case ($p_F = 0.467$ GeV/c from the fit), and to a convolution of the $b \to D$ spectrum[2] measured by CLEO [92] with the $c \to l$ spectrum in the $b \to c \to l$ case. The effect has been propagated to the measured gluon splitting rate as shown in Table 7.3. The large difference between the electron and muon values for the $c \to l$ systematic error will be discussed in Sec. 7.1.9.

The scaled energy x_E ($\equiv p_{\mathrm{had}}/E_{\mathrm{beam}}$) distribution of the heavy hadrons affects the decay length distribution of the heavy hadrons and the momenta of the decay products. Heavy quark fragmentation is simulated using the Peterson model [64]. The parameters ε_b and ε_c (see Sec. 4.1.1), which control the shape of the functions, are adjusted to reproduce the measured value of the mean scaled energy of weakly-decaying heavy hadrons, $\langle x_E^{(b)} \rangle = 0.702 \pm 0.008$ and $\langle x_E^{(c)} \rangle = 0.484 \pm 0.008$ [52], and then varied within their estimated errors, obtaining $\Delta g^{e}_{c\bar{c}} = \pm 0.02 \times 10^{-2}$, $\Delta g^{\mu}_{c\bar{c}} = \pm 0.03 \times 10^{-2}$ when varying $\langle x_E^{(b)} \rangle$ and $\Delta g^{e}_{c\bar{c}} = \pm 0.04 \times 10^{-2}$, $\Delta g^{\mu}_{c\bar{c}} = \pm 0.05 \times 10^{-2}$ when varying $\langle x_E^{(c)} \rangle$, respectively.

7.1.5 Lepton identification

The systematic error associated to the lepton identification efficiency is estimated as in [72]. The ECAL selection efficiency for simulated events containing an electron is corrected to the data observed in six bins in $|\cos\theta|$ (corresponding to the ECAL barrel, the endcaps, the overlaps between barrel and endcaps) and two bins in p_T ($p_T < 0.25$ GeV/c and $p_T > 0.25$ GeV/c), while the efficiency of the dE/dx selection in the TPC is corrected in five angular bins. The muon identification efficiency is corrected to the data in three momentum bins ($2.5 < p < 3$ GeV/c, $3 < p < 4$ GeV/c, $p > 4$ GeV/c), in addition, for the latter, an angular binning is performed in 40 $|\cos\theta|$ regions.

[2] Here by $b \to D$ is meant any D^0 and $D^{\pm}$ produced by a B meson decay independently from the decay chain.

The resulting effect is $\Delta g^e_{c\bar{c}} = \pm 0.18 \times 10^{-2}$ and $\Delta g^\mu_{c\bar{c}} = \pm 0.01 \times 10^{-2}$.

7.1.6 Fake and non-prompt leptons

The same procedure as in Ref. [72] has been used to correct the rate of fake and non-prompt leptons predicted by the simulation and to estimate the corresponding uncertainty.

The measurement of the misidentification rate in the muon sample has been extensively discussed in Sec. 4.7.4. A correction factor of 17% is applied to the rate of fake and non-prompt muons that fulfil the selection cuts in the simulation. Such a factor is varied by 5% in order to assess the corresponding systematic uncertainty, obtaining $\Delta g^\mu_{c\bar{c}} = \pm 0.50 \times 10^{-2}$.

For fake and non-prompt electrons, an uncertainty of 20% is assigned to the rate of misidentified hadrons, and an uncertainty of 5% to the rate of photon conversions, giving $\Delta g^e_{c\bar{c}} = \pm 0.09 \times 10^{-2}$.

7.1.7 Generators

The modelling of the $g \to c\bar{c}$ process affects the selection efficiencies and hence the value of $g_{c\bar{c}}$. Three variables have been identified as being most relevant for the process: the energy E_g of the gluon, its effective mass m^*_g and the angle θ^* between the gluon direction and the c quark direction, measured in the gluon rest frame (see Fig. 7.1). The distributions of these variables as given by the JETSET generator are reweighted to match the prediction of the HERWIG generator [21, 22], and the difference observed in the measured value of $g_{c\bar{c}}$ is taken as an estimate of the systematic uncertainty. The procedure yields $\Delta g^e_{c\bar{c}} = +0.05 \times 10^{-2}$ and $\Delta g^\mu_{c\bar{c}} = +0.26 \times 10^{-2}$ for the effect of E_g and m^*_g (which are strongly correlated), $\Delta g^e_{c\bar{c}} = -0.06 \times 10^{-2}$ and $\Delta g^\mu_{c\bar{c}} = -0.12 \times 10^{-2}$ for the angular distribution.

The large difference between the electron and muon values for these systematic errors will be discussed in Sec. 7.1.9.

7.1.8 Mass of the charm quark

The mass of the charm quark is taken to be 1.2 ± 0.2 GeV/c^2 [2]. A shift in the charm mass results in a variation of the E_g and m^*_g distributions, as shown in Fig. 7.2. The corresponding uncertainties on the measured values are $\Delta g^e_{c\bar{c}} = \pm 0.19 \times 10^{-2}$ and $\Delta g^\mu_{c\bar{c}} = \pm 0.24 \times 10^{-2}$.

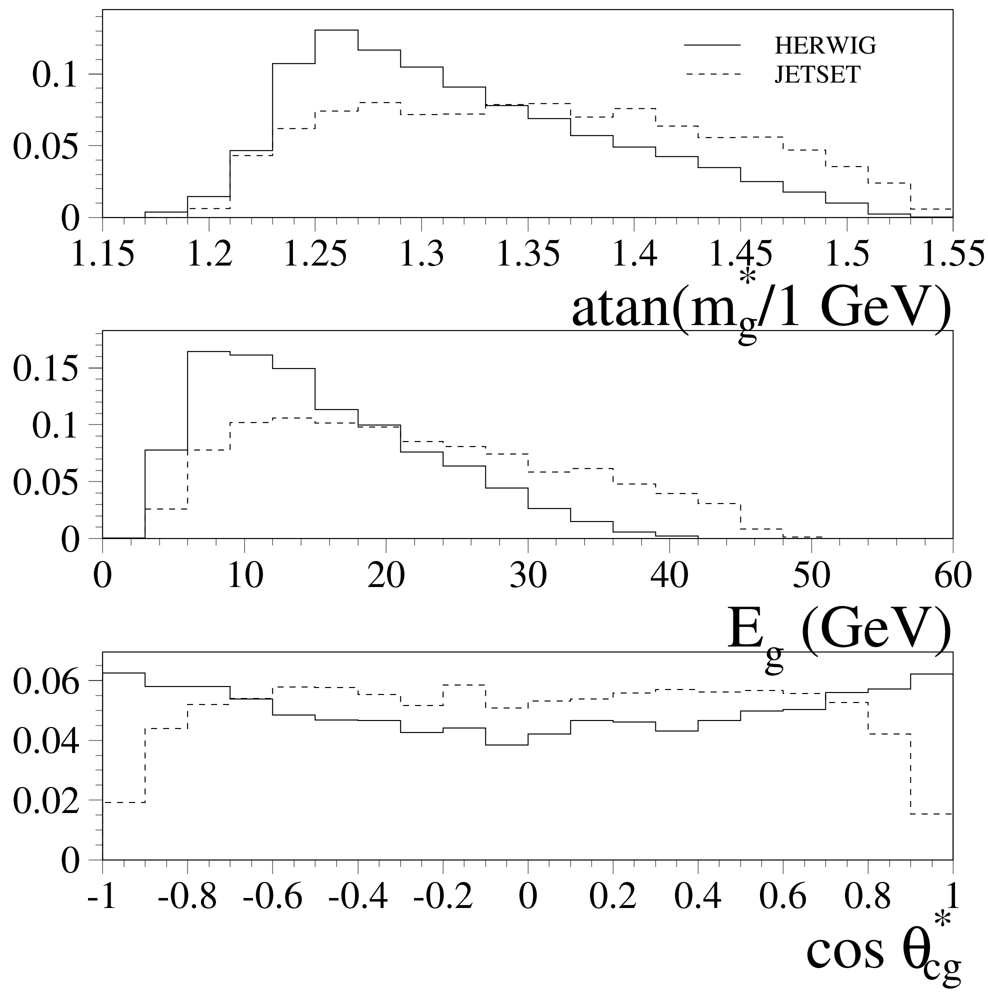

Figure 7.1: atan($m_g^*/1$ GeV$/c^2$), E_g, cos θ_{cg}^*, before any selection, for HERWIG and JETSET (normalized to the same arbitrary area).

7.1.9 Dependence of the systematic errors on the momentum cut

Some of the systematic errors have very different values for the electronic and muonic channels, even if important correlations exist between the two channels. This is due to the fact that these systematic errors are related to the lepton momentum, so that the different lower momentum cuts in electron and muon identification yield a different influence of the same systematic uncertainty source on the result.

Table 7.5 shows how these uncertainties vary with the momentum cut. Electrons are

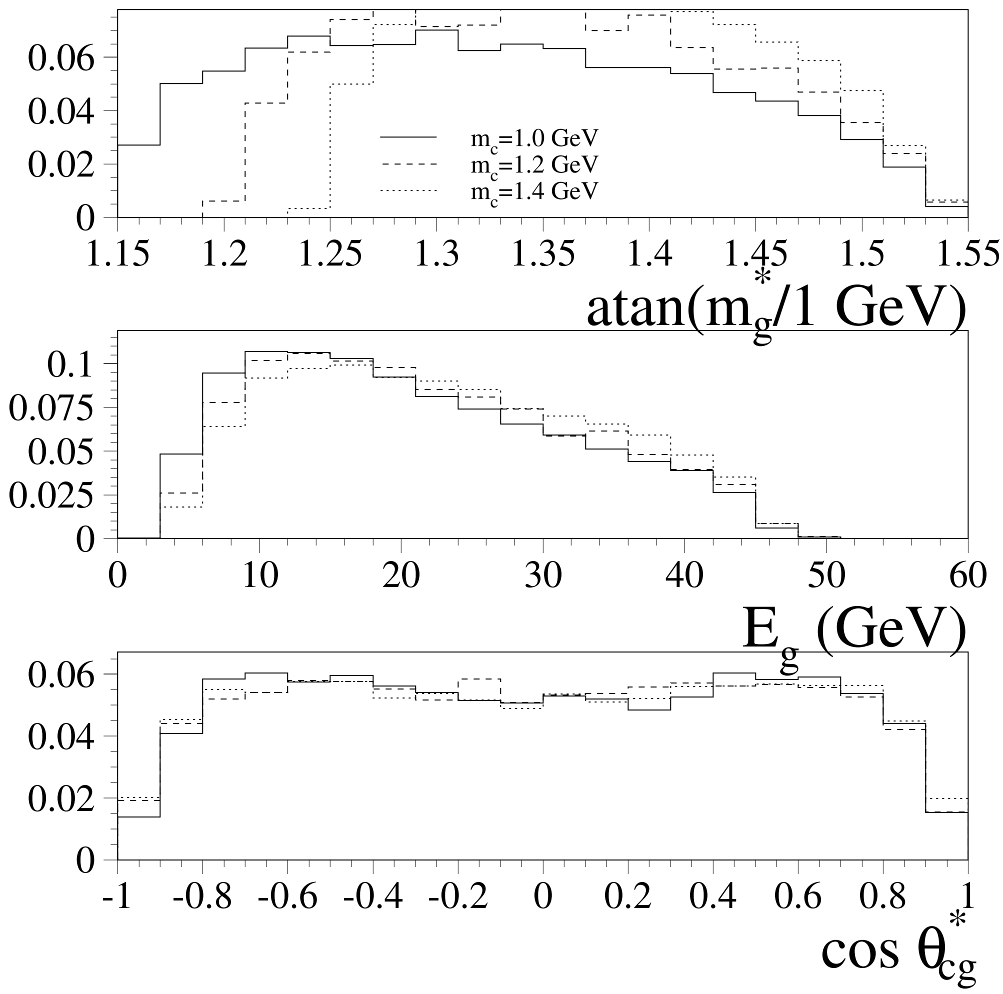

Figure 7.2: $\mathrm{atan}(m_g^*/1\ \mathrm{GeV}/c^2)$, E_g, $\cos\theta_{cg}^*$, before any selection, for three different values of the charm quark mass m_c (normalized to the same arbitrary area).

selected with momenta above 2 GeV/c, and their selection efficiency has a non-negligible dependence upon momentum and transverse momentum (calculated with respect to the jet axis), as shown in [71]. Muons are selected with momenta above 2.5 GeV/c. The efficiency is basically independent of momentum (above the cut) and transverse momentum. The different dependence of selection efficiency upon lepton kinematics for the two subsamples implies that the sensitivities to lepton modelling are in principle different.

In the case of the change of generator, most of the difference is simply due to the acceptance cut, as easily demonstrated by increasing the electron momentum cut to 2.5 GeV/c,

Source of error	$\Delta g^{e}_{c\bar{c}}$ ($\times 10^{-2}$)	$\Delta g^{\mu}_{c\bar{c}}$ ($\times 10^{-2}$)
Statistical error	0.28	0.38
ϵ_Q, ϵ_C, ϵ_B	0.13	0.21
$g_{b\bar{b}}$	0.09	0.10
Thrust cut efficiency	0.07	0.11
BR($b \to l$)	0.05	0.06
BR($b \to c \to l$)	0.02	0.03
BR($c \to l$)	0.23	0.20
$b \to l$ spectrum	0.01	< 0.01
$b \to c \to l$ spectrum	0.02	0.02
$c \to l$ spectrum	0.03	0.12
Lifetimes of b hadrons	0.03	0.03
$\langle x_E^{(c)} \rangle$	0.04	0.05
$\langle x_E^{(b)} \rangle$	0.02	0.03
Lepton identification	0.18	0.01
Lepton background	0.09	0.50
Generators, θ^*	0.06	0.12
Generators, $E_{\mathrm{g}}, m^*_{\mathrm{g}}$	0.05	0.26
m_{c}	0.19	0.24
Total systematic error	0.42	0.72

Table 7.4: Summary of the statistical and systematic uncertainties.

$p > 2.0$ GeV/c	$\Delta g^{e}_{c\bar{c}}$ ($\times 10^{-2}$)	$\Delta g^{\mu}_{c\bar{c}}$ ($\times 10^{-2}$)
$c \to l$ spectrum	0.03	-
Generators, θ^*	0.06	-
Generators, $E_{\mathrm{g}}, m^*_{\mathrm{g}}$	0.05	-
$p > 2.5$ GeV/c	$\Delta g^{e}_{c\bar{c}}$ ($\times 10^{-2}$)	$\Delta g^{\mu}_{c\bar{c}}$ ($\times 10^{-2}$)
$c \to l$ spectrum	0.06	0.12
Generators, θ^*	0.10	0.12
Generators, $E_{\mathrm{g}}, m^*_{\mathrm{g}}$	0.26	0.26
$p > 3.0$ GeV/c	$\Delta g^{e}_{c\bar{c}}$ ($\times 10^{-2}$)	$\Delta g^{\mu}_{c\bar{c}}$ ($\times 10^{-2}$)
$c \to l$ spectrum	0.09	0.15
Generators, θ^*	0.14	0.19
Generators, $E_{\mathrm{g}}, m^*_{\mathrm{g}}$	0.42	0.44

Table 7.5: Some systematic uncertainties for different momentum cuts.

and then both cuts to 3 GeV/c.

For equal momentum cut, the remaining small difference can be attributed to the dependence of the efficiency on momentum and transverse momentum, in the case of electrons. The shapes of the E_g and m^*_g distributions for the two generators are shown in Fig. 7.1. The gluon energy is strongly correlated with the lepton energy, while the gluon mass to first order determines the jet broadness.

7.2 Consistency checks

7.2.1 Stability of the neural network cuts

The stability of the results has been checked against the cuts on N_e and N_μ. Fig. 7.3 shows, for the electron and muon subsamples, the variation of the results for different cut values, together with the statistically uncorrelated error. No significant dependence is observed.

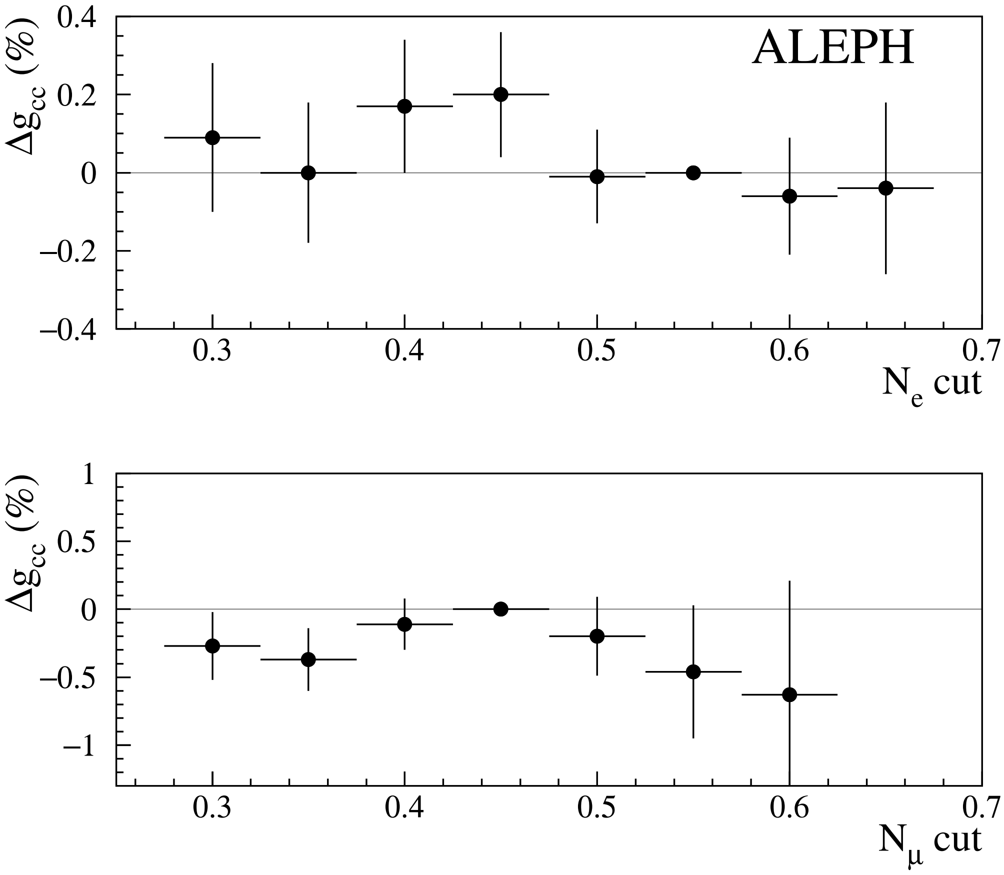

Figure 7.3: The variation $\Delta g_{c\bar{c}}$ versus the cut on the neural network outputs N_e, N_μ. The errors bars indicate the uncorrelated uncertainties only.

7.2.2 Analysis of simulated events

In the simulation the fraction of hadronic events with a gluon splitting to a $c\bar{c}$ pair is 1.79×10^{-2}. The analysis applied to simulated events yields $g^{e}_{c\bar{c}} = (1.70 \pm 0.21) \times 10^{-2}$ and $g^{\mu}_{c\bar{c}} = (1.75 \pm 0.29) \times 10^{-2}$, consistent with the input value.

7.2.3 Shape of the neural network outputs N_e and N_μ

The shapes of the neural network outputs for the electron and muon subsamples are shown in Fig. 7.4, for data and simulation. For the simulation, the $g_{c\bar{c}}$ value is fixed to the result of this analysis (average of the electron and muon subsamples, as given in Sec. 8.1). Rather good agreement is observed between data and simulation.

A somewhat different check is shown in Fig. 7.5, where the normalization of the Monte Carlo distribution is such to reproduce the data in the region $N_{e,\mu} < 0.2$. This is motivated by the fact that the signal is less well known than the background (which by far dominates over signal for low values of N_e and N_μ). Equalizing simulated and real data in the regime of low neural network output implies that any deviation for high N_e and N_μ values is probably to be imputed to the simulation of the signal. Also in this case, no significant discrepancy is observed between data and simulation.

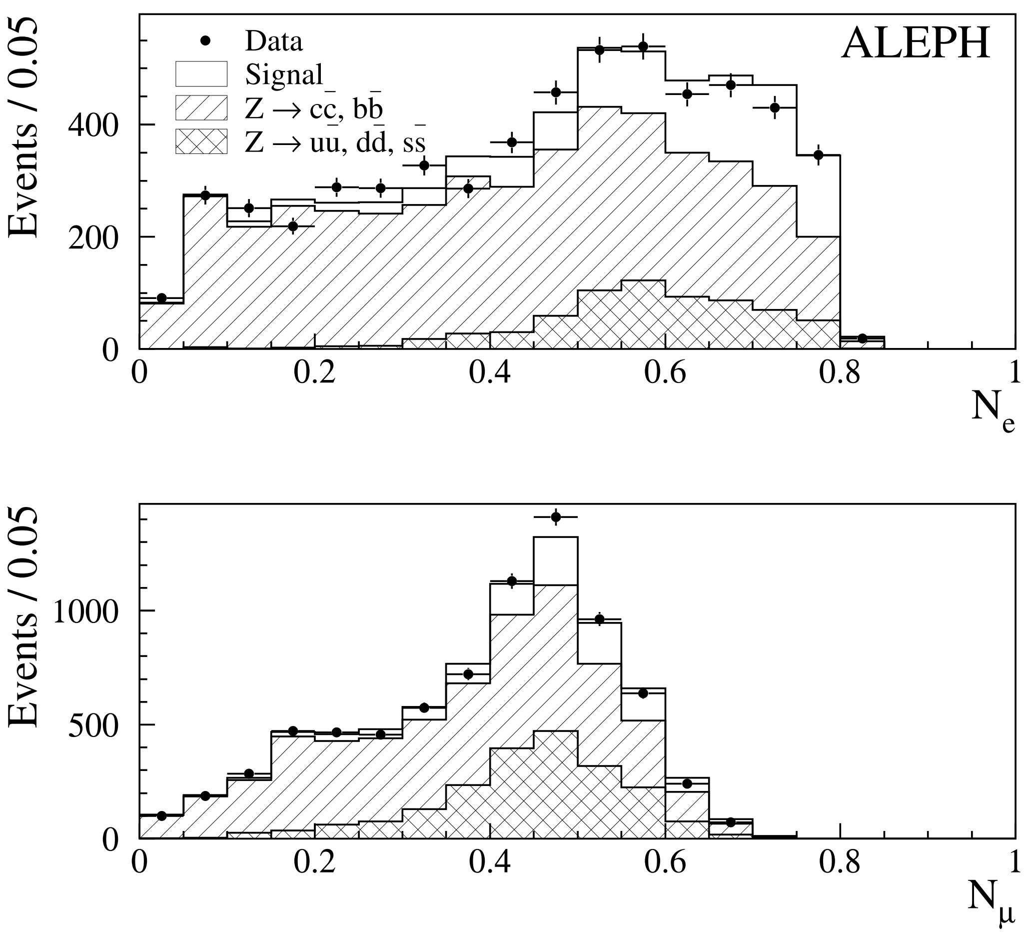

Figure 7.4: Output of the neural network for electrons and muons. In these plots, the simulation is normalized to the data and the signal is weighted according to the results of this analysis, as given in Sec. 8.1.

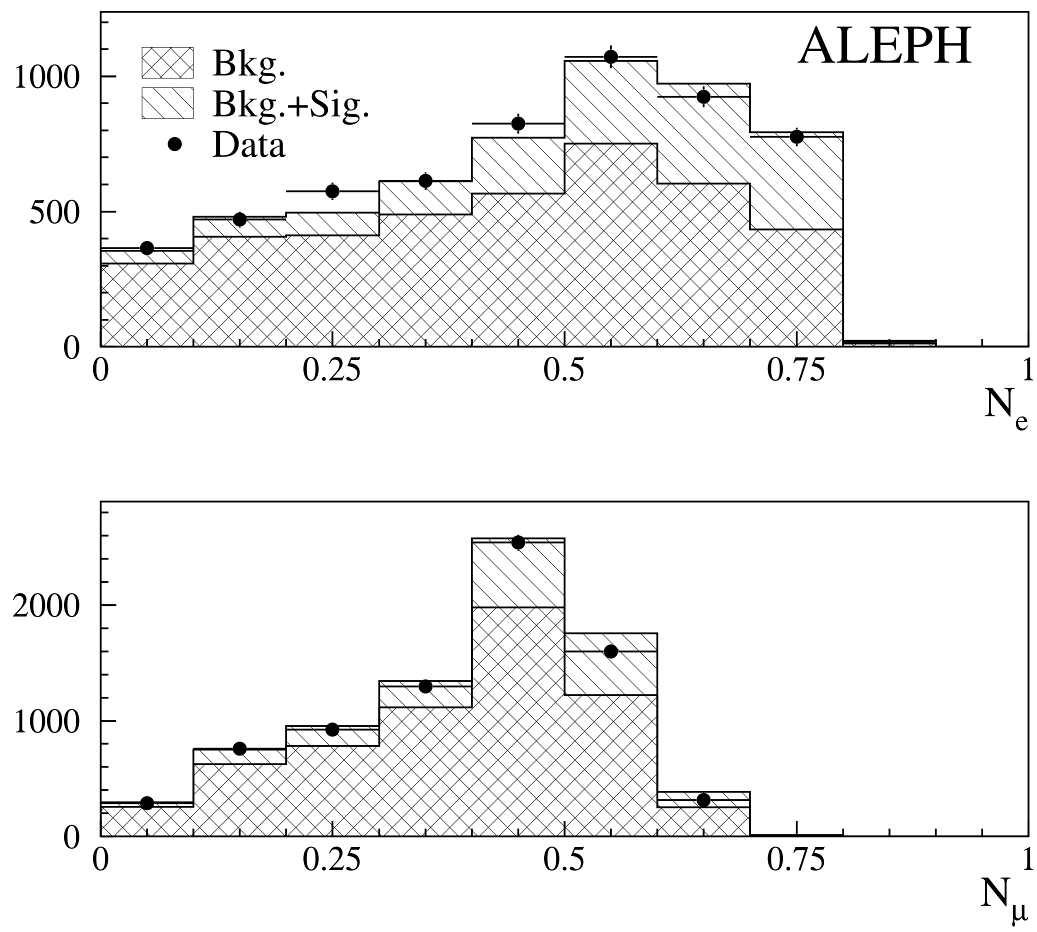

Figure 7.5: Output of the neural network for electrons and muons. In these plots, simulated events are normalized to data for $N_{e,\mu} < 0.2$, and the signal is normalized according to the results obtained in Sec. 6.8.

Chapter 8

Results and conclusions

The rate of gluon splitting into a $c\bar{c}$ pair in hadronic Z^0 decays at LEP with the ALEPH detector has been measured from samples containing an electron or a muon candidate:

$$g^e_{c\bar{c}} = (3.32 \pm 0.28(\text{stat}) \pm 0.42(\text{syst})) \times 10^{-2} , \tag{8.1}$$

$$g^\mu_{c\bar{c}} = (2.99 \pm 0.38(\text{stat}) \pm 0.72(\text{syst})) \times 10^{-2} . \tag{8.2}$$

8.1 Combination of the results of this analysis

The two results are combined taking in account the correlations between systematic uncertainties using the Best Linear Unbiased Estimator technique [93]. Having n measurements y_i of the physical observable y, this technique consists in the search for the best estimate $\hat{y}$ of the form

$$\hat{y} = \sum_i \alpha_i y_i , \tag{8.3}$$

where the weights α_i are constrained by the unitarity requirement

$$\sum_i \alpha_i = 1 . \tag{8.4}$$

The search is performed by minimizing the variance of $\hat{y}$, given by

$$\sigma^2 = \sum_i \sum_j E_{ij} \alpha_i \alpha_j . \tag{8.5}$$

The E_{ij} factors are the elements of the *error matrix*; the diagonal elements E_{ii} are the variances of the single measurements y_i, and the off-diagonal elements are the covariances. In the special case of two measurements we have:

$$E = \begin{pmatrix} \sigma_1^2 & r\sigma_1\sigma_2 \\ r\sigma_1\sigma_2 & \sigma_2^2 \end{pmatrix} \tag{8.6}$$

where r is the *correlation coefficient*. Every source of uncertainty has its own error matrix, and the global error matrix is the sum of the single error matrices.

The variance of $\hat{y}$, given by Eq. 8.5, has to be minimized with respect to the α_i's, with the additional constraint 8.4. This is obtained by expressing a particular α_i, e.g. α_1, as a function of the others by means of Eq. 8.4, treating the other α's as independent variables.

In the case considered, there is no correlation between the electron and muon channels regarding the statistical error on data and Monte Carlo, as well as the systematic errors coming from leptonic identification and misidentification procedures, while $r = 1$ is chosen for all the other uncertainties, giving the final ALEPH result

$$g_{c\bar{c}} = (3.26 \pm 0.23(\mathrm{stat}) \pm 0.42(\mathrm{syst})) \times 10^{-2}. \tag{8.7}$$

This result is in agreement with the other measurements available [48, 49, 50] and with the present world average $g_{c\bar{c}} = (2.96 \pm 0.38) \times 10^{-2}$ [52].

Figure 8.1 shows a comparison between result 8.7 and the published measurements.

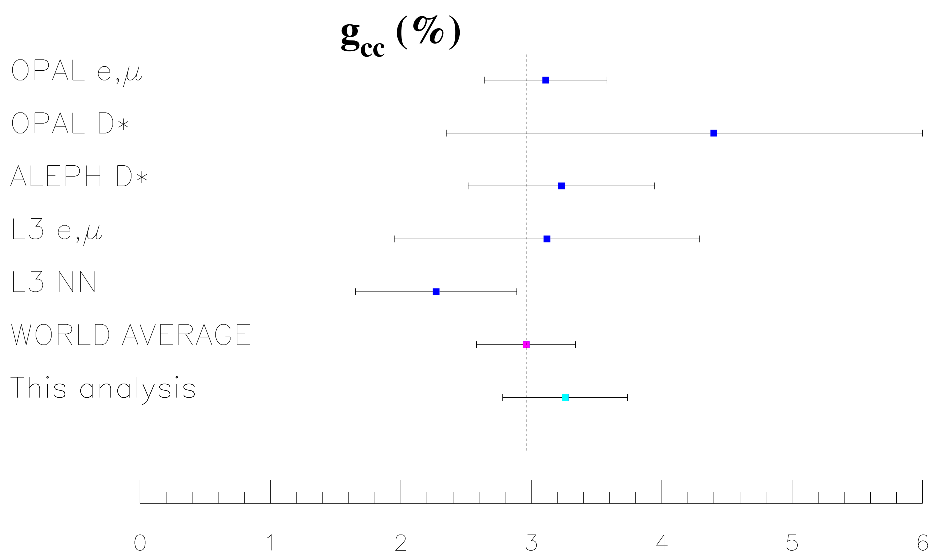

Figure 8.1: Comparison between the result given in this thesis and the previously published measurements, where the world average does not include this analysis.

8.2 New world average

To extract the new world average, the results of this thesis have to be combined with all the other measurements of $g_{c\bar{c}}$ (described in Sec. 2.3), taking properly into account all the correlations between systematic uncertainties.

An iterative method is used, consisting of the following steps: $g_{c\bar{c}}$ and $g_{b\bar{b}}$ are combined separately to obtain $g_{c\bar{c}}^{best}$ and $g_{b\bar{b}}^{best}$; then $g_{c\bar{c}}^{best}$ and $g_{b\bar{b}}^{best}$ are used to obtain a new estimate from each measurement. Given the strong correlation between $g_{c\bar{c}}$ and $g_{b\bar{b}}$ it is convenient to write every single result as

$$g_{c\bar{c}}^{i} = A_i - B_i \times g_{b\bar{b}}^{best} \,.$$

In the present case, results 8.1 and 8.2 can be rewritten as

$$\begin{aligned} g_{c\bar{c}}^{e} &= 3.76 \times 10^{-2} - 1.71 \times g_{b\bar{b}}^{best} \,, \\ g_{c\bar{c}}^{\mu} &= 3.46 \times 10^{-2} - 1.83 \times g_{b\bar{b}}^{best} \,. \end{aligned}$$

After a few iterations (three are sufficient for convergence), this procedure yields

$$g_{c\bar{c}} = (3.01 \pm 0.33) \times 10^{-2} \,, \tag{8.8}$$

$$g_{b\bar{b}} = (2.54 \pm 0.51) \times 10^{-3} \,. \tag{8.9}$$

Results 8.8 and 8.9 have to be compared to 2.22 and 2.23. The addition of the new results 8.1 and 8.2 gives only a slight shift in the mean values for $g_{c\bar{c}}$ and no appreciable variation for $g_{b\bar{b}}$, but a sizeable reduction in the total error for $g_{c\bar{c}}$.

OPAL e	22.6%
OPAL μ	3.0%
OPAL D^*	1.0%
L3 e	2.3%
L3 μ	0.4%
L3 ev.sh.	22.2%
ALEPH D^*	14.4%
ALEPH e	29.5%
ALEPH μ	4.6%

Table 8.1: Weights of the single $g_{c\bar{c}}$ measurements.

Table 8.1 shows the weight assigned by the BLUE method to every $g_{c\bar{c}}$ measurement in the combination. The result from the electronic channel of this thesis is the most important measurement; it should also be noted that the result from muon channel is the most important among the muon based analyses.

	ALEPH e	ALEPH μ
OPAL e	28%	23%
OPAL μ	18%	15%
OPAL D^*	5%	7%
L3 e	11%	6%
L3 μ	12%	7%
L3 ev.sh.	2%	1%
ALEPH D^*	4%	7%
ALEPH e	100%	34%
ALEPH μ	34%	100%

Table 8.2: Correlations between the e and μ channel results of this thesis and the other $g_{c\bar{c}}$ measurements.

The new world average (Eq. 8.8) has a two standard deviations distance from the theoretical prediction $g_{c\bar{c}} = 2.3 \times 10^{-2}$ (for $m_c = 1.2$ GeV and $\alpha_s = 0.120$), as discussed in Sec. 2.2.

It is worth noting that the theoretical gluon splitting rate strongly depends on the charm quark mass and on α_s, and has a sizeable uncertainty due to the neglected terms in the perturbation series. The theoretical uncertainty quoted in Ref. [34] due to the truncation of the perturbation series (30% of the result, i.e. $\Delta g^{th}_{c\bar{c}} = \pm 0.7 \times 10^{-2}$) is enough to account for the discrepancy, but it is certainly overestimated (a much less conservative guess for this uncertainty is 15%, according to the same paper). Furthermore, a positive shift of 0.002 in the strong coupling constant (equal to the current total uncertainty, see Eq. 1.44) yields an increase of 0.3×10^{-2} in $g_{c\bar{c}}$ (almost one standard deviation of the world average). The charm quark mass affects the experimental determination, as discussed in Sec. 7.1.8, and also the theoretical result. A negative shift of 0.2 GeV/c^2 ($m_c = 1.0$ GeV/c^2) would yield a positive shift of 0.4×10^{-2} on the $g_{c\bar{c}}$ prediction, partially compensated by a shift of 0.2×10^{-2} on the experimental result, for an overall reduction of the discrepancy between theory and data by 2/3 of a standard deviation.

8.3 Impact of this result on other analyses

8.3.1 Decay fractions of the Z^0 in c and b

These two observables have been discussed in Sec. 1.4.2. Results 1.32 and 1.33 are derived using the old average values for $g_{c\bar{c}}$ and $g_{b\bar{b}}$. The influence of $g_{c\bar{c}}$ and $g_{b\bar{b}}$ on R_c and R_b has been shown in Tab. 2.1. Since

$$\frac{R_Q^{new} - R_Q^{old}}{\Delta R_Q} = a \frac{g_{Q\bar{Q}}^{new} - g_{Q\bar{Q}}^{old}}{\Delta g_{Q\bar{Q}}} \ , \tag{8.10}$$

with $a = +1$ in case of positive correlation and -1 in the opposite case, it is straightforward to extract the updated values of R_b and R_c:

$$R_b = 0.21643 \pm 0.00065 \ , \tag{8.11}$$

$$R_c = 0.1717 \pm 0.0031 \ . \tag{8.12}$$

As can be seen, the induced changes are almost negligible. Table 8.3 shows the new contributions of gluon splitting to the total error on R_c and R_b.

	Error on R_b	**Error on R_c**
$g_{b\bar{b}} = (2.54 \pm 0.51) \times 10^{-3}$	0.000202 (anticorr.)	0.000106 (corr.)
$g_{c\bar{c}} = (3.01 \pm 0.33) \times 10^{-2}$	0.000064 (anticorr.)	0.000672 (anticorr.)
total	0.000653	0.003044

Table 8.3: Contribution of the gluon splitting uncertainties to the total error of R_b and R_c. "Corr." or "anticorr." indicates if the R_Q measurement is positively or negatively correlated with $g_{Q\bar{Q}}$.

Bibliography

[1] The ALEPH collaboration, *A measurement of the gluon splitting rate into $c\bar{c}$ pairs in hadronic Z decays*, Phys.Lett. **B561** (2003) 213.

[2] Particle Data Group, K. Hagiwara et al., *Review of Particle Physics*, Phys.Rev. **D66** (2002) 010001.

[3] S.L. Glashow, *Partial symmetries of weak interactions*, Nucl.Phys. **22** (1961) 597.

[4] S. Weinberg, *A model of leptons*, Phys.Rev.Lett. **19** (1967) 1264.

[5] A. Salam, *Elementary Particle Theory*, ed. N. Svartholm (Almquist and Wiksells, Stockholm, 1969).

[6] G. Altarelli, G. Parisi, *Asymptotic freedom in parton language*, Nucl.Phys. **B126** (1977) 298.

[7] C.S. Kim, A.D. Martin, *On the determination of V_{ub} and V_{cb} from semileptonic B decays*, Phys.Lett. **B225** (1989) 186.

[8] G. Altarelli, N. Cabibbo, G. Corbò, L. Maiani, G. Martinelli, *Leptonic decay of heavy flavors: A theoretical update*, Nucl.Phys. **B208** (1982) 365.

[9] G. Altarelli, S. Petrarca, *Inclusive beauty decays and the spectator model*, Phys. Lett. **B261** (1991) 303.

[10] R. V. Wagoner, W. A. Fowler, F. Hoyle, *On the synthesis of elements at very high temperatures*, Ap.J. **148** (1967) 3.

[11] The CDF collaboration, *Measurement of the Top Quark Mass with the Collider Detector at Fermilab*, Phys.Rev.Lett. **82**, (1999) 271.

[12] The D0 collaboration, *Direct measurement of the top quark mass by the D0 Collaboration*, Phys.Rev. **D58**, (1998) 052001.

[13] The LEP Electroweak Working Group, *A combination of preliminary electroweak measurements and constraints on the Standard Model* (2002) CERN-EP/2002-091.

[14] S. Bethke, *Determination of the QCD coupling α_s*, J.Phys. **G26** (2000) R27.

[15] The ALEPH collaboration, *Measurement of the strong coupling constant using τ decays*, Phys.Lett. **B307** (1993) 209.

[16] The OPAL collaboration, *Measurement of the strong coupling constant α_s and the vector and axial-vector spectral functions in hadronic τ decays*, Eur.Phys.J. **C7** (1999) 571.

[17] H. Georgi, M. Machacek, *Simple Quantum-Chromodynamics prediction of jet structure in e^+e^- annihilation*, Phys.Rev.Lett. **39**, (1977) 1237.

[18] E. Fahri, *Quantum Chromodynamics test for jets*, Phys.Rev.Lett. **39**, (1977) 1587.

[19] T. Chandramohan, L. Clavelli, *Consequences of 2nd order QCD for jet structure in e^+e^- annihilation*, Nucl.Phys. **B184** (1981) 365.

[20] T. Sjöstrand, *PYTHIA 5.7 and JETSET 7.4 physics and manual*, 1993, CERN-TH.7112/93.

[21] G. Marchesini et al., *HERWIG – A Monte Carlo event generator for simulating Hadron Emission Reactions With Interfering Gluons*, Computer Phys.Comm. **67** (1992) 465.

[22] G. Corcella et al., *HERWIG 6.3 release note*, JHEP **0101** (2001) 010.

[23] G. Dissertori, *Measurements of α_s from event shapes and the four-jet rate*, Proceedings of the 31st International Conference on High Energy Physics, Amsterdam, 24-31 July 2002; hep-ex/0209070.

[24] A.V. Manohar, M.B. Wise, *Power suppressed corrections to hadronic event shapes*, Phys.Lett. **B344** (1995) 407.

[25] Y.L. Dokshitzer, G. Marchesini, B.R. Webber, *Dispersive approach to power-behaved contributions in QCD hard processes*, Nucl.Phys. **B469** (1996) 93.

[26] Y.L. Dokshitzer, A. Lucenti, G. Marchesini, G.P. Salam, *Universality of 1/Q corrections to jet-shape observables rescued*, Nucl.Phys. **B511** (1998) 396.

[27] G.P. Korchemsky, G. Sterman, *Nonperturbative corrections in resummed cross sections*, Nucl.Phys. **B437** (1995) 415.

[28] P.A. Movilla Fernandez, O. Biebel, S. Bethke, *Tests of Power Corrections to Event Shape Distributions from* e^+e^- *Annihilation*, hep-ex/9906033.

[29] G. Dissertori, *Experimental status of measurements of* α_s *at LEP*, Proceedings of the XIIIth meeting on physics at LEP (Roma, 2001).

[30] The ALEPH collaboration, *A measurement of* R_b *using a lifetime-mass tag*, Phys.Lett. **B401** (1997) 163.

[31] The LEP Working Group for Higgs Boson Searches, *Search for the Standard Model Higgs Boson at LEP*, Proceedings of the 31st International Conference on High Energy Physics, Amsterdam, 24-31 July 2002.

[32] The ALEPH collaboration, *Final results of the searches for neutral Higgs bosons in* e^+e^- *collisions at* $\sqrt{s}$ *up to 209 GeV*, Phys.Lett. **B526** (2002) 191.

[33] M. H. Seymour, *Heavy quark production in jets*, Z.Phys. **C63** (1994) 99.

[34] M.H. Seymour, *Heavy quark pair multiplicity in* e^+e^- *events*, Nucl.Phys. **B436**, (1995) 163.

[35] S. Frixione et al., *Heavy quark production*, Adv.Ser.Direct.High Energy Physics **15** (1998) 609.

[36] A.K. Likhoded, A.I. Onishchenko, *Gluon splitting into a pair of heavy quarks in* e^+e^- *annihilation*, Phys.Atom.Nucl. **60** (1997) 623.

[37] D.J. Miller, *The multiplicity of heavy quark pairs from gluon splitting in* e^+e^- *annihilation*, 1998, RAL-TR-98-043, hep-ph/9806302, Proceedings of the XXXIst Rencontres de Moriond (Moriond, Les Arcs, 1998).

[38] D.J. Miller, M.H. Seymour, *Secondary heavy quark pair production in e^+e^- annihilation*, Phys.Lett. **B435** (1998) 213.

[39] Y.L. Dokshitzer, V.A. Khoze, A.H. Mueller, S.I. Troyan, *Basics of perturbative QCD*, (1991) Editions Frontières, Gif-sur-Yvette.

[40] A.H. Hoang, M. Ježabek, J.H. Kühn, T. Teuber, *Hadron radiation in leptonic Z decays*, Phys.Lett. **B325** (1994) 495 [Erratum: Phys.Lett. **B327** (1994) 439].

[41] W.H. Furry, *A simmetry theorem in the positron theory*, Phys.Rev. **51** (1937) 125.

[42] B.A. Kniehl, J.H. Kühn, *QCD corrections to the Z decay rate*, Nucl.Phys. **B329** (1990) 547.

[43] R. Bonciani, S. Catani, M. Mangano, P. Nason, *NLL resummation of the heavy quark hadroproduction cross-section*, Nucl. Phys. **B529**, 424 (1998).

[44] Y.L. Dokshitzer, *Improved QCD treatment of the KNO phenomenon*, Phys.Lett. **B305** (1993) 295.

[45] S. Catani, Y.L. Dokshitzer, F. Fiorani, B.R. Webber, *Average number of jets in e^+e^- annihilation*, Nucl.Phys. **B377** (1992) 445.

[46] A.H. Mueller, P. Nason, *Heavy particle content in QCD jets*, Nucl.Phys. **B266** (1986) 265.

[47] M.A. Shifman, A.I. Vainshtein, V.I. Zakharov, *QCD and resonance physics*, Nucl.Phys. **B147** (1979) 385, 448 and 519.

[48] The OPAL collaboration, *Measurement of the production of charm quark pairs from gluons in hadronic Z decays*, Eur.Phys.J. **C13** (2000) 1.

[49] The ALEPH collaboration, *Study of charm production in Z decays*, Eur.Phys.J. **C16** (2000) 597.

[50] The L3 collaboration, *Measurement of the probability of gluon splitting into charmed quarks in hadronic Z decays*, Phys.Lett. **B476** (2000) 243.

[51] G.C. Fox and S. Wolfram, *Test for planar events in e^+e^- annihilation*, Phys. Lett. **B82** (1979) 134.

[52] The LEP/SLD Heavy Flavour Working Group, *Final input parameters for the LEP/SLD heavy flavour analyses*, (2001) LEPHF/2001-01.

[53] LEP design report, CERN-LEP/84-01 (1984)

[54] The LEP polarization team, *Accurate determination of the LEP beam energy by resonant depolarization*, Z. Phys. **C66** (1995) 45.

[55] The ALEPH collaboration, *ALEPH: a detector for electron-positron annihilations at LEP*, Nucl.Instr.Meth. **A294** (1990) 121.

[56] The ALEPH collaboration, *Performance of the ALEPH detector at LEP*, Nucl.Instr.Meth. **A379** (1995) 101.

[57] G. Batignani et al., 1991 IEEE nuclear science symposium, Santa Fe, IEEE Trans. Nucl. Sci. NS-39 (4/5) (1992) vol.I, p.438.

[58] B. Mours et al., *The design, construction and performance of the ALEPH silicon vertex detector*, Nucl. Instrum. and Methods **A379** (1996) 101.

[59] W.B. Atwood et al., *Performance of the ALEPH Time Projection Chamber*, Nucl.Instr.Meth. **A306** (1991) 446.

[60] The ALEPH collaboration, *Properties of hadronic Z^0 decays and test of QCD generators*, 1992, Z.Phys. **C55**, 209.

[61] The ALEPH collaboration, *Studies of quantum chromodynamics with the ALEPH detector*, Phys.Rep. **294** (1998) 1.

[62] B. R. Webber, *Monte Carlo simulation of hard hadronic processes*, Ann.Rev.Nucl.Part.Sci. **36** (1986) 253.

[63] B. Andersson, G. Gustafson, G. Ingelman, T. Sjostrand, *Parton fragmentation and string dynamics*, Phys.Rep. **97** (1983) 31.

[64] C. Peterson et al., *Scaling violations in e^+e^- annihilation spectra*, Phys.Rev. **D27**, (1983) 105.

[65] The ALEPH collaboration, *Study of the fragmentation of b quarks into B mesons at the Z peak*, Phys.Lett. **B512** (2001) 30.

[66] R. Brun et al., *GEANT*, 1984, CERN DD/EE/84-1.

[67] R. Frühwirth, *Application of Kalman Filtering to track and vertex fitting*, Nucl.Instr.Meth. **A262** (1987) 444.

[68] The JADE collaboration, *Experimental studies on multi-jet production in e^+e^- annihilation at PETRA energies*, Z.Phys. **C33** (1986) 23.

[69] ALEPH collaboration, *Tagging b hadrons using track impact parameters*, 1992, ALEPH 95-135.

[70] A. M. Stacey, *A precise measurement of* $\Gamma_{Z^0\to b\bar{b}}/\Gamma_{Z^0\to hadrons}$, 1996, Ph.D. thesis, Imperial College.

[71] The ALEPH collaboration, *Heavy quark tagging with leptons in the ALEPH detector*, Nucl.Instr.Meth. **A346** (1994) 461.

[72] The ALEPH collaboration, *Inclusive semileptonic branching ratios of b hadrons produced in Z decays*, Eur.Phys.J. **C22** (2002) 613.

[73] The ALEPH collaboration, *The Forward-Backward Asymmetry for Charm Quarks at the Z*, Phys.Lett. **B 434** (1998) 415.

[74] The ALEPH collaboration, *Production of K^0 and Λ in hadronic Z decays*, Z.Phys. **C64** (1994) 361.

[75] S. Haykin, *Neural Networks, a comprehensive foundation* (2nd ed., 1999), Prentice Hall, Upper Saddle River (NJ).

[76] K. Gurney, *An Introduction to Neural Networks* (2002), UCL Press, London.

[77] W.S. Sarle, *Neural Network FAQ*, periodic posting to the Usenet newsgroup comp.ai.neural-nets, URL: ftp://ftp.sas.com/pub/neural/FAQ.html

[78] A. Zell et al., *Stuttgart Neural Network Simulator, User Manual, Version 4.1*, URL: http://www-ra.informatik.uni-tuebingen.de/SNNS/UserManual/UserManual.html

[79] D.E. Rumelhart, J.L. McClelland, eds. *Parallel Distributed Processing*, (1986), MIT Press, Massachusetts.

[80] B.T. Polyak, *Some methods of speeding up the convergence of iterative methods*, Zh.Vychisl.Mat.Mat.Fiz. **4** (1964) 1.

[81] M. Riedmiller and H. Braun, *A Direct Adaptive Method for Faster Backpropagation Learning: The RPROP Algorithm* (1993), Proc. ICNN, San Francisco.

[82] N. Draper, H. Smith, *Applied Regression Analysis*, (1991), John Wiley ed., New York.

[83] K. Hornik, M. Stinchcombe, H. White, *Multilayer feedforward networks are universal approximators*, Neur.Net., **2** (1989) 359.

[84] E.D. Sontag, *Feedback stabilization using two-hidden-layer nets*, IEEE Transactions on Neural Networks, **3** (1992) 981.

[85] A. Stocchi, *Experimental results on heavy quark hadrons*, Proceedings of the 31st International Conference on High Energy Physics, Amsterdam, 24-31 July 2002.

[86] A. Tricomi, *The B semileptonic branching fractions in* $Z^0 \to b\bar{b}$ *decays*, Proceedings of the 31st International Conference on High Energy Physics, Amsterdam, 24-31 July 2002.

[87] F. Palla, *Semileptonic B decays and CKM elements at LEP*, Proceedings of the EPS International Conference on High Energy Physics, Budapest, 2001, JHEP (http://jhep.sissa.it), Proceedings Section, PrHEP-hep2001/077.

[88] The ALEPH collaboration, *Measurement of the forward–backward asymmetry in* $Z \to b\bar{b}$ *and* $Z \to c\bar{c}$ *decays with leptons*, Eur.Phys.J. **C24** (2002) 177.

[89] The CLEO collaboration, *Measurement of semileptonic branching fractions of B mesons at the* $\Upsilon(4S)$ *resonance*, Phys. Rev. **D 45** (1992) 2212.

[90] The MARK III collaboration, *Direct measurement of charmed* D^+ *and* D^0 *semileptonic branching ratios*, Phys. Rev. Lett. **54** (1985) 1976.

[91] The DELCO collaboration, *Semileptonic decays of the D meson*, Phys. Rev. Lett. **43** (1979) 1073.

[92] The CLEO collaboration, *Inclusive and exclusive decays of B mesons to final states including charm and charmonium mesons*, Phys. Rev. **D 45** (1992) 21.

[93] L. Lyons, D. Gibaut, P. Clifford, *How to combine correlated estimates of a single physical quantity*, Nucl.Inst.Meth. **A270** (1988) 110.

Acknowledgments

I cannot be thankful enough to Professor Lorenzo Foà for his supervision throughout my Scuola di Perfezionamento in Scuola Normale Superiore.

I have had the pleasure to work very closely with Fabrizio Palla, who deserves a lot of credit for the successful completion of my work on gluon splitting and of this thesis.

It has also been a very formative experience to work with the rest of the people in ALEPH. I am especially grateful for the helpful inputs from Roberto Tenchini, Duccio Abbaneo and Günther Dissertori.

I must thank Marco Cirelli because he proved to be a good friend and because he was always there to sort out my endless questions about perturbative QCD.

Finally, I would like to thank Massimiliano Chiorboli, who went through the same pains and joys since our first year at University of Catania, Giovanni Signorelli who helped me to understand every aspect of life in Pisa and in Scuola Normale and whose enthusiasm for almost every field of physics is contagious, and all the other friends in Pisa and Catania (too many to be listed here). I learned more from our discussions at the "mensa" about Physics, Life, Universe and Everything than from any book or lesson.